IJCOE
COASTAL, OFFSHORE & ENVIRONMENTAL ENGINEERING




Volume 3 | Issue 3 | Oct 2018



www.ijcoe.org info@ijcoe.org 11



International Journal of Coastal, Offshore and Environmental Engineering (IJCOE) | Vol 3 | Issue 3 | Oct 2018



Since 2015

International Journal of Coastal, Offshore & Environmental Engineering

ISSN: 2980-8731 (online)



Volume 3 | Issue 3| Oct 2018

IJCOE

Editor-in-Chief: Prof. Hamid S.Bahai

International Journal of Coastal, Offshore & Environmental Engineering
Since 2015
ISSN: 2980-8721 (online)

**In The Name of God**

## Message from the Editor-in-Chief

The IJCOE journal office was established in 2015,and its first issue was published in 2016. TheIJCOE covers a wide range of research in thefields of oceanography & ocean technology, aswell as marine industries & marine engineering.The editorial board of IJCOE consists of nearly130 of the greatest scientists and researchersfrom over 30 countries worldwide, and thejournal's review board comprises 1,000 membersfrom all five continents. The membership andapplication process for joining the editorial andreview boards of this journal is ongoing. IJCOE isa research-academic quarterly journal that haspublication and distribution permissions fromthe Press Organization and permission topublish scientific-research articles from theMinistry of Science, Research, and Technology(MSRT) with an "A" rating. It also holds a "Q1"rating from the ISC institute with an impactfactor (IF) of approximately 0.43 and isconsidered a "core journal" (prestigious andoutstanding journal). IJCOE is an open-accessjournal and allows the download and receipt ofaccepted articles in full text for free. It respectsand adheres to copyright and COPE regulations.The journal's office operates 24/7, providingservices to researchers. In addition to publishinga regular quarterly journal, IJCOE has 16 specialissues on specific topics in preparation. It alsoprovides conditions for publishing specializedbooks, references, and handbooks. Moreover, itis ready to cooperate with the secretariats ofreputable international conferences to publishtheir selected and outstanding articles. IJCOEevaluates, appraises, and publishes books,articles, and the scientific achievements andfindings of esteemed researchers and scientistsworldwide who are innovating and conductingin-depth research in the "important and strategicfield of the maritime technology & Oceanengineering." It welcomes any form of jointcooperation with universities, research institutes,and related research centers at the national,regional, and international levels, and extends ahand for collaboration.

## Classification of Editorial Board in IJCOE

Editor-in-Chief

Director-in-Chief

Deputy Editor

Executive Managers

English Text Editor

Technical Editor

International Editorial Board

National Editorial Board

Editorial Board Associate

Editorial Board Assistant

Guest Editorial Board

Advisory Board

Administrative Coordinator

Honorary Board Member

Methodology Advisor

## Author Benefits

- Open Access
- Rapid Publication
- Thorough Peer-Review
- No Copyright Constraints
- Coverage by Leading Indexing Services
- Discounts On Article Processing Charges (APC)
- No Space Constraints, No restriction on the maximum length of the papers, number of figures or colors

INTERNATIONAL JOURNAL OF IJCOE COASTAL, OFFSHORE & ENVIRONMENTAL ENGINEERING

## Aims of IJCOE

Hydrodynamics

Marine equipment

Structural mechanics

Ocean environmental predictions

Stochastic calculations Experimental

Automatic Control of Marine Systems

## Scope of IJCOE

Marine Hazards

Ocean Acoustics

Naval Architecture

Ocean Engineering

Coastal Engineering

Marine Meteorology

Marine Earth Sciences

Underwater Technology

Marine Renewable Energy

Polar & Arctic Engineering

Marine Renewable Energy

Marine Geography & Geodesy

Marine Environmental Engineering

Automatic Control of Marine Systems

Hydro Physics & Physical Oceanography

## Type of papers

- Case Studies
- Book Reviews
- Review Article
- Letters to the Editor
- Methodology Papers
- Editorials and Commentaries
- Response or Rejoinder Papers
- Perspective or Opinion Papers
- Conceptual or Theoretical Papers
- Meta-Analysis and Systematic Reviews
- Short Communications or Brief Reports
- Research Articles (Original Research Papers)

## Scientific Research Journal

**Ministry of Science, Research And Technology (MSRT)**

Jurnal Ranking 2023: A

**Ministry Of Science, Research And Technology (ISC)**

Citation Impact 2022: 0.429

Quartile 2022 : Q1

Core Collection

IJCOE is a Member of


## Cantact Us

**Office 1 |** Research Institute of Meteorology and Atmospheric Science

**Address |** Tehran, Shahid Kharrazi Highway, Pajoohesh Blvd, Research Institute of Meteorology and Atmospheric Science, Sand and Dust Storm International Research Center (SDS-IRC), No. 13, 1st floor.

**Phone |** +982144787652

**Postal code |** 13611-14977

**website |** www.rimac.ac.ir

**Office 2 |** Iranian National Institute for Oceanography and Atmospheric Science

**Address |** Tehran, Dr. Fatemi Gharbi St., Shahid Etemadzade St., No. 3, third floor.

**Phone |** +982166944873

**Postal code |** 13389 – 14118

**website |** www.inio.ac.ir

**Email |** Info@ijcoe.org

**Website |** www.ijcoe.org

## Follow Us

www.ijcoe.org

INTERNATIONAL JOURNAL OF IJCOE COASTAL, OFFSHORE & ENVIRONMENTAL ENGINEERING

**Volume & Issue:**

**Volume 3, Issue 3, October2018**

**Number of Articles: 6**

# Content

INTERNATIONAL JOURNAL OF
COASTAL & OFFSHORE ENGINEERING
IJCOE Vol.3/No. 3/Autumn 2018 (1-12)

*Available online at: http://ijcoe.org/browse.php?a_code=A-10-164-1&sid=1&slc_lang=en*

# The Effects of Sea Level Fall on the Caspian Sea Shoreline Changes

**Soheil Ataei H.[1*], Mehdi Adjami [2] and Seyed Ahmad Neshaei[3]**

*[1*] Ph.D. Candidate, Faculty of Civil Engineering, Shahrood University of Technology, Shahrood, Iran; ataei.h.s@gmail.com*
*[2] Assistant Professor, Faculty of Civil Engineering, Shahrood University of Technology, Shahrood, Iran; adjami@shahroodut.ac.ir*
*[3] Associate Professor, Department of Civil Engineering, Faculty of Engineering, University of Guilan, Rasht, Iran; maln@guilan.ac.ir*

**ARTICLE INFO**

*Article History:*
Received: 24 May 2018
Accepted: 26 Nov. 2018

*Keywords:*
Shoreline Changes
Sea Level Change
Bruun Rule
Landward Sediment Transport
Caspian Sea

**ABSTRACT**

The Caspian Sea level has experienced frequent fluctuations resulting in shoreline advance and retreat. Therefore, studying and predicting shoreline changes in the Caspian Sea are very important. The "Bruun Rule" was presented in order to predict shoreline variation due to sea level rise. In addition, to improve the predictions of the Bruun rule, added landward sediment transport to it, leading to more desirable results. In this research, the Bruun rule and its modified form, extended for landward transport, were investigated for the Caspian Sea level fall conditions. The modified equation in this study leads to the better results, which indicates that due to sea level fall and natural storms, there would be sediment deposition toward the shoreline. In terms of water level reduction, by applying the coefficient, the root mean squared error was obtained 3.447 meters for predicting shoreline changes in comparison to its natural changes. According to the results, the lowest difference in prediction is related to the Mahmudabad coast and the highest difference in prediction is related to the Dastak coast, which are equal to 0.059 and 4.849 meters, respectively. Based on this trend for forecasting shoreline changes by applying the coefficient and not having much difference in calculating the root mean square error based on the proposed equation of Rosati et al., it is possible to use the optimized equation in this study as a prediction of shoreline changes in terms of sea level fall; This coefficient has improved the forecasting trend of coastline changes in terms of water level reduction for each of the studied areas with direct deviations of $D_{50}$ and $H_B$ in the equation, and the results obtained from forecasting shoreline variations show a lower difference for each area.

## 1. Introduction

Most of the shorelines are covered with sands. At some point, a river, a tidal inlet or a rocky promontory cuts them. By breaking waves and running-up on shore face, the coastal surface changes continuously. Continuous changes in the shape of shores occur because the characteristics of a wave (its height, period and angle upon approaching the beach) scarcely remain constant for a certain period of time.
These changes are made by currents, which are influenced by the waves developed in the breaking zone and by the direct wave actions through the turbulence caused by the broken waves and by the rising and falling of the water level at the coast. The simultaneous change in the shape of a shore happens due to the sediment transferred by the approached waves and those that are either off or along a shore. Figure 1 shows an example of a coastal cross-section.
In addition to profile changes of the coast caused by waves, if relative changes in the mean sea level occur (just as in most beaches around the world), there would be some changes in the beach profile. At the time of sea level rise along with the profile drowning, when sand is transported off the shore and the Mean Sea Level position on the shoreface moves landward, profile rearrangement occurs. Bruun explain this process and present a method for calculating the distance change of the shoreline upon even a slight rise in the Mean Sea Level [1, 2]. The Bruun rule depends on parameters such as sea level rise, closure depth, the distance from the closure depth to the

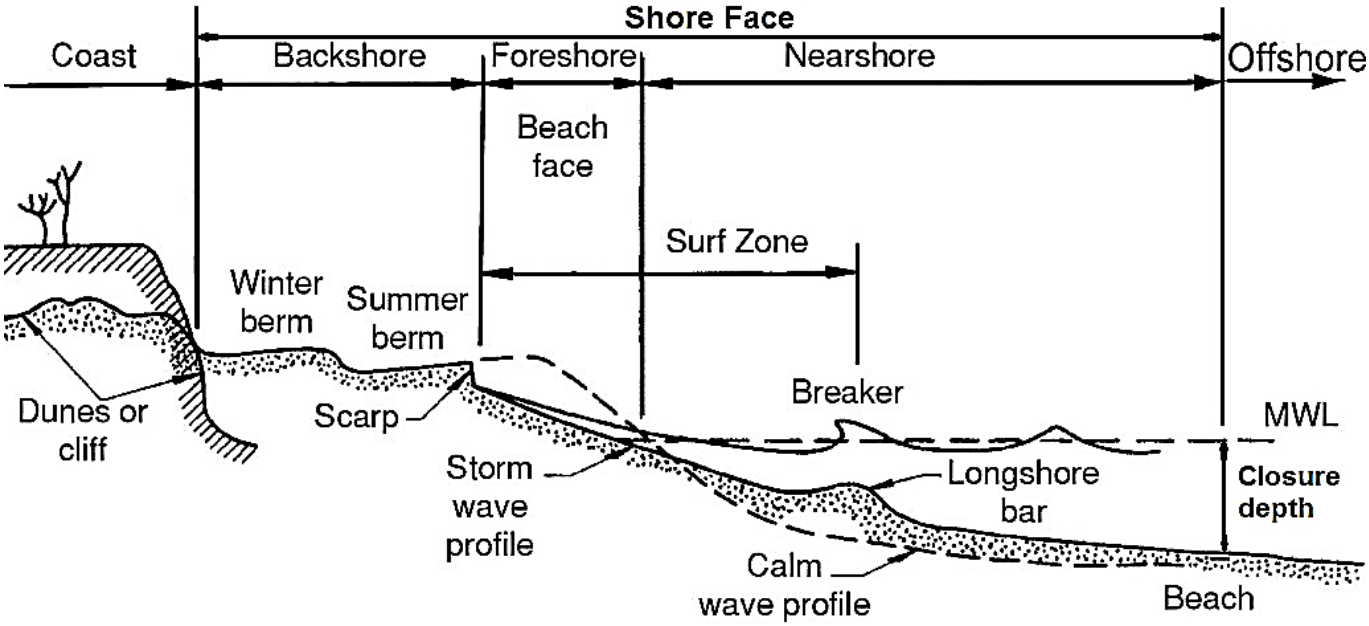


**Figure 1. A typical beach cross-section with details [4]**

shoreline and the maximum run-up height. Also, to improve the predictions made by the Bruun rule, Rosati *et al.* added landward sediment transport, which led to obtaining much-desired results [3].

Changes in shorelines (advancing or retreating) due to the mentioned factors are of great importance in coastal residential areas, especially, ports. Predicting the trend of these changes will determine the future of coastal cities and causes decisions to be made to confront and control the advance of shorelines toward residential areas and to prevent potential damages. Also, it will facilitate more logical planning to be done in terms of designing and the economy of important commercial and fishing ports.

De Winter and Ruessink, examined the effects of sea level rise on the sand dunes with considering XBeach models in their research. According to their studies, with 0.4 meters increase in water level, the volume of eroded beaches of Noordwijk, and Egmon has been reached 52 and 80 $m^3/m$ *per* $m$ respectively [5].

Also, Vitousek *et al.*, developed flexible and multi-faceted model as CoSMoS-COAST to predict long-term changes of shorelines. This model is used to predict changes of the coastline of Southern California (500 km) as a result of sea level rise. According to their forecast, by 0.93 to 2 meters rise in sea level until 2100, about 31 to 67 percent of the coasts of Southern California will be lost [6].

There have been numerous changes in the Caspian Sea level in different times. Sometimes, these changes have had a decreasing trend, while at others; they have been incremental [7]. Since the Caspian Sea level has experienced frequent fluctuations resulting in coastal advance and retreat; therefore, studying and predicting shoreline changes in the Caspian Sea is very important.

Neshaei *et al.* investigate sediment transport by the wind and its effect on changes in the shape of a coast and presented a calibrated model, whose predictions showed reasonable results. These predictions were performed based on three types of selected parameters, which are, average values, minimum values and maximum values. A majority of data points measured by surveying are located within a narrow band obtained by the last two set of model parameters. Using the average values for the model parameters, it showed reasonable predictions regarding to the complexity of the nature of the shoreline profiles [8].

Firoozfar *et al.* examined the behavior of the southern coasts of the Caspian Sea due to sea level changes. In their study, they carried out sedimentary characteristics, coastal hydrography, bed morphology and coastal profile up to a depth of 10 meters in three different periods from the coasts. In their research, they obtained a database of coastal gradients, sedimentary characteristics, and along shore flow patterns of the shoreline. Based on sea level changes and its results, the coastal area of the south of the Caspian Sea was classified into four categories: the west of Guilan province with a gentle slope near the coast and a steep slope in the coastal zone to a depth of 10 meters; the central region of the Guilan province and eastern province of Mazandaran with a steep slope near the coast and a gentle slope in the coastal zone to a depth of 10 meters; the western part of Mazandaran province with a steep slope near the coast and the coastal area to a depth of 10 meters, as well as Golestan province with a very gentle slope in its coastal area [9].

Bruun took the seaward transport of all eroded sand as a result of sea level rise into consideration. Many laboratory experiments have been conducted such as

Schwartz (1967 and 1987), Williams (1978) and Park (2009) [10-13]; and many numerical models have been developed in various studied based on the Bruun rule. These studies are included but not limited to Kobayashi *et al.* (1996), Tega and Kobayashi (2000), Davidson-Arnott (2005), Donnelly *et al.* (2006), Donnelly (2007), Donnelly (2008), Larson *et al.* (2009), Aagaard and Sorensen (2013), Houston and Dean (2014) and Tarigan and Nurzanah (2016) [14-23].

Cooper and Pilkey claim that the Bruun rule is based on incorrect fundamental hypotheses and cannot be used to predict shoreline changes [24]. Kaplin and Selivanov compared the Bruun rule with profile changes of the Caspian Sea during 1978-1991, in which the sea level rise of 1.8-2.5 meter has been noticed. Obtained results indicated that the Bruun rule was well-adapted to changes in shorelines. The authors of this paper assert that in order to reach more accurate results, longshore sediment transport, swash zone and sediments transported by the wind should also be considered in calculations [25].

Based on the Bruun rule, Leatherman *et al.* studied shoreline changes related to the sea level rise in five eastern coasts in the United States. The authors claim that the model proved to be correct; however, its domain was always two times greater than the rate of the sea level rise [26]. Zhang *et al.* conducted a more precise study on the Bruun rule and investigated shoreline changes based on sea level rise in five coasts similar to those studied by Leatherman *et al.*; The authors confirmed the Bruun rule, yet they stated that two zones with lower change rates (Long Island and Delmarva Peninsula) were naturally nourished. Still, no wind-related swash zone and sediment deposition were seen in their studies [27]. With considering Bruun rule, Ranasinghe *et al.* studied the shoreline changes in Australian coasts in terms of sea level rise and estimated that these changes would be less than 8% by the year 2100 [28].

## 2. Methods

Bruun proposed an equation based on the equilibrium of eroded and deposited volume of cross-shore sediment transport [1]. The equation can predict shoreline changes based on sea level changes. Besides the eroded and deposition volume in a coastal region, Rosati *et al.* considered the landward sediment deposition volume as well [3].

### 2.1. The Bruun Rule

The Bruun rule considers the horizontal changes in a shoreline to be related to sea level changes, closure depth, the distance from the closure depth to the shoreline and of the maximum advancing of waves at the swash zone. Thus, the following equation has been suggested [1, 2]:

$$R_B = S\,\frac{W_*}{h_c + B} \tag{1}$$

Where, $R_B$ is horizontal changes of shoreline (Bruun Rule), $S$ is changes in the sea level, $B$ is maximum run-up height and $h_c$ and $W_*$ are closure depth and the active profile length after sea level changes, respectively. $W_*$ can be obtained from the following equation:

$$W_* = W + R_B \tag{2}$$

Where, $W$ is active profile length before sea level changes. The Bruun rule's details are shown in Figure 2. To calculate the closure depth, the Coastal Engineering Research Center suggests the following relation [29]:

$$h_c = 6.75 H_s \tag{3}$$

$H_s$ is significant wave height in deep waters.

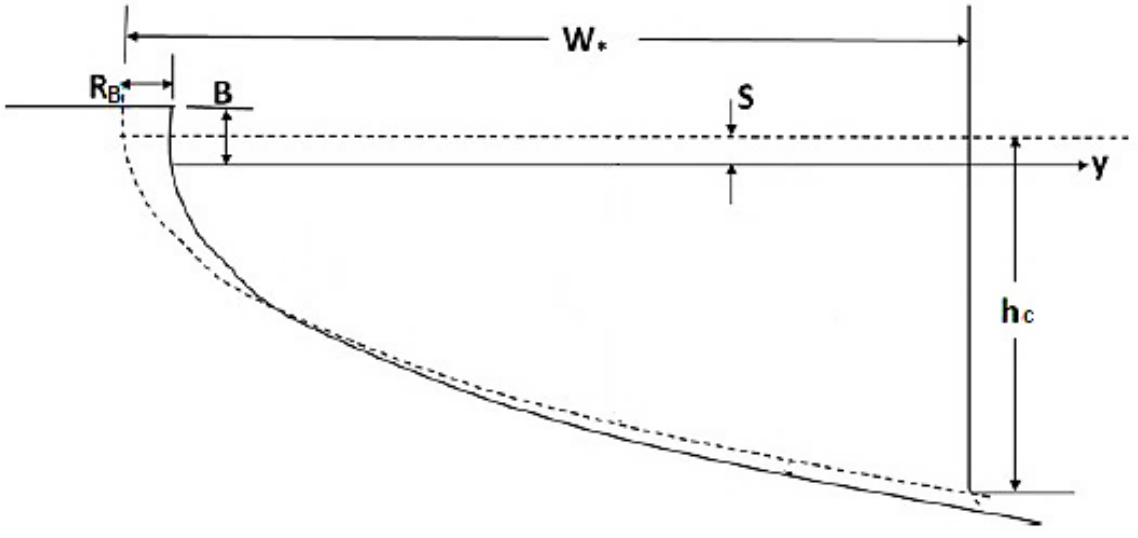


**Figure 2. Bruun Rule definitions [1, 2]**

The maximum run-up height can also be calculated by using the following equation [30]:

$$B = \frac{U_0^2}{2g} \tag{4}$$

Where, $g$ is acceleration of gravity and $U_0$ is initial velocity of water on the shoreline, which is calculated using the following equation:

$$U_0 = C\sqrt{gH_B} \tag{5}$$

In this equation, $H_B$ represent mean wave height in the breaker zone and $C$ is Froude number. A natural beach is under the influence of wave breaking mechanism, and the value of $C \approx 1.4$ seems to be typical according to the results provided by Svendsen *et al.* [31]. Based on more laboratory studies, the value of $C$ is between 1.18 and 1.48 [32, 33].

### 2.2. The Modified Bruun Rule Extended for Landward Transport

After conducting field studies in eastern coasts of Florida and analyzing the Bruun rule, Rosati *et al.* conclude that at the time of sea level rise both seaward and landward sediment transport will occur. With consideration of the landward sediment transport hypotheses that were put forward by Rosati *et al.*, the shoreline changes after changes in the sea level can be calculated using the following equation [3]:

$$R_R = \left(W_* + \frac{V_D}{S}\right) Ln\left(\frac{h_c + B}{h_c + B - S}\right) \approx S\,\frac{W_* + V_D/S}{h_c + B} \tag{6}$$

Where, $R_R$ is horizontal changes of a shoreline (The Modified Bruun Rule Extended for Landward Transport by Rosati *et al.*) and $V_D$ is volume per unit length of the landward deposition that is equal to $y_L \times S$, where $y_L$ is width of landward sediment transport [3]. Based on Rosati *et al.* equations, characteristics of profile changes, which occurred after sea level rise can be seen in Figure 3.

## 3. Study Area

With its natural and regional conditions, the Caspian Sea is one of the best places to conduct coastal engineering studies. Numerous sea level changes during a short periods of time have made it attractive for conducting studies on beach profile and shoreline changes that happen due to sea level rise and fall. Therefore, the Caspian Sea can be considered a large-scale natural laboratory model. The Caspian Sea coast in Dastak and Anzali regions are shown in Figure 4.

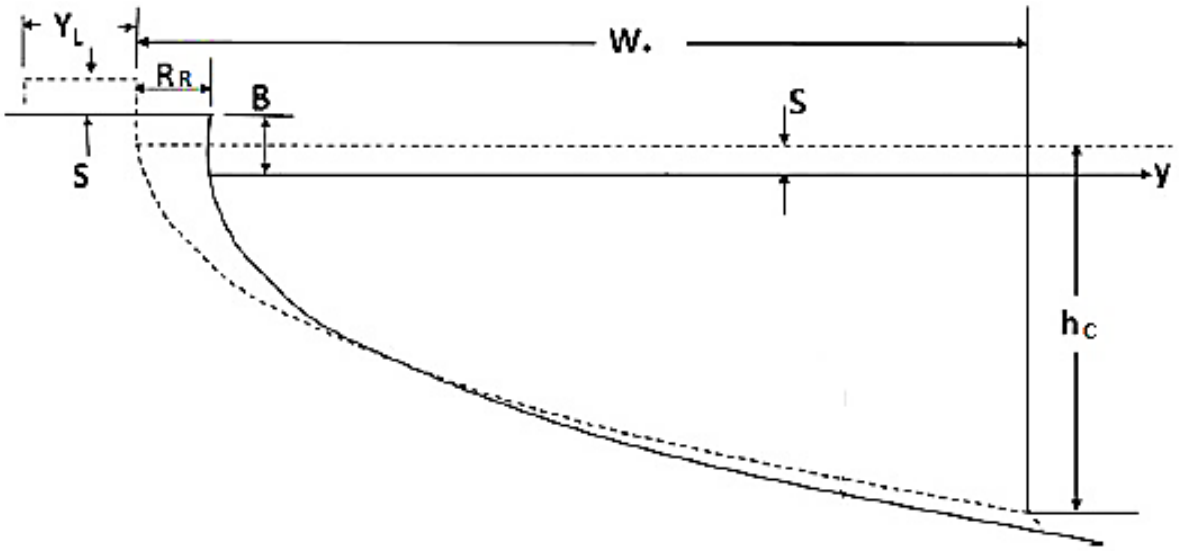


**Figure 3. Characteristics of profile changes after the sea level rise [3]**


**Figure 4. Caspian Sea Coasts in the Dastak and Anzali Zones**

In order to investigate the relation suggested by Bruun and Rosati *et al.* in a more accurate way, necessary information such as mean grain size ($D_{50}$), sea level changes ($S$) and cross-section profiles of the southern coasts were collected from Anzali and Dastak coastal regions in Guilan province, Namakabrood, Mahmudabad and Larim in Mazandaran province and also from Miankaleh in Golestan province during the 2013-2015 periods by the Caspian Sea National Research Center report [33]. The southern part of the Caspian Sea and the studied coasts can be seen in Figure 5.

Data for the Caspian Sea waves, including the height of waves and their corresponding periods in deep waters and a wave's breaker zone with a return period of 3 years were used from the Ports and Maritime Organization [34]. Information about the mean sediment particle size, sea level change and wave information have been given in Table 1.


**Figure 5. The southern part of the Caspian Sea and the studied coasts**

**Table 1. Measured data of the southern areas of the Caspian Sea [7, 33, 34]**

| Parameter/Zone | Anzali | Dastak | Namakabrood | Mahmudabad | Larim | Miankaleh |
|---|---|---|---|---|---|---|
| $D_{50}$ (*mm*) | 0.2 | 0.19 | 0.23 | 0.19 | 0.17 | 0.17 |
| S (2013 to 2015) (*m*) | -0.132 | -0.132 | -0.132 | -0.132 | -0.132 | -0.132 |
| $y_L$ (*m*) | 154.5 | 174.5 | 115 | 160.5 | 199 | 100 |
| $H_S$ (*m*) | 0.71 | 0.71 | 0.65 | 0.65 | 0.67 | 0.67 |
| $T_0$ (*Sec*) | 4.86 | 4.86 | 4.25 | 4.25 | 4.7 | 4.7 |
| $H_{B\ max}$ (*m*) | 5.22 | 5.22 | 5.12 | 5.12 | 4.79 | 4.79 |
| $H_B$ (*m*) | 0.68 | 0.68 | 0.65 | 0.65 | 0.66 | 0.66 |
| $T_{BP}$ (*Sec*) | 13.1 | 13.1 | 11.9 | 11.9 | 12.19 | 12.19 |
| $T_B$ (*Sec*) | 4.87 | 4.87 | 4.26 | 4.26 | 4.72 | 4.72 |

In Table 1, $H_S$ is significant wave height in deep waters, $T_0$ is mean wave period in deep waters, $H_{B\ max}$ is maximum wave height in the breaker zone, $H_B$ is mean wave height in the breaker zone, $T_{BP}$ is maximum wave period in the breaker zone and $T_B$ represent mean wave period in the breaker zone. As it can be seen in Table 1, the mean particle size in the Caspian Sea coasts is about 0.0002 meters. With consideration of the data from the 3-year return period in the southern coasts of the Caspian Sea, the maximum wave height in the breaker zone would be about 5 meters. These shows that the Caspian Sea has a fairly stormy nature. Under natural conditions and taking waves' mean characteristics value into consideration for a 3-year period, the wave height in deep water is almost 0.67 meter with a period of 4.7 seconds, which is an indication of the Caspian Sea's normal behavior under normal and calm weather conditions.

## 4. Results

### 4.1. Bruun Rule and Landward Transport Analysis

To calculate the closure depth, Eq. (3) can be used. This equation has been suggested by the Coastal Engineering Research Center [10]. The outputs indicate the logical prediction of this equation. After calculating the closure depth, its distance from the shoreline was calculated based on the 2013 profiles. Also, the natural slope of the coast could be calculated based on closure depth values and their distance from the shoreline.

To calculate the maximum run-up height (Eq. 4), the initial velocity of water at the shoreline (Eq. 5) should also be calculated. This velocity is a function of the acceleration of gravity, wave height and the coefficient which depends on the bore collapse (Froude number) in the breaker zone. In order to estimate the bore collapse coefficient, some simplification conditions were considered, in which the value of the coefficient *C* was 1.4. Closure depth (Eq. 3), the horizontal distance of the closure depth from shoreline, the natural slope of the coast ($S_0$), the initial velocity of water in the shoreline and the maximum run-up height are presented in Table 2.

As it can be seen in Table 2, based on the equations, the water depth at the end of the active coastal zone is predicted to be about 4.5 meters. The horizontal distances of the closure depth from the shoreline in Mahmudabad and Namakabrood shores are less due to their steeper slopes in comparison with other zones. Also, a gentler slope at Miankaleh coasts leads to longer distances of the closure depth from the shoreline. It is shown that the maximum run-up height is near 0.65 meters. The values obtained for all coasts are close to this one.

The main difference between the Caspian Sea and open seas is in the way its sea level changes. As the data show, open seas are continually experiencing rises in their levels, whereas in the Caspian Sea, there are periods of both sea level rise and fall; From 1977 to 1995, the sea experienced a rise of 2.4 meters, while from 1995 to 2014, it experienced 0.8 meter fall [7]. These sea level fluctuations are shown in Figure 6.

**Table 2. The calculated parameters of the Caspian Sea**

| Parameter/Zone | Anzali | Dastak | Namakabrood | Mahmudabad | Larim | Miankaleh |
|---|---|---|---|---|---|---|
| $h_c$ (*m*) | 4.793 | 4.793 | 4.388 | 4.388 | 4.523 | 4.523 |
| W (*m*) | 454.44 | 451.04 | 327.86 | 296.80 | 454.86 | 885.36 |
| $S_0$ | 0.011 | 0.011 | 0.013 | 0.015 | 0.010 | 0.005 |
| C | 1.4 | 1.4 | 1.4 | 1.4 | 1.4 | 1.4 |
| $U_0$ (*m/s*) | 3.615 | 3.615 | 3.535 | 3.535 | 3.562 | 3.562 |
| B (*m*) | 0.666 | 0.666 | 0.637 | 0.637 | 0.647 | 0.647 |

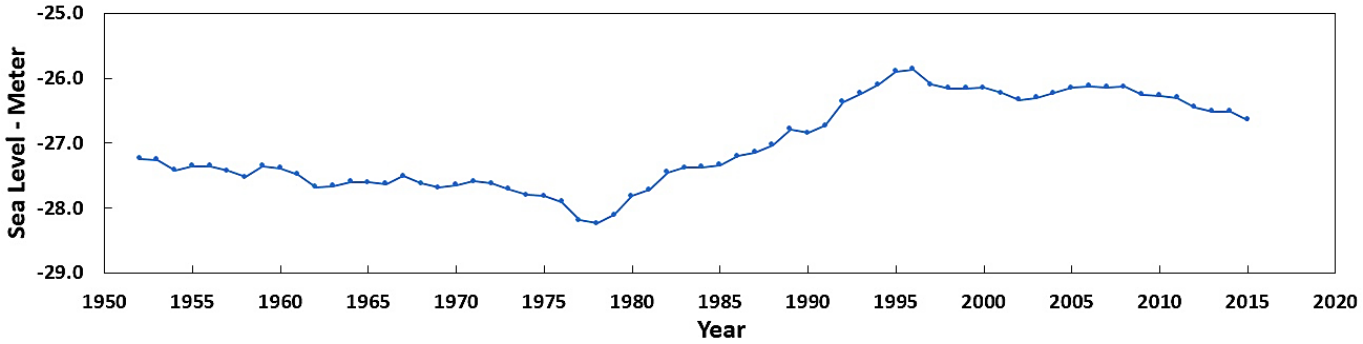


**Figure 6. 60 years of the Caspian Sea level change according to the high sea level [7]**

### 4.2. Adjustment of the Bruun Rule with Sea Level Fall Conditions

In order to investigate and apply the effects of sea level fall in the Eq.'s (1) and (6), the basic and simplified assumptions can be made to calculate the Bruun theory based on the volume of sediment deposition and accumulation as follows:

$$\Delta V_{-} = \Delta V_{+} \Rightarrow R_B \times (h_c + B) = S \times (W + R_B) \qquad (7)$$

$$\Delta V_{-} = \Delta V_{+} \Rightarrow R_R \times (h_c + B) = S \times (W + R_R) + S \times y_L \qquad (8)$$

Eq. (7) related to Bruun's theory and Eq. (8) related to the modified Bruun Rule theory by Rosati *et al.*

By considering simplified assumptions in Eq.'s (7) and (8) in terms of sea level fall and due to the insignificance of the changes in water level to the closure depth, the vertical elevation of the water as well as the advance of the shoreline, the left terms of the above equations can stay unchanged. Hence, it can be assumed that under the conditions of sea level fall, the volume of washed-out sediments will act as the conditions for rising sea levels.

Due to the fact that in the new conditions (the reduction of sea level), in spite of increasing sea level, the shoreline progresses; therefore, in the right side of Eq.'s (7) and (8) (in the section of sediment accumulated in the sea bed), the terms $S \times (W + R_B)$ and $S \times (W + R_R)$ change to $S \times (W - R_B)$ and $S \times (W - R_R)$. Other terms on the left side of the equations can be considered unchanged. In order to get better understanding the process of reducing the sea level and shoreline changes are shown in Figure 7 by some simplification.

Figure 8 shows shoreline changes in the profiles measured in the studied coasts. Also, values of shoreline changes based on the Bruun Rule, the modified Bruun rule extended for landward transport and the shoreline changes based on profiles measured during the 2013-2015 period and the difference between shoreline changes measured and calculated from Eq.'s (1) and (6) are given in Table 3.

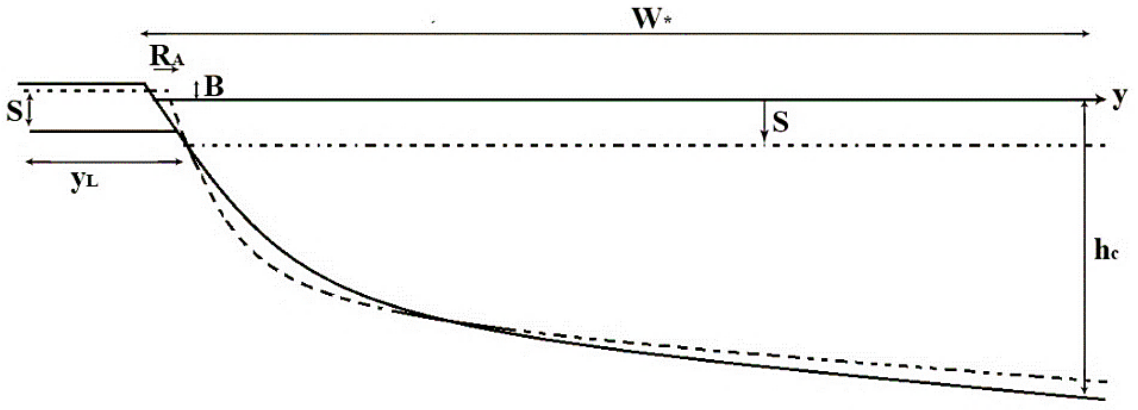


**Figure 7. Characteristics of profile changes after the sea level fall**

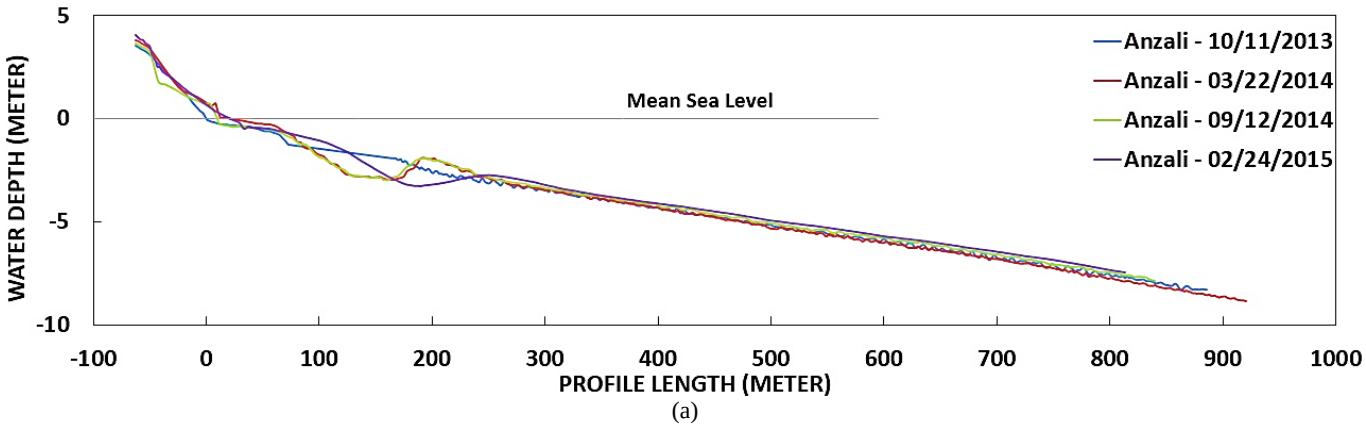


(a)

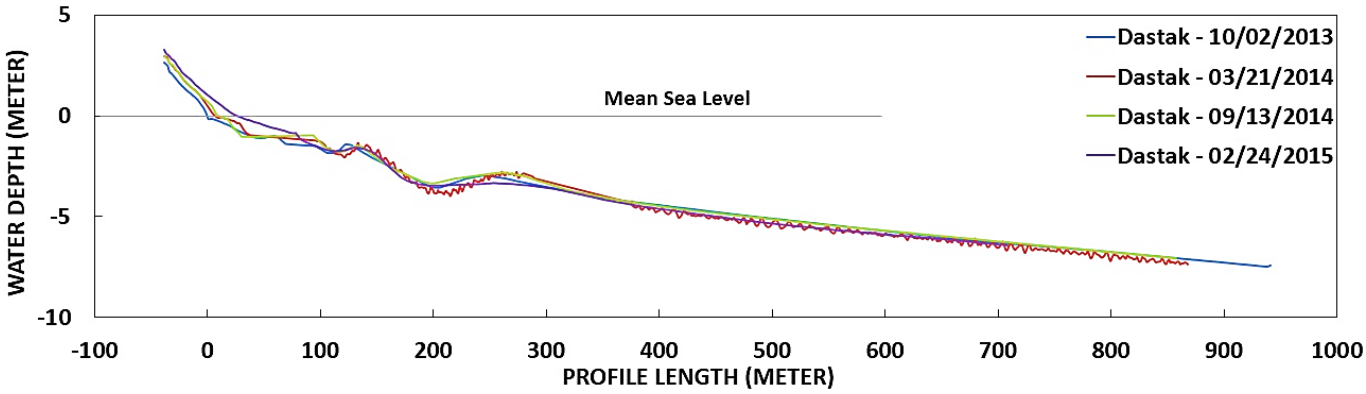


(b)

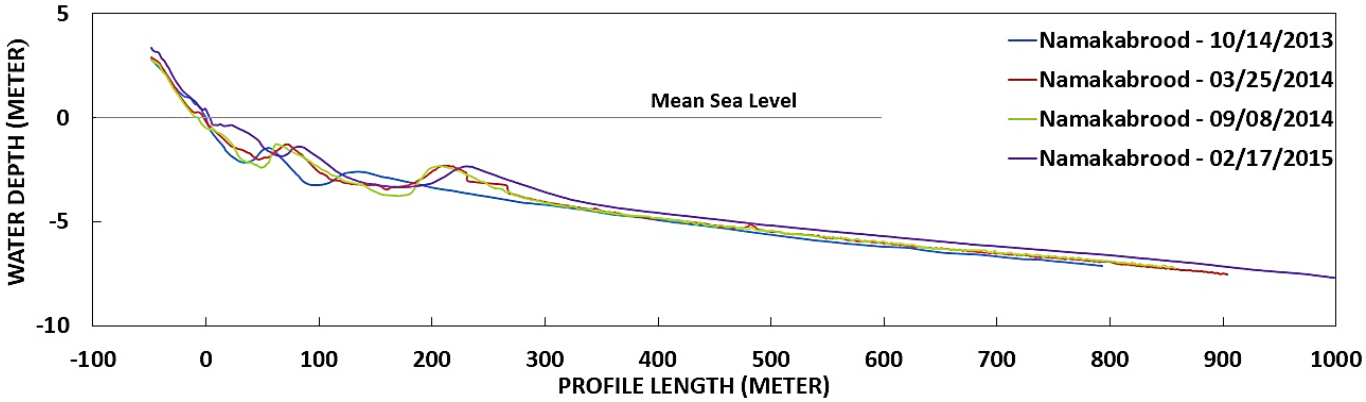


(c)

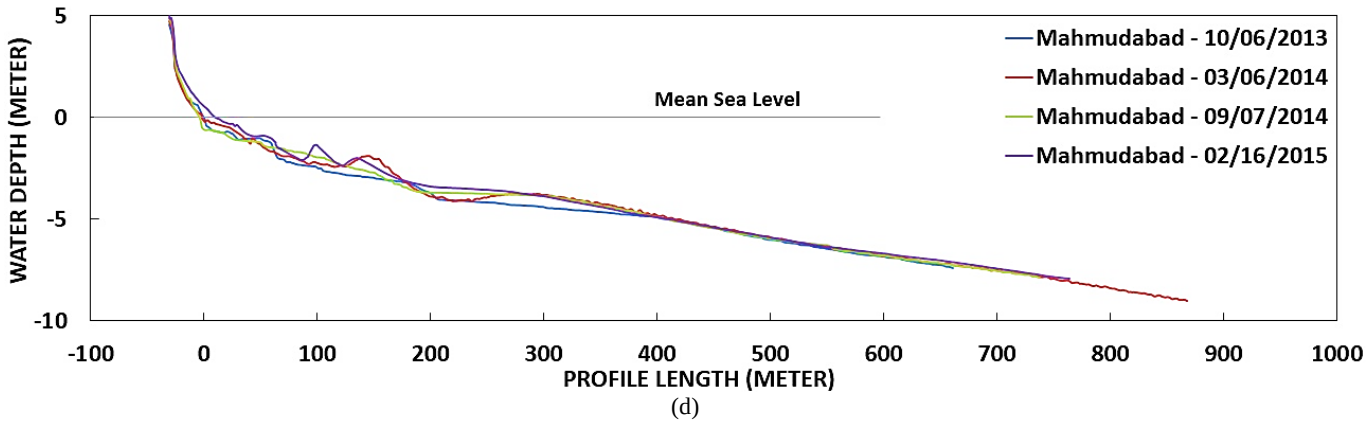


(d)

**Figure 8. Shoreline variations for observed profiles in the studied coasts; a) Anzali, b) Dastak, c) Namakabrood, d) Mahmudabad, e) Larim, f) Miankaleh**

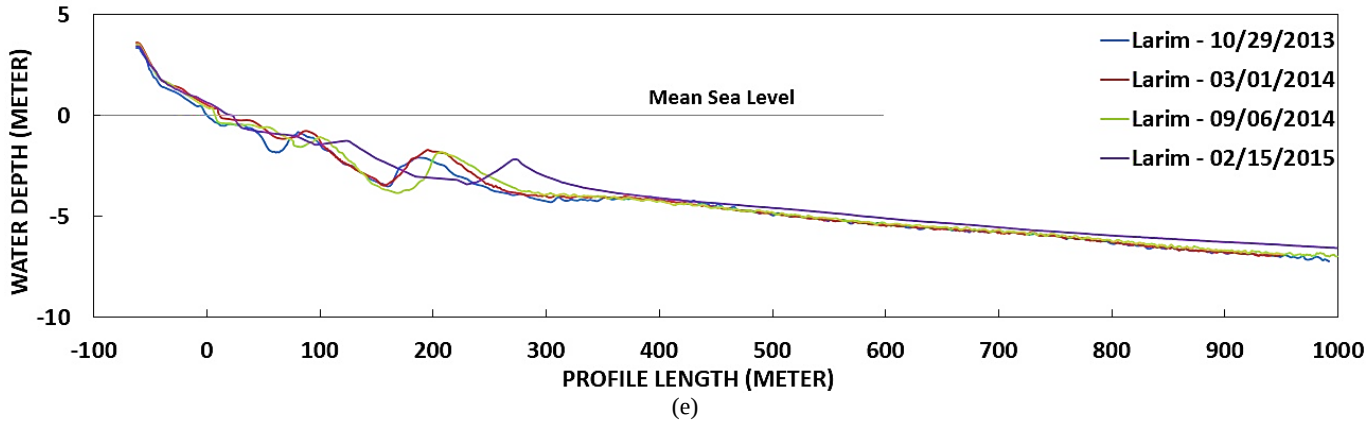


(e)

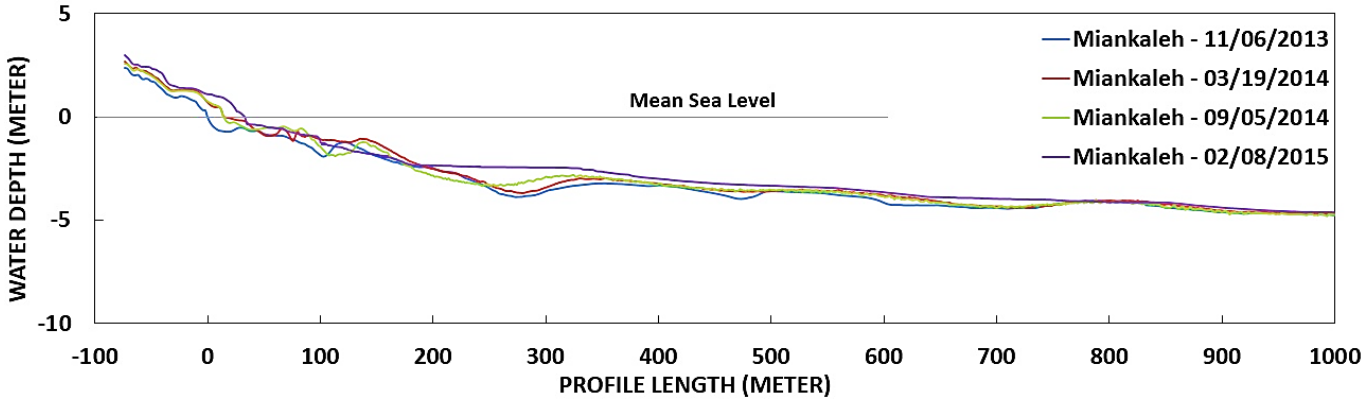


(f)

**Figure 8. Shoreline variations of observed profiles in the studied coasts; a) Anzali, b) Dastak, c) Namakabrood, d) Mahmudabad, e) Larim, f) Miankaleh - Continue**

**Table 3. Calculated parameters of shoreline changes according to Bruun Rule, it's modified for landward transport, Shoreline changes based on the obtained profiles during the years 2013 to 2015**

| Parameter/Zone | Anzali | Dastak | Namakabrood | Mahmudabad | Larim | Miankaleh |
|---|---|---|---|---|---|---|
| $R_{Natural}$ ($m$) | 11.367 | 20.479 | 6.322 | 11.919 | 16.491 | 23.298 |
| $R_B$ ($m$) | 10.729 | 10.649 | 8.392 | 7.597 | 11.324 | 22.042 |
| $R_R$ ($m$) | 14.377 | 14.769 | 11.336 | 11.705 | 16.279 | 24.532 |
| $R_{Natural}$ - $R_B$ ($m$) | 0.638 | 9.830 | 2.070 | 4.322 | 5.167 | 1.256 |
| $R_{Natural}$ - $R_R$ ($m$) | 3.010 | 5.710 | 5.014 | 0.214 | 0.212 | 1.234 |

In Table 3, the calculated values of the difference between the natural change of the shoreline and the shoreline correction calculated based on equations in a positive state (absolute value) are given in the last two rows of the table.

With the results obtained from Table 3, prediction of shoreline changes based on the Bruun Rule in all coasts except Namakabrood is less than its measured value, while given the values of sediment deposition in Anzali, Namakabrood and Miankaleh coasts, the modified Bruun rule extended for landward transport, predicts changes to be more than their natural limits. Moreover, in Root Mean Square Error (RMSE), it is observed that the prediction error for shoreline changes based on the equation given by Rosati *et al.* would be smaller than the Bruun's equation [35].

$$RMSE = \sqrt{\frac{\sum_{i=1}^{n}\left(R_{Natural} - R_{B,or,R}\right)^2}{n_{\text{Numbers of data}}}} \quad (9)$$

Based on Eq. (7), the RMSE for horizontal changes of shoreline of the Bruun rule and the modified Bruun rule extended for landward transport would be 4.971 and 3.377 meters, respectively, i.e. a difference of 1.594-meter between these equations and a higher accuracy of the equation suggested by Rosati *et al.*, which would make the prediction closer to reality.

As it can be seen in the previous investigations, equations for shoreline changes have been defined based on sea level rise. However, these equations have shown good results under the conditions, when the level of the Caspian Sea falls as well. In order to improve the prediction of Rosati *et al.* equation and to optimize it, basic parameters that play a fundamental role in the behavior of the profile and shorelines have

been studied. For this reason, basic parameters such as mean grain size ($D_{50}$), sediment scale parameter ($A$) and natural slope of a coastal region ($S_0$), which are among effective factors related to wave height in a coastal region, have been examined against the mean wave height in the breaker zone ($H_B$).

The natural slope of a coast at its shallow zone is one of the factors that play a significant role in determining the location of the waves break. Also, particle size of the bed and type of particles play an important role in waves' break, when the waves come (in contact with the seabed according to their domains) at the shallow zone [36, 37]. When waves carry sediment particles of different gradations and create erosion at the seabed, this process affects their energy, height and their break. Sediment scale parameter also depends on the seabed particle size and particle deposition velocity, which would affect wave height in the breaker zone [38, 39].

In this research a coefficient was applied, which depends on the mean wave height in the breaker zone and the particle size of the bed, in the equation for the prediction of shoreline changes, it would become as follows:

$$R_A = A_s \times \frac{S\left(W_* + {V_D}/{S}\right)}{h_c + B} \qquad (10)$$

In the above equation, $R_A$ is horizontal changes of shoreline that modified in this research and $A_s$ is a coefficient, which depends on mean wave height in the breaker zone and the mean particle size of the bed and could be obtained from the following equation:

$$A_s = 2.963\times10^{-4}\left(\frac{H_B}{D_{50}}\right) \qquad (11)$$

The number $2.963\times10^{-4}$ in above equation is intended as a calibration that optimized coefficient was extracted using coding in MATLAB software with trial and error method. Therefore, the prediction of shoreline changes that were obtained from the studied regions using the modified equation of Rosati *et al.* has been given in Table 4.

As it can be observed in Table 4, by applying $A_s$ coefficient into the equation, the prediction of shoreline changes is obtained with similar error compared to before applying this coefficient (Table 3). After applying this coefficient into the equation, predictions for three regions, Dastak, Namakabrood and Mahmudabad became better acceptable in comparison with the primary equation presented by Rosati *et al.* and the values were closer to the actual data. In Anzali region, due to the fact that measured profiles were near breakwaters at the port and Anzali lagoon, the predictions were overestimate than those of the primary equation. Due to the sediment regime of this region, the existence of breakwaters and the lagoon near the place, in the areas where profiles are measured, the calculated errors has increased.

The increase in the prediction of shoreline variation within the Miankaleh area is also due to the fact that the field measurement area is close to the Amirabad and Neka ports; the presence of these two ports impairs the natural functioning of the coast due to environmental factors.

In general, no change was made by applying the $A_s$ coefficient to Eq. (6) in the mean square error value for all areas under study (the root mean square error of the difference in predictions based on Eq.'s (6) and (10) is equal to 3.377 and 3.447 meters);

Nevertheless, by applying this coefficient (applying the parameters of the mean size of sediment particles and the mean height of the waves in the breaking area) and providing optimized Eq. (10), the shoreline changes for all studied regions are become more logical and acceptable.

The difference in forecasting the shoreline variation has not reached up to 5 meters on any of the coasts; while, according to the Bruun equation, the predicted difference for the shores of Dastak and Larim are 9.830 and 5.167 meters respectively and based on Rosati *et al.* the predicted difference for shores of Dastak and Namakabrood are 5.710 and 5.014 meters, respectively.

Based on the results presented in Table 4, the least difference in prediction is related to Mahmudabad shore and the most difference in prediction is related to the Dastak shore, which is respectively 0.059 and 4.849 meters.

Based on improvement for forecasting shoreline changes by applying the $A_s$ coefficient and not having much difference in calculating root mean square error based on the Rosati *et al.* proposed equation, we can use Eq. (10) as an optimized equation in terms of sea level fall.

**Table 4. Calculated parameters of shoreline variations according to the modified Bruun Rule extended for landward transport after *As* coefficient applying and shoreline changes based on the obtained profiles during the years 2013 to 2015**

| Parameter/Zone | Anzali | Dastak | Namakabrood | Mahmudabad | Larim | Miankaleh |
|---|---|---|---|---|---|---|
| $R_{Natural}$ ($m$) | 11.367 | 20.479 | 6.322 | 11.919 | 16.491 | 23.298 |
| $R_A$ ($m$) | 14.480 | 15.639 | 9.531 | 11.861 | 18.656 | 28.115 |
| $R_{Natural} - R_A$ ($m$) | 3.113 | 4.849 | 3.208 | 0.059 | 2.159 | 4.812 |
| **RMSE ($m$)** | | | | 3.447 | | |

## 5. Conclusions

In order to predict shoreline changes due to sea level rise, presented and developed an equation, in which shoreline changes were related to parameters such as sea level rise, closure depth, the distance from the closure depth to a shoreline and the maximum run-up height. Many relevant laboratory and field studies have been conducted. These results indicated that the Bruun rule gave a logical prediction. This rule was investigated and analyzed in this research and with consideration of the Caspian Sea level fall, good predictions were made in the studied regions. Minimum and maximum prediction differences for shorelines were 0.638 and 9.830 meters, respectively, compared with the actual values that illustrated on the profile figures. The obtained RMSE value was 4.971 meters.

Following extensive investigations, Rosati *et al.* concluded that landward sediment transport played a significant role in determining shorelines and by applying it into the Bruun rule equation, prediction of shoreline changes could be improved. The equation suggested by Rosati *et al.* was completely investigated in this research and analyses indicated even more desirable predictions compared with those of the Bruun rule. In this study, minimum and maximum prediction differences for shoreline advances were 0.212 and 5.710 meters, respectively in comparison with their actual values and the obtained RMSE value was 3.377 meters.

In order to improve predictions, the $A_s$ coefficient was defined. This coefficient is related to the mean wave height in the breaker zone and the mean particle size of the seabed.

In terms of water level fall, by applying the $A_s$ coefficient, the mean squared error to predict shore changes in compare to its natural variation was obtained 3.447, which did not make a large change in the mean squared error of the values obtained from Rosati *et al.*

However, according to the results, the least difference in prediction is for the Mahmoodabad coast and the greatest difference in prediction is related to the Dastak coast, which is respectively 0.059 and 4.849 meters, which makes the range of predictions difference less and more logical compared to Rosati *et al.*

The difference in forecasting the shoreline variation has not reached up to 5 meters on any of the coasts; while, according to the Bruun equation, the predicted difference for the shores of Dastak and Larim is 9.830 and 5.167 meters respectively and based on Rosati *et al.* The predicted difference for shores of Dastak and Namakabrood is 5.710 and 5.014 meters, respectively.

Based on the improvement for forecasting shoreline changes by applying the $A_s$ coefficient and not having much difference in calculating the root mean square error based on the Rosati *et al.* equation, we can use the proposed equation in this study to predict shoreline changes as an optimized equation in terms of sea level fall.

## Acknowledgements

We would like to thank our fellow researchers at the Caspian Sea National Research Center and the Ports and Marine Administration of Guilan Province for providing us with the information we needed about the Caspian Sea and Mr. Malek (Head of the Caspian Sea National Research Center) and Mr. Salimi (Ports and Marine Administration of Guilan Province-Department of Hydrography) for making necessary arrangements for us so that we could collect information. We also appreciate Mr. Mohammadikhah (Ph.D. student of Mechanical Engineering for Energy Conversion at University of Guilan) for providing his knowledge for objectives of this research.

## Reference

1- Bruun, P., (1954), *Coast erosion and the development of beach profiles*, U.S. Army Corps of Engineers, Beach Erosion Board, Tech. Memo. No. 44.

2- Bruun, P., (1962), *Sea-level rise as a cause of shore erosion*. Journal of the Waterways and Harbors division, 88(1), 117-132.

3- Rosati, J.D.; Dean, R.G., and Walton, T.L., (2013), *The modified Bruun Rule extended for landward transport*. Marine Geology, 340, 71-81.

4- Sorensen, R.M., (2006), *Basic coastal engineering, Third Edition (Vol. 10)*. Springer Science & Business Media, Printed in the United States of America.

5- de Winter, R.C., and Ruessink, B.G., (2017), *Sensitivity analysis of climate change impacts on dune erosion: case study for the Dutch Holland coast*. Climatic Change, 141(4), 685-701.

6- Vitousek, S.; Barnard, P.L.; Limber, P.; Erikson, L., and Cole, B., (2017), *A model integrating longshore and cross- shore processes for predicting long- term shoreline response to climate change*. Journal of Geophysical Research: Earth Surface.

7- PMO report, (2016), *Caspian Sea Level Changes*. Ministry of Roads & Urban development of I.R. Iran. http://www.pmo.ir/en/home.

8- Neshaei, M.A.L.; Veiskarami, M., and Nadimy, S., (2011), *Computation of shoreline change: A transient cross-shore sediment transport approach*. International Journal of Physical Sciences, 6(24), 5822-5830.

9- Firoozfar, A., Bromhead, E. N., Dykes, A. P., & Neshaei, M. A. L. (2012), *Southern Caspian Sea coasts, morphology, sediment characteristics, and sea level change*. In Proceedings of the Annual International Conference on Soils, Sediments, Water and Energy (Vol. 17, No. 1, p. 12).

10- Schwartz, M.L., (1967), *The Bruun theory of sea-level rise as a cause of shore erosion*. The journal of Geology, 76-92.
11- Schwartz, M.L., (1987), *Editorial: The Bruun Rule. Twenty Years Later*. Journal of Coastal Research, ii-iv.
12- Williams, P.J., (1978), *Laboratory development of a predictive relationship for washover volume on barrier island coastlines*. Master thesis, Department of Civil Engineering, University of Delaware, Network, DE, 154p.
13- Park, Y.H., (2009), *Overwash induced by storm conditions*. Doctoral dissertation.
14- Kobayashi, N.; Tega, Y., and Hancock, M.W., (1996), *Wave reflection and overwash of dunes*. Journal of Waterway, Port, Coastal, and Ocean Engineering, 122(3), 150-153.
15- Tega, Y., and Kobayashi, N., (2000), *Dune profile evolution due to overwash*. Coastal Engineering, 2000. 2634-2647.
16- Davidson-Arnott, R.G., (2005), *Conceptual model of the effects of sea level rise on sandy coasts*. Journal of Coastal Research, 1166-1172.
17- Donnelly, C.; Kraus, N., and Larson, M., (2006), *State of knowledge on measurement and modeling of coastal overwash*. Journal of Coastal Research, 965-991.
18- Donnelly, C., (2007), *Morphologic change by overwash: establishing and evaluating predictors*. Journal of Coastal Research, (SI 50 (special issue)), 520-526.
19- Donnelly, C., (2008), *Coastal overwash: processes and modeling*. Report LUTVDG/(TVVR-1043).
20- Larson, M.; Donnelly, C.; Jimenez, J., and Hanson, H., (2009), *Analytical model of beach erosion and overwash during storms*. Proceedings of the ICE-Maritime Engineering, 162(3), 115-125.
21- Aagaard, T., and Sorensen, P., (2013), *Sea level rise and the sediment budget of an eroding barrier on the Danish North Sea coast*. Journal of Coastal Research, 65(sp1), 434-439.
22- Houston, J.R., and Dean, R.G., (2014), *Shoreline change on the east coast of Florida*. Journal of Coastal Research, 30(4), 647-660.
23- Tarigan, A.P.M., and Nurzanah, W., (2016), *The Shoreline Retreat and Spatial Analysis over the Coastal Water of Belawan*, INSIST, 1(1), 65-69.
24- Cooper, J.A.G., and Pilkey, O.H., (2004), *Sea-level rise and shoreline retreat: time to abandon the Bruun Rule*. Global and planetary change, 43(3), 157-171.
25- Kaplin, P.A., and Selivanov, A.O., (1995), *Recent coastal evolution of the Caspian Sea as a natural model for coastal responses to the possible acceleration of global sea-level rise*. Marine Geology, 124(1), 161-175.
26- Leatherman, S.P.; Zhang, K., and Douglas, B.C., (2000), *Sea level rise shown to drive coastal erosion*. Eos, Transactions American Geophysical Union, 81(6), 55-57.
27- Zhang, K.; Douglas, B.C., and Leatherman, S.P., (2004), *Global warming and coastal erosion*. Climatic Change, 64(1-2), 41-58.
28- Ranasinghe, R.; Callaghan, D., and Stive, M.J., (2012), *Estimating coastal recession due to sea level rise: beyond the Bruun rule*. Climatic Change, 110(3-4), 561-574.
29- Coastal Engineering Research Center, (2006), *Coastal engineering manual*. United States, Army., U.S. Government Printing Office, Washington DC 20314-1000.
30- Baldock, T.E., and Holmes, P., (1999), *Simulation and prediction of swash oscillations on a steep beach*. Coastal Engineering, 36(3), 219-242.
31- Svendsen, I.A.; Madsen, P.A., and Hansen, J.B., (1978), *Wave characteristics in the surf zone*. Coastal Engineering Proceedings, 1(16).
32- Yeh, H.H.; Ghazali, A., and Marton, I., (1989), *Experimental study of bore run-up*. Journal of Fluid Mechanics, 206, pp.563-578.
33- Caspian Sea National Research Center report, (2016), *Caspian Sea Profiles*. Water Research Institute, Ministry of Energy of I.R. Iran. http://wri.ac.ir/csnrc.
34- PMO, (2009), *Waves modeling of Iranian seas; first volume: Caspian Sea*. (In Persian).
35- Willmott, C.J., and Matsuura, K., (2005), *Advantages of the mean absolute error (MAE) over the root mean square error (RMSE) in assessing average model performance*. Climate research, 30(1), 79.
36- Sunamura, T., and Horikawa, K., (1975), *Two dimensional beach transformation due to waves*. Coastal Engineering, (pp. 920-938).
37- Aagaard, T., (2014), *Sediment supply to beaches: cross‐shore sand transport on the lower shoreface*. Journal of Geophysical Research: Earth Surface, 119(4), 913-926.
38- Nordstrom, K.F., (1977), *The use of grain size statistics to distinguish between high-and moderate-energy beach environments*. Journal of Sedimentary Research, 47(3).
39- Aagaard, T., and Sorensen, P., (2012), *Coastal profile response to sea level rise: a process‐based approach*. Earth Surface Processes and Landforms, 37(3), 354-362.

INTERNATIONAL JOURNAL OF
COASTAL & OFFSHORE ENGINEERING IJCOE Vol.3/No. 3/Autumn 2018 (13-17)

Available online at: http://ijcoe.org/browse.php?a_code=A-10-137-3&sid=1&slc_lang=en

# Dispersion Simulation of Cesium-137 Released From a Hypothetical Accident at the Bushehr Nuclear Power Plant in Persian Gulf

**Atiyeh Kamyab[1], Masoud Torabi Azad[2*], Mahdi Sadeghi[3], Ahmad Akhound[1]**

[1] *Physics Department, Payame Noor University, Tehran, Iran, P.O. Box 19395-3697*
[2*] *North Tehran Branch, Islamic Azad University, Tehran, Iran (Corresponding Author)M_Azad@Iau-tnb.ac.ir*
[3] *Medical Physics Department, School of Medicine, Iran University of Medical Science, P.O. Box: 14155-6183, Tehran, Iran*

**ARTICLE INFO**

*Article History:*
Received: 15 Nov. 2018
Accepted: 13 Dec. 2018

*Keywords:*
Cesium-137
Dispersion
CROM model
Bushehr
Persian Gulf

**ABSTRACT**

The nuclear disasters in Chernobyl and Fukushima have shown that such nuclear incidents are causing serious and undesirable long-term damage to the environment and the health of living beings, including humans. So that they should be taken very seriously. Considering the importance of the subject, in this paper, the simulation of the transmission and emission of cesium 137 nuclear abandoned from the contingency incident of Bushehr Power Plant in the Persian Gulf using the CROM (Código de cRiba para evaluaciÓn de iMpacto) code has been discussed. We assumed that the incident took place on July 1, 2018, and the most dangerous and an important nucleus of the abandoned is cesium 137. The simulation results show that the Cs-137 released from the incident is moved to the west and northwest of Persian Gulf and approach the head of the Persian Gulf after fifteen days. Then driven by the discharge of the Arvandrood River to the south coast and center of the Gulf moves forward and leads to the bottom. About two months later (late August) it will leave the Strait of Hormuz and will advance the Oman Sea and the Indian Ocean. Now, if this happens on January 1, after about 30 days, cesium 137 reaches the head of the Persian Gulf, and four months later (late March) will leave the Strait of Hormuz. The results of this study can be used under the same conditions in the nuclear emergency of Bushehr Power Plant.

## 1. Introduction

Nuclear power plants are designed and built according to high standards. But the occurrence of natural disasters and the possible dangers of wars and ... can cause serious damage to them and cause the release of nuclear pollutants in the environment. The release of nuclear material in atmosphere and oceans is a major threat to the health of living creatures. Many researchers from different parts of the world, after two major Chernobyl events in Ukraine in 1986, and Fukushima in Japan in 2011 have been using numerical simulation models to try to predict the risks of releasing radioactive substances and their impact on the environment after assumptions in different nuclear power plants. So each has gained some interesting results.

After the Fukushima accident, the horizontal distribution of cesium 137 and sea surface current is simulated using several different models, like CRIEPI, JAEA, JCOPET, Sirocco, NOAA models. What the results of the models show is that coastal currents lead the pollutants to the south, after that to the east, and wherever currents become stronger, the movement of pollutants also accelerates [6]. The horizontal distribution of the sea surface concentration, in different season, obtained by a coastal model from Tokyo Electric Power Company (TEPCO), common feature for each season is the high concentration in the area close to F1NPP, which gradually decreases with distance from the F1NPP, and the relatively high-concentration plume dispersion along the shores. The contaminated water migrates eastward with the Kuroshio Extension; however, the Kuroshio Extension's position and current speed varies seasonally because of the change in the water mass balance of the Oyashio and Kuroshio currents [3].

The ROMS model shows external effective dose rate of radionuclides originated from F1NPP. In the beginning of the discharge, the external effective dose rate could peak to 10-6 Sv/hour. The effective dose originated from intake of sea food was assessed to about 1.7×10-6 Sv/year. This means immersing in the

coastal water for hours would accept the equal effective dose from intake sea food for a whole year. The effective dose rate decreased quickly and became less than 10-8 Sv/hour from May [5]. In this research, we show that if this happens for the Bushehr nuclear power plant, one of the most important and most dangerous nuclear radiculocytes, called cesium 137, with a half-life of about thirty years, extends to the Persian Gulf. This nuclear pollutant is not naturally found in the environment and only enters the environment through nuclear activities and fission of uranium 235, which can affect the surface even to the depths of the water.

## 2. Research Method

It is assumed that a major accident at Bushehr nuclear power plant, would release large amounts of radioactive nuclei into the environment, including the Cesium 137. Because of the greater importance of Cs-137, this radioactive nucleus is used in simulation. We assume the inventory of the Bushehr reactor core at the time of the incident and the percentage of that released in the environment on the basis of the Chernobyl accident [2], that is, we consider that the reactor core at the time of the incident is $1.7 \times 10^{17}$ Bq [7], of which about thirty percent is entering the environment of these, ten percent enters the water. We consider that the release of radioactive substances into the environment takes place within three days, after which time the incident is inhibited and their release into the environment is stopped. The release of the Cs-137 nucleus differs from these three days. But it is assumed, on average, that each day, $5 \times 10^{15}$ Bq (5 PBq) will enter the water from the cesium 137 [8].

The currents and physical conditions of the Persian Gulf are different for each day. For this purpose, it is necessary to consider the environmental conditions of that particular day to study the emission of nuclear pollutants. In this paper, for example, the first day of July is considered, and the average surface water flow is lowered on average for the summer, because the Shamal winds (Northwest winds) that inflate the Gulf and affect the flow of waters in the area, and water currents can reach the Gulf, so that the flow of water in the Gulf is generally more regular than in other seasons [9-10].

The development of marine and ocean emission models is needed to investigate and predict the release of nuclear materials. One of these models is the CROM code. The CROM (Código de cRiba para evaluaciÓn de iMpacto) software tool was designed by the "Information Technology Laboratory (LABI)" at the Polytechnic University of Madrid's School of Industrial Engineers in collaboration with the CIEMAT Department of Environmental Impact of Energy under the Environmental Radiation Impact Program. It is based on the SRS19, but with some improvements based on the EUR 15760. The models implemented in CROM have been published by the CIEMAT. The CROM software application is designed to automate calculation of the concentrations of radionuclides in different environments. We use here from version 8 of the CROM code , by which we examine the transfer and accumulation of Cs-137 pollutants after a hypothetical incident at the Bushehr Power Plant for the Persian Gulf on a spatial scale, and then with We use a series of simple physical calculations to make them scalable. The method of calculating the CROM model is using the exponential method and Gaussian function, which is widely used to simulate the spread of marine pollutants. The exponential function has a density function (Equation 1):

$$f(x) = \frac{1}{\lambda} e^{\frac{-1}{\lambda}x} \qquad \text{for } x \geq 0 \qquad (1)$$

Lambda (λ) is decay constant. In the exponential distribution, the user cannot truncate the distribution below it, because it does not tend to infinite to the left. The lower limit is controlled by displacing the distribution. As in the rest of the modules, certain parameters must be provided to be able to make the calculations. We find some stations in Persian Gulf and put their physical parameters in the CROM code. Export data of the code are radionuclide's concentration (C) (Equation 2) [1]:

$$C = \left(\frac{962U^{0.17}Q_i}{Dx^{1.17}}\right)\left[exp\frac{(-7.28\times10^5)U^{2.34}y_0^2}{x^{2.34}}\right]\left[exp\left(-\frac{\lambda_i x}{U}\right)\right] \qquad (2)$$

(2)

The primary data for simulating the emission of pollutants in this model is the horizontal distance between the studied stations relative to the coastline and the discharge point (x) and their vertical distance (y), the water depth at those points (D), the velocity and direction of the coastal current (U), The vertical distance of the point of discharge to the station ($y_0$) and the dispersion coefficient perpendicular to the coast ($E_y$). In addition, data on the rate of radioactive activity at discharge time (Qi) and (λi) is radioactive decay constant of pollutants are important and necessary. As a default, the initial activity of 137 cesium was calculated to be $6 \times 10^{10}$ Bq/s ($5 \times 10^{15}$ Bq/day ) [2] and we estimated the x,y,$y_0$ values for each station using the guide map. $E_y$ is various in different parts, which we used in our default software. We set the water level to about one meter (at the surface). And we set the flow rate according to Figure 9 for each station. $\lambda_i$ is $7.322 \times 10^{-10}$ /s for Cs-137.

## 3. Results and discussion

It is assumed that the incident of the Bushehr reactor took place on the first day of July 2018. Dispersion simulation of cesium 137 in the Persian Gulf indicates that due to the currents and flow of water in this basin, radionuclides tend to head to the Gulf and

very simply, given the velocity and time relation ( v = x / t ), we can estimate the time to reach the head of the Gulf and from there to the other points. It takes about 50 days to infect the whole surface of the Persian Gulf. Of course, parts from the southern shores of the United Arab Emirates and small areas in the center of the Gulf remain contaminated (Fig. 1).

On this day, surface currents reach the basin at speeds of about 0.6 m/s from the Strait of Hormuz and pass through the northern coasts (Iran) and slow down at the head of the Gulf at 0.1 m/s and then move to the south coasts. They move very slowly and enter the bed near the Strait of Hormuz. The simulation results show that after the accident, the Cs-137 is released in the west and northwest direction of the Power Plant and then begins to move toward the head of the Gulf and reaches the head of the Gulf after almost fifteen days. There , the Arvandrood crater directs it towards the center and the southern coasts, and it takes about 50 days to cover the entire gulf with regard to the speed of the surface currents, and again it is observed that the severity of pollution in the south and center of the Gulf is far less or it is even free of contaminants, and because of the direction of the surface currents in the Strait of Hormuz, it flows into the Gulf, the cesium 137 contaminates the Strait to the bed and then enters the Oman Sea and the Indian Ocean. Now, if this happens on January 1, given that the speed of the currents from the Strait of Hormuz to the Persian Gulf is about half the speed of them in the summer, and the Shamal Winds that blow from the northwest in the winter will not allow the streams to reach head of the Gulf and complete a full cycle [9]. As a result, cesium 137, as shown in Figure (2), is released at surface of the Gulf, it takes about one month to reach the head of the Persian Gulf, and from there it moves very slowly towards the south latitude. Advances to the center of the Gulf, then enters the bottom and about 4 months after that, leaves the Strait of Hormuz. Also for other radionuclides, the intensity of the radiation is similar to that in Figures 3 to 10.

To ensure the results, we compared them with some of the simulations that came from other models after the Fukushima incident. Including CRIEPI [6], JAEA [6], JCOPET [6], Sirocco [6], NOAA [6], POM [4], ROMS [5], models, and considering that the Persian Gulf is a semi-enclosed basin and that the surface water flow is more varied and more complex than the Pacific coast, so it seems to be possible to confirm the results of the CROM model to a high degree.

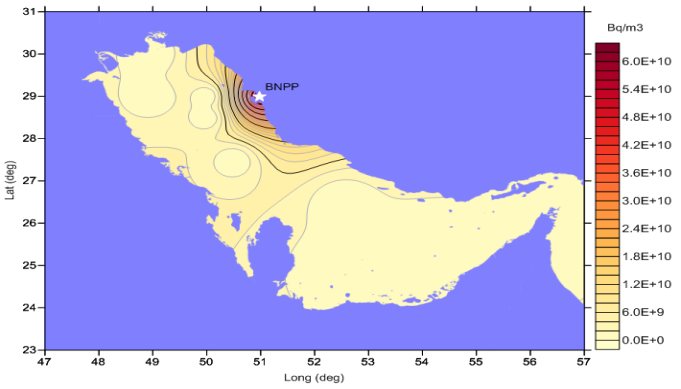


**Fig 1. Dispersion Cs-137 in the Persian Gulf (summer)**

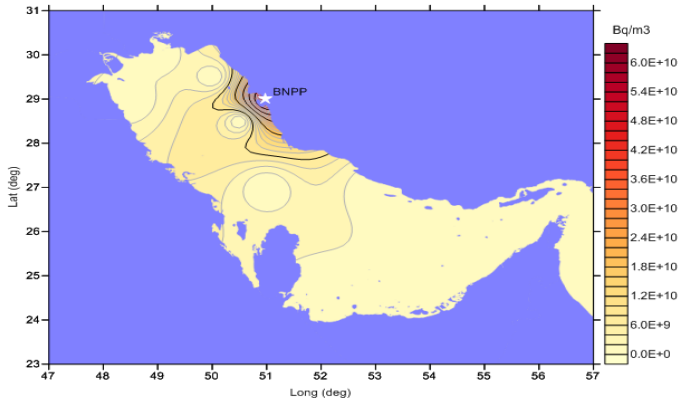


**Fig 2. Dispersion Cs-137 in the Persian Gulf (winter)**

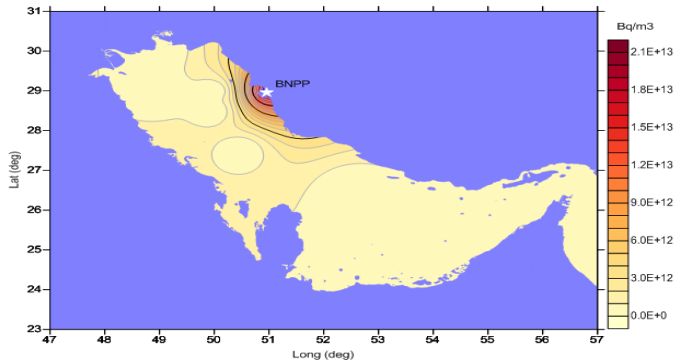


**Fig 3. Dispersion I-131 in the Persian Gulf (summer)**

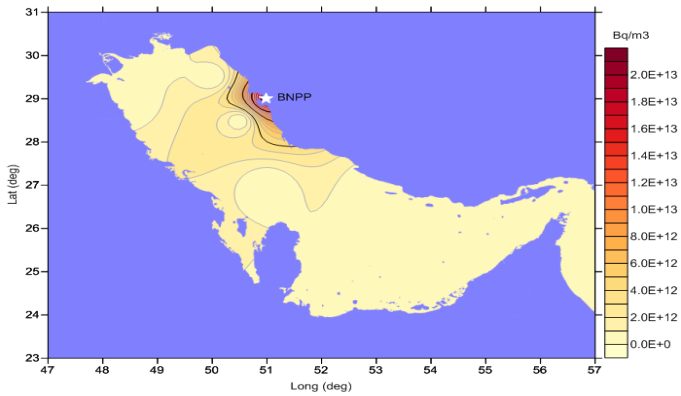


**Fig 4. Dispersion I-131 in the Persian Gulf (winter)**

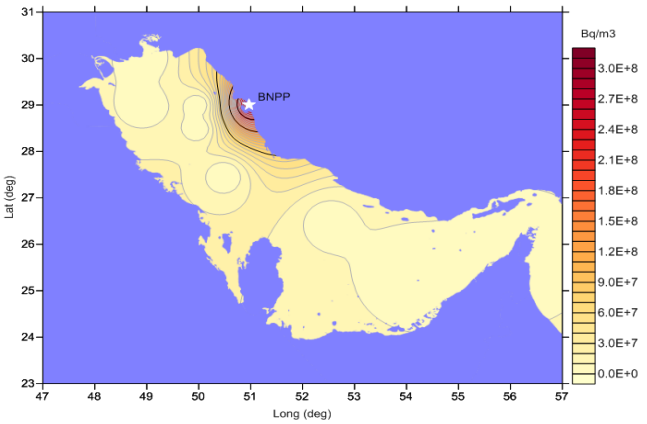


**Fig 5. Dispersion Pu-239 in the Persian Gulf (summer)**

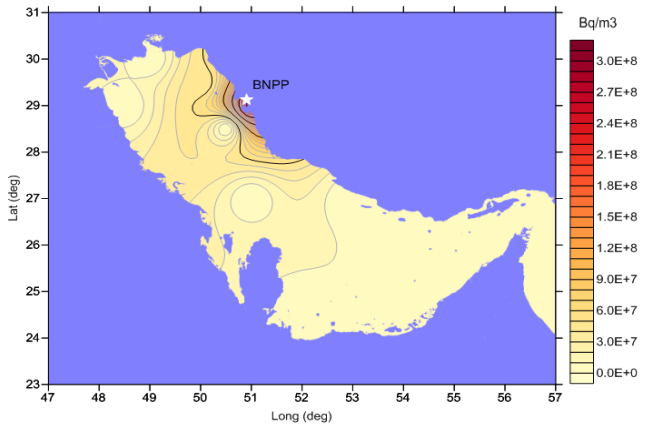


**Fig 6. Dispersion Pu-239 in the Persian Gulf (winter)**

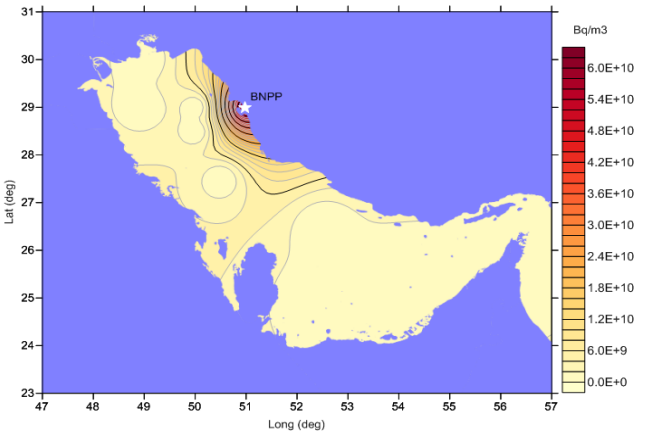


**Fig 7. Dispersion Sr-90 in the Persian Gulf (summer)**

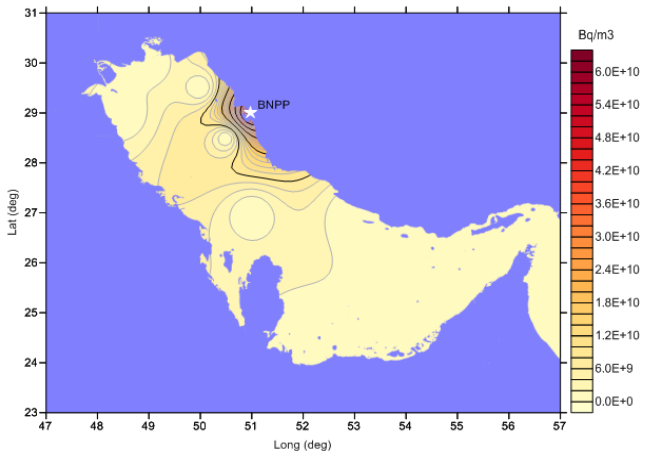


**Fig 8. Dispersion Sr-90 in the Persian Gulf (winter)**

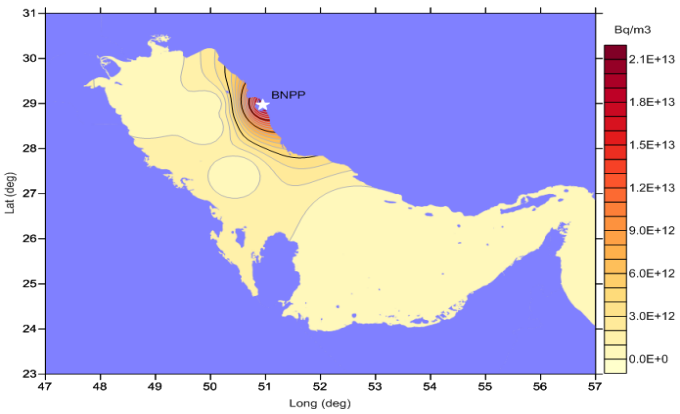


**Fig 9. Dispersion Te-132 in the Persian Gulf (summer)**

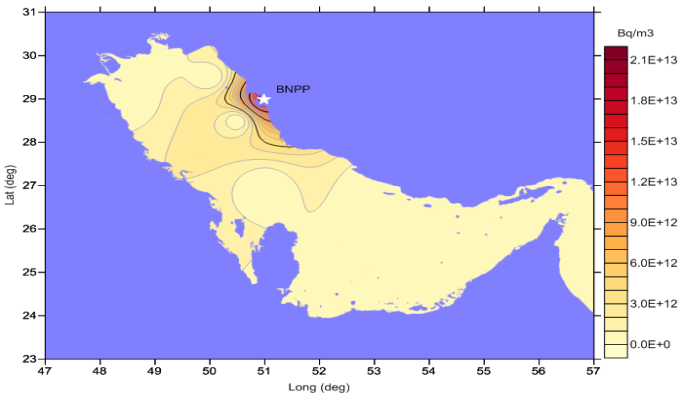


**Fig 10. Dispersion Te-132 in the Persian Gulf (winter)**

## 4. Conclusion

In this paper, a simulation of the dispersion and concentration of the Cesium 137 nuclear fugitive released from the incident of Bushehr Power Plant was studied using the CROM model on July 1, 2018.And surface water currents are assumed to be on average for the summer season Because the northwest winds (Shamal winds) that affect the bay and circulate the waters of this area are minimized and water flows can reach the Gulf, so that the flow of water in the Gulf is generally more regular than other seasons. The simulation results show when the Persian Gulf currents are similar to those in this paper, Cesium 137 released from the incident goes further towards the Gulf and the maximum polluting deposition is on the same northern coast and near the Bushehr province. It then advances towards the west and northwest, so that it reaches the head of the Persian Gulf after fifteen days, and is driven by the discharge of the Arvandrood river crater to the south coast and center of the Gulf, and from there, it is directed to the bottom. About two months later (late August), it will leave the Strait of Hormuz and will advance the Oman Sea and the Indian Ocean. If we choose the first of July, the first of January, winter season, for the incident, then the flows from the Strait of Hormuz are about half that in the summer. Also, due to the "Shamal" winds that flow northwest to the Persian Gulf, currents can not reach the Gulf and complete the entire cycle through the Gulf, which is very important in the release of nuclear pollutants.So that, after about

30 days, cesium 137 reaches the top of the Gulf, and four months later (late March) will leave the strait of Hormuz. Of course, given the 30-year-old half-life of 137 cesium, and that the Gulf is a closed water basin, and it takes about 3 to 5 years to change its water, we expect the cesium-137, a alkali metal, to be polluting for many years Deep in the Gulf, in particular, remain litter.

The strontium 90, which lies in the group of alkaline earth metals and has a half-life of about 28 years, has the same behavior as cesium.

Plutonium 239, from actinides (intermediate metals), due to its high density and half-life, moves more sophisticated than the rest of the pollutants in both seasons, and can not reach the summit of the Gulf in the summer and is strongly influenced by Arvandrood to the central and It is part of the Southwest coast; it has a large part of the southern coast. Before reaching the eastern half of the Gulf, it enters the bed due to heavy load, and is located in sediments. In winter, it can overcome the discharge of the Arvandrood river and have a short stay in the Gulf. And although he goes a little toward the west, he is still guided to the southwestern coast and goes from there to bed.

Iodine 131 and Tellurium 132 are both non-metallic and exactly interact with each other. In the summer, they move in a counterclockwise direction to the southwestern coast, but they are driven straight into the winter and enter the bed.

All of the nuclear pollutants are drifting more toward the southwestern coast in the winter. While in the summer they tend to reach the northwest. So, in the summer, they will have a more complete cycle of cycling. But in the winter they are direct from the coast of Bushehr to the southwest coast and then slowly enter the bed.

## 5. References

1- International Atomic Energy Agency, *Generic models for use in assessing the impact of discharges of radioactive substances to the environment*, Safety Reports Series, Vienna 2001.

2- Kaviyani, F., Memariyan, M. H., Eslami Kalantari, M., (2017), *Simulation of transmission air pollution and deposition of abandoned nuclear pollutants from a predictable incident at Bushehr Power Plant*, Phys. Earth and Space, Vol. 43, p. 650-635.

3- Kobayashi, T., In, T., Ishikawa, Y., (2015), *Development of ocean dispersion concentration maps of the contaminated water released from the Fukushima Dai-ichi Nuclear Power Plant*, Nucl. Sci. Technol. Vol. 52, p. 769–772.

4- Kobayashi, T., Otosaka, S., Togawa, O., Hayashi, K., (2007), *Development of a non-conservative radionuclides dispersion model in the ocean and its application to surface Cesium-137 dispersion in the Irish Sea*, Nucl. Sci. Technol. Vol. 44, p. 238–247.

5- Guan, Y., Shen, S., Huang, H., (2015), *Numerical simulation of dispersion of radionuclides released from the Fukushima NPP and the assessment of their nuclear impact*, Appl. Mech. Mat., Vol. 737, p. 417-421.

6- Masumoto, Y., Miyazawa, Y., Tsumune, D., Tsubono, T., Kobayashi, T., Kawamura, H., Estournel, C., Marsaleix, P., Lanerolle, L., Mehra, A., Garraffo, Z. D., (2012), *Oceanic dispersion simulations of Cs-137 released from the Fukushima Daiichi Nuclear Power Plant*, Elements, Vol. 8, p. 207–212.

7- Ramzaev, V., Nikitin, A., Sevastyanov, A., Artemiev, G., Bruk, G., Ivanov**,** S., (2014), *Shipboard determination of radiocesium in seawater after the Fukushima accident: results from the 2011–2012 Russian expeditions to the Sea of Japan and western North Pacific Ocean*, Environ. Radioact, Vol. 135, p. 13-24.

8- John, E., Hoeve, T., Jacobson, M. Z., (2012), *Worldwide health effects of the Fukushima Daiichi nuclear accident*, Energ. Environ. Sci. Vol. 5, p. 8743-8757.

9- Yao, F., (2008), *Water mass formation and circulation in the Persian Gulf and water exchange with the Indian Ocean, Submitted to the Faculty of the University of Miami in partial fulfillment of the requirements for the degree of Doctor of Philosophy*, Coral Gables, Florida, Vol. 144.

10- Stephane, P., Pascal, L., Xavier, C., (2015), *A model of the general circulation in the Persian Gulf and in the Strait of Hormuz: Intra seasonal to inter annual variability*, Cont. Shelf Res. Vol. 94, p. 55-70.

INTERNATIONAL JOURNAL OF
COASTAL & OFFSHORE ENGINEERING
IJCOE Vol.3/No. 3/Autumn 2018 (19-27)

Available online at: http://ijcoe.org/browse.php?a_code=A-10-233-2&sid=1&slc_lang=en

# Experimental Study of Wave Spectrum Type Impact on Inner Chamber Fluctuation, Pressure and Reflection of OWC Device

**Milad Zabihi[1], Said Mazaheri[2*], Masoud Montazeri Namin[3]**

[1] *Ph.D student, Iranian National Institute for Oceanography and Atmospheric Science; milad.zabihi@inio.ac.ir*
[2*] *A/Professor, Iranian National Institute for Oceanography and Atmospheric Science; said.mazaheri@inio.ac.ir*
[3] *Assistant Professor, University of Tehran; mnamin@ut.ac.ir*

**ARTICLE INFO**

*Article History:*
Received: 18 Oct. 2018
Accepted: 16 Dec. 2018

*Keywords:*
OWC
Wave Spectrum
Reflection
Experimental

**ABSTRACT**

Increasing problems due to supplying energy demand conveyed researchers to find a solution in renewable energy resources and consequently marine engineers drew attentions towards wave energy which has the merit of higher energy density than the other resources. Oscillating Water Column (OWC) is one of the most propitious devices for capturing wave energy. Researchers have studied the device under different wave height and period conditions and they investigated various geometric parameters such as front wall draft and the chamber length. However, the effects of wave spectrum type or shape has not been investigated deeply yet. Different wave spectra have been developed for different places around the world but the focus of this study is on the two well-known spectra called JONSWAP and Pierson-Moskowitz to see how the type of the spectrum can impact on inner chamber fluctuation, pressure variation and reflection response of an offshore OWC. To achieve this goal, a 1:15 scale model of an offshore OWC was constructed in National Iranian Marine Laboratory. The results show that inner chamber free surface spectrum is affected by the type of incident wave spectrum. In another word, energy content at peak frequency was approximately 50% higher when the incident wave spectrum is of JONSWAP type. However, energy corresponding to sloshing frequency and total energy content in the chamber were almost the same for both types of the spectra. Pressure spectra inside the chamber showed a similar trend as free surface elevation. Although there was a little difference in reflection response of an OWC influenced by the type of spectra, this discrepancy was more pronounced in high frequency waves.

## 1. Introduction

Undoubtedly, environmental impacts of using fossil energy resources such as global warming and its consequent outcomes are a menace for the earth future. This was a motivation for researchers to put much more effort in harnessing renewable energy resources in recent years. Among new sustainable approaches of generating energy, one that particularly stands out is marine renewable energy. Marine renewable energy can be classified as offshore wind, thermal, tidal and wave power. Wave farm higher energy density (2-3) kw/m$^2$ rather than solar (0.1-0.2) kw/m$^2$ and wind farms (0.4-0.6) kw/m$^2$ is its advantage over other marine renewable energy resources [1]. Of all different technologies developed for wave energy conversion, Oscillating Water Columns (OWC) seems to be the most propitious device even reached to full scale prototype [2]. OWCs are recognized by their common rectangular compartment which are partially submerged. The structure is open to sea at the bottom allowing the incoming waves to be transferred in to the structure. Subsequently, wave induced fluctuation inside the chamber or compartment causes the trapped air to drive the turbine which is built in at the top of the chamber. Then using a generator, turbine movement can be converted to electricity.

Research on offshore located OWCs are much more limited rather than those which are positioned at shore or nearshore. Although offshore OWCs may suffer from higher funding for development, they are exposed to higher amount of energy rather than onshore ones. They can be integrated with floating breakwaters to reduce the construction cost and can be a good choice for the small islands or offshore construction sites to help them supply their needed energy [3]. An offshore OWC was developed by Masuda for the first time [4].

Lots of studies can be found in the context of OWCs including numerical and experimental approaches. Evans [5] was a pioneer researcher who introduced rigid piston model for free surface fluctuation inside the chamber. His model was developed by [6-9]. They tried to consider free surface crookedness through applying a periodic pressure distributed over the surface. Later, researchers who were involved with numerical procedure used boundary element methods [10-11] or utilized CFD capabilities to solve fully nonlinear interaction in the chamber based on Navier-Stokes equation [12-16]. The latter approach has the merit of taking nonlinear interactions into account; such as wave breaking and sloshing.

Apart from the aforementioned numerical investigations, valuable experimental studies can be found in the literature. Some of them focused on shore-based OWCs such as those studies conducted by Morris-Thomas et al. [17] and Vyzikas et al. [18] who worked on shape of the front wall and OWC geometry, respectively. Viviano et al. [19] built a 1:5-1:9 scale model and evaluated wave loading and wave reflection for irregular wave impingement. Ning et al. [20] did an experimental research on shore based OWCs and studied free surface oscillation in the chamber.

Contrary to shore-based experimental studies, research on detached floating or fixed OWCs are relatively limited. Sheng et al. [21] carried out experiments on floating cylindrical shaped OWCs and found that the ratio of orifice area to water column area plays an important role and a value of 1.7% to 2.28% leads to optimum efficiency for the device. Crema et al. [22], also did an experimental research on an OWC joining a floating structure, namely a breakwater. They evaluated geometric parameters and wave condition to determine OWC performance. Very recently, Elhanafi et al. [23-25] carried out experimental tests and used their data to validate their numerical model for further analyze on OWC performance. The 1:50 scale model of offshore stationary model was constructed and its performance was evaluated against regular wave attack.

Despite all researchers' efforts, the industry needs much more confidence to invest on these devices and this issue necessitates more investigation on the OWC performance to bridge the gap between commercializing and research. Moreover, reviewing the literature shows that firstly, experimental tests on offshore OWCs are much less despite the fact that offshore OWCs are exposed to higher wave energy. Secondly, to the best knowledge of the authors there is no similar study addressing wave spectrum type impacts on OWC performance. Different spectrum types are developed for different marine environments; however, the two most familiar ones, that is to say JONSWAP and Pierson-Moskowitz (hereafter called P-M) are evaluated here. It is worth mentioning that evaluation of the device efficiency influenced by spectrum type is presented by the authors in a separated paper [26]. Hence, the aim of this paper is only to investigate the free surface fluctuation and pressure variation inside the chamber affected by spectrum type. In addition, in this paper, reflection from OWC device is studied under the impact of wave spectrum type.

Regardless of OWC device geometry, wave-OWC nonlinear interactions such as sloshing and wave reflection have impacts on both OWC hydrodynamic performance and structural design. Concerning hydrodynamic interactions, which is the focus of this paper, it should be mentioned that the less sloshing occurs, the more energy can be extracted. This is due to low pressure variation at sloshing frequencies. Moreover, reflection is highly affected by the OWC device geometry and the ratio of water depth to wave length. The latter parameter is examined in this study.

The rest of the paper can be summarized as follows; section 2 is dedicated to a brief explanation of experiments where the reader can find the test conditions. Section 3 presents the results of chamber free surface fluctuation, pressure variation and reflection affected by spectrum type. Section 4 which is the last section of this paper presents concluding remarks.

## 2. Experimental Tests

Experiments were done at National Iranian Marine Laboratory (NIMALA), Tehran, Iran. Actually, the Laboratory is a large towing tank with 400 m length, 6 m width and 4 m depth. It is possible to set the wave maker to generate regular or irregular waves. Wave height in irregular wave generation is limited to 40 cm and wave peak period is limited to 3s. However, instruction given by the laboratory technicians restricted the wave height and wave period to 30 cm and 2.5 s, respectively. Such a restriction was due to the fact that wave may flow out of tank end wall for extremely long waves. It should be mentioned that a sloped beach is constructed at far end of the tank to prevent coming back of transmitted waves. To control the wave induced movements of the OWC model and to make it fix in its location, a huge steel frame was built. Cables were also used to ensure no movement occurs. The steel frame is shown in Figure 1.

A 1:15 scale model of an OWC which was built using plexiglass is shown in Figure 2. Dimensions of the physical model are specified in Figure 2. Slot shape opening in the OWC roof was to take damping effect in to account. As applied by [3] and [18], there are several ways to consider Power Take Off effect including slot shape opening and orifice one. Slot shape approach was used in this paper. In these test series evaluating spectrum type impact, slot size was kept constant during the test at 1 cm which is equivalent to aperture ratio of 1.28%. It is worth mentioning that aperture ratio is defined as the ratio of slot size to the net chamber length (0.78m). Instrumentation along the

tank and inside the chamber is shown in Figure 3 and Figure 4 . As can be seen three Wave Gauges (WG) were used outside the OWC to separate incident and reflected waves. Two also were used inside the chamber for tracking free surface fluctuation. Pressure Sensors (PS) were also utilized to measure the pressure variation inside the chamber. Measurement frequency was 50 hz for all instruments. A data acquisition system was used to convert the voltage outputs of the WGs and PS to readable surface elevation and pressure data according to centimeter and pascal units, respectively (Figure 5).

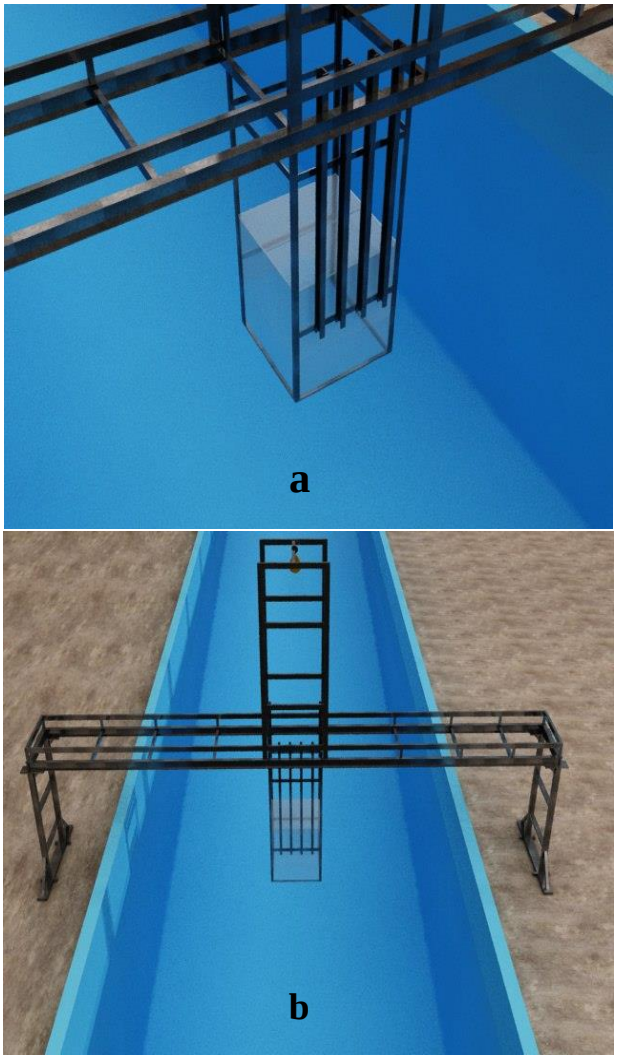


**Figure 1. 3D view of holding frame for keeping OWC in its position, (a): back view of OWC (using U section beams at the back of the OWC structure, (b); Front view**


**Figure 2. Dimension of the physical model (meter)**

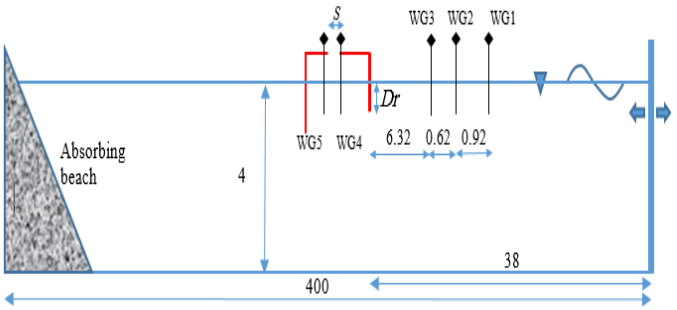


**Figure 3. Location of the wave gauges and pressure sensors, in meter (Not to scale) [26]**

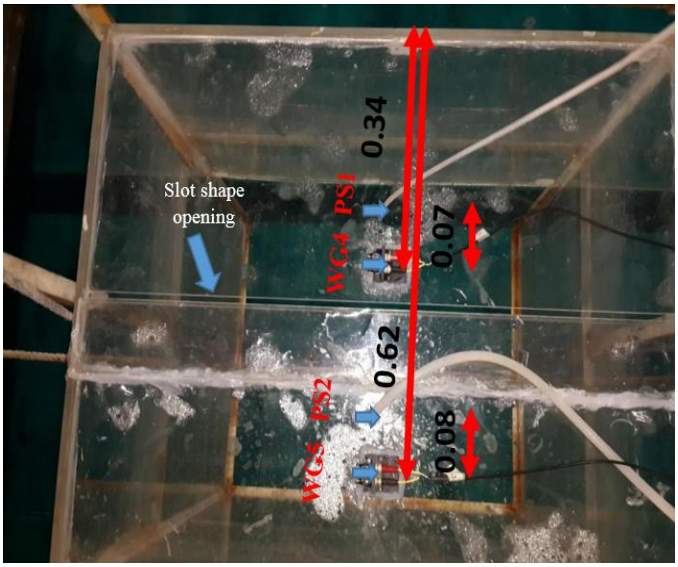


**Figure 4. Top view of the OWC chamber, PS and WGs location, in meter**

**Figure 5. Data acquisition system**

JONSWAP and P-M spectra were used in this paper. The following equations account for JONSWAP and P-M spectra.

$$S(f) = \frac{\alpha g^2}{f^5}\exp[\frac{-5}{4}(\frac{f_p}{f})^4]\gamma^r \quad (1)$$

where

$$r = \exp[-\frac{(f-f_p)^2}{2\sigma^2 f_p^2}] \quad (2)$$

$$\alpha \approx \frac{0.0624}{0.230 + 0.0336\gamma - (0.185/(1.9+\gamma))} \quad (3)$$

and $\sigma \approx 0.07$ if $f \le f_p$, and $\sigma \approx 0.09$ if $f > f_p$.

$\gamma$ is known as shape factor which is considered to be 3.3 and 1 for JONSWAP and P-M spectra, respectively. The wave condition applied in this paper are mentioned in Table 1. Three test series including six tests were performed here. To isolate wave spectrum type effect, wave height and period was kept constant during each series. Moreover, wave steepness defined as $H_{m0}/L_p$ was kept constant during the test at 0.026. It is notable that water depth was 4m in all tests.

**Table 1. Tests Condition**

| | Incident Wave Characteristics | | | OWC Geometry | |
|---|---|---|---|---|---|
| Test no. | Spectrum Type | Wave Height ($H_{m0}$) [cm] | *kd* | Slot size[cm] | Front wall Draft [cm] |
| 1 | JONSWAP | 10 | 6.45 | 1 | 20 |
| 2 | P-M | 10 | 6.45 | 1 | 20 |
| 3 | JONSWAP | 15 | 4.28 | 1 | 20 |
| 4 | P-M | 15 | 4.28 | 1 | 20 |
| 5 | JONSWAP | 25 | 2.60 | 1 | 20 |
| 6 | P-M | 25 | 2.60 | 1 | 20 |

## 3. Results and Discussion

### 3.1. Spectrum Type Impact on Free Surface Fluctuation inside the Chamber

Previously, it was found by the authors that for shorter period waves (*kd*=6.45 and 4.28), efficiency of the device is higher when the incident wave spectrum is of JONSWAP type while for longer wavelengths (*kd*=2.6) P-M spectrum causes more energy capture. This was attributed to the wider distribution of the inner chamber spectrum caused by incident P-M spectrum at *kd*=2.6 [26]. The aforementioned results are not repeated in this paper for abridgement. As an extension to the previous paper [26], this paper studies the effect of spectrum type on inner chamber free surface fluctuation with the focus on sloshing in the chamber. According to [27], sloshing may occur in closed chambers. When sloshing happens, the pressure variation in the chamber would be nearly zero and thus no energy could be extracted by the device. Hence, it is of great importance to be evaluated in designing procedure. Given *B* as chamber length, sloshing can be observed at different modes according to $kB = n\pi$. Replacing *B* by 0.78 (net length of the OWC camber) it is likely to see first mode at 1 hz and second mode at 1.4 hz in this study.

Figure 6 to Figure 8 show spectrum density calculated for WG5 influenced by wave spectrum type. As it is clear, in all Figures, the inner chamber spectra are influenced by the incident wave type. In fact, when the incident wave type is of JONSWAP type, greater values of energy content was observed at incident wave peak frequency. For example, in Figure 6, peak energy content in the chamber corresponding to JONSWAP type spectrum is approximately 50% more than the energy content calculated for P-M spectrum. For the rest of the domain frequencies, P-M spectrum may yields higher energy content; especially at *kd*=2.6 for $0.5 < f < 0.7$.

However, spectral analysis shows that total energy content in the system due to water fluctuation is the same for the two spectra which have been applied. Table 2 shows the result of spectrum analysis for both spectra. As can be seen, there is negligible difference between wave heights values calculated in the chamber showing that the amount of energy content inside the chamber caused by water fluctuation is almost equal for both spectra.

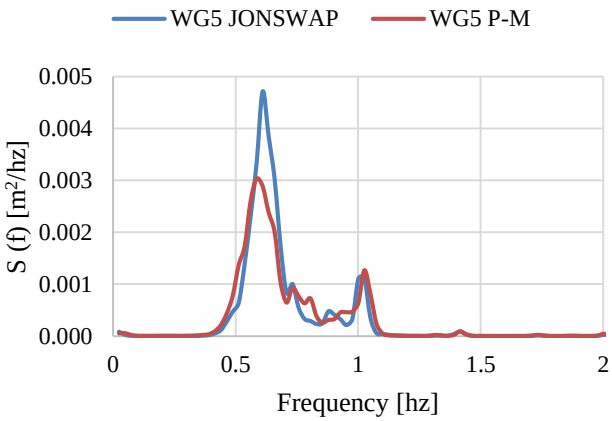


**Figure 6. Spectrum of WG5 under the impact of JONSWAP and P-M spectra as incident waves, $H_{m0}$=10 cm *kd*=6.45**

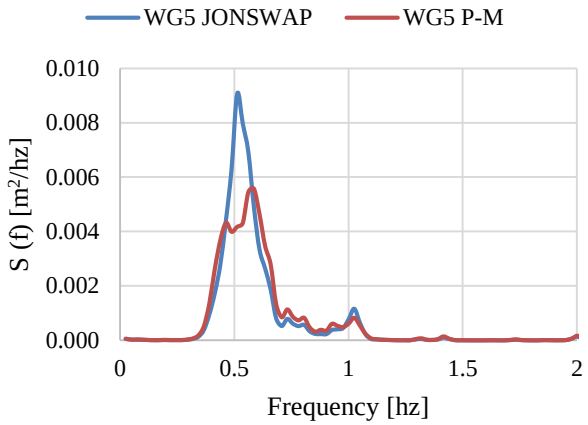


**Figure 7. Spectrum of WG5 under the impact of JONSWAP and P-M spectra as incident waves, $H_{m0}$=15 cm *kd*=4.28**

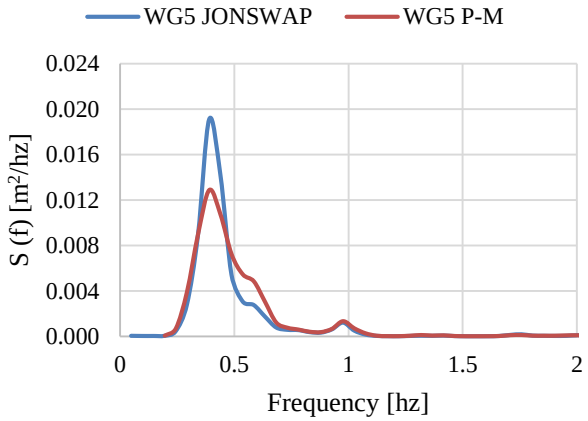


**Figure 8. Spectrum of WG5 under the impact of JONSWAP and P-M spectra as incident waves, $H_{m0}$=25 cm *kd*=2.60**

**Table 2. Spectral analysis for the conducted tests, results of WG5**

| Incident Wave Characteristics | | | | Inner Chamber Spectral Analysis |
|---|---|---|---|---|
| Test no. | Spectrum Type | Incident Wave Height ($H_{m0}$) [cm] | *kd* | Inner Wave Height ($H_{m0}$) [cm] |
| 1 | JONSWAP | 10 | 6.45 | 10.89 |
| 2 | P-M | 10 | 6.45 | 10.57 |
| 3 | JONSWAP | 15 | 4.28 | 15.79 |
| 4 | P-M | 15 | 4.28 | 15.29 |
| 5 | JONSWAP | 25 | 2.6 | 22.51 |
| 6 | P-M | 25 | 2.6 | 22.59 |

Another important point is energy content related to higher frequencies. Although the energy content for higher frequencies are much less than energy content corresponding to peak frequency, it is of great importance as it is associated with sloshing energy content. It should be mentioned that sloshing has destructive effects both on structural strength and device energy conversion efficiency.

It is clearly visible that sloshing energy content occurs at all the cases which have been tested but it is more pronounced at incident waves with higher peak frequency because the ratio of sloshing energy to total energy inside the chamber is higher for short period waves. On the other hand, there is no significant difference in sloshing energy for the two spectra, as regardless of the spectrum type, the tests showed almost equal sloshing energy. This trend was seen in all the tests.

For a better understanding of sloshing contribution on free surface fluctuation inside the chamber, sloshing frequency is filtered and plotted during the test. The results of total free surface fluctuation inside the chamber are presented beside the sloshing-only surface elevation for a better comparison. Figure 9 shows the case when the incident wave is of JONSWAP type and Figure 10 is related to the case of P-M spectrum as incident wave. As it is clear, the maximum amount of sloshing fluctuation is the same for both spectra and it is around 4 cm.

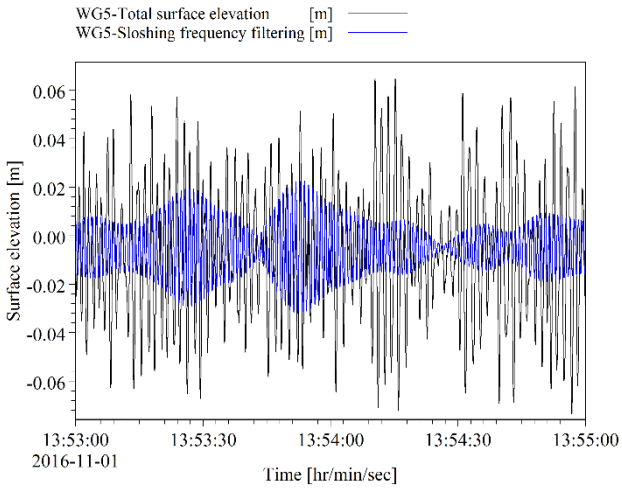


**Figure 9. Comparing surface fluctuation due to sloshing and total free surface fluctuation measured at WG5 for incident wave of JONSWAP type; Test no.1**

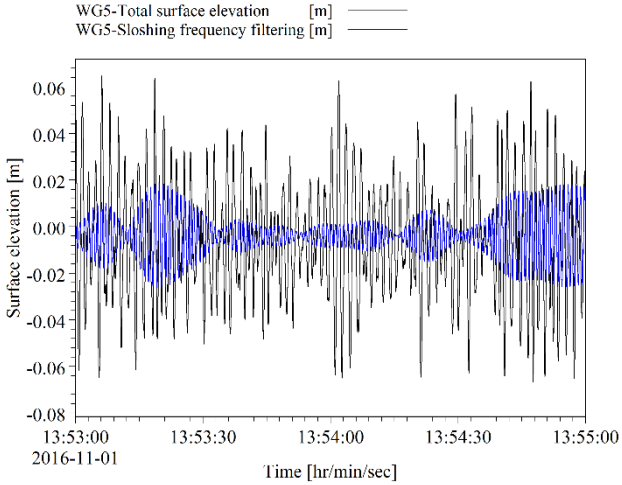


**Figure 10. Comparing surface fluctuation due to sloshing and total free surface fluctuation measured at WG5 for incident wave of P-M type; Test no.2**

### 3.2. Spectrum Type Impact on Chamber Pressure Variation

Apart from the fact that longer incident periods caused higher pressure values, the focus of this part was on chamber pressure variation due to spectrum type for the same wave condition. The results show that air pressure inside the OWC is completely affected by the incident spectrum type. Figure 11 to 13 shows pressure spectra inside the chamber. The shape of the obtained spectra are influenced by the shape of the incident wave spectrum. In other words, JONSWAP spectrum caused higher pressure in peak frequency but this was not the case for $f>fp$. In fact for frequencies other than peak frequency, the pressure spectra were overlapped.

It is worth mentioning that according Figure 11 to 13 pressure values corresponding to $f$=1 hz (sloshing frequency) is almost zero.

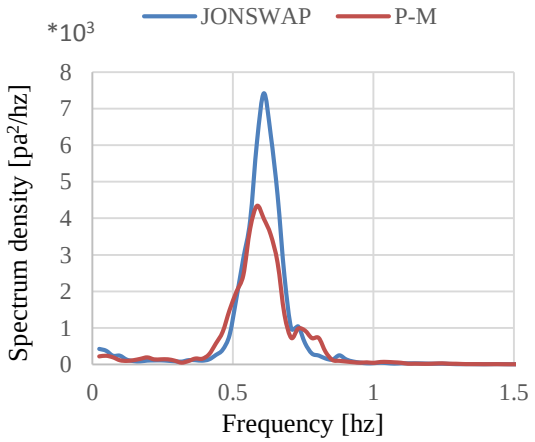


**Figure 11. Pressure spectrum inside the chamber, under the impact of JONSWAP and P-M spectra as incident waves, $H_{m0}$=10 cm $kd$=6.45**

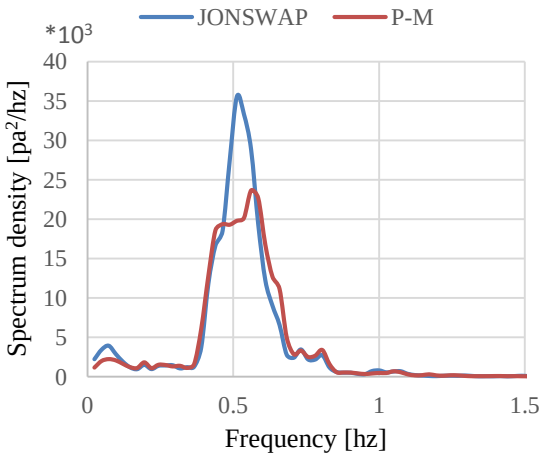


**Figure 12. Pressure spectrum inside the chamber, under the impact of JONSWAP and P-M spectra as incident waves, $H_{m0}$=15 cm $kd$=4.28**

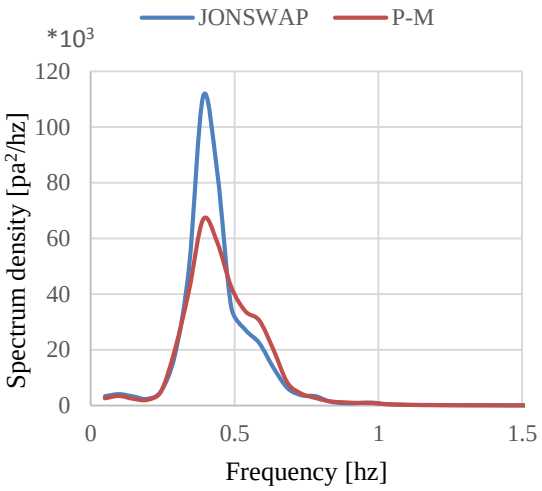


**Figure 13. Pressure spectrum inside the chamber, under the impact of JONSWAP and P-M spectra as incident waves, $H_{m0}$=25 cm $kd$=2.60**

### 3.3. Spectrum Impact on Reflection by OWC

Detailed information on separating incident and reflected waves can be found in Ref [28]; however, a brief explanation of this procedure is provided in the following paragraph. Wave surface elevation can be decomposed to linear incident and reflected wave components. In its complex form it is given as;

$$\eta = \sum_{n=-N}^{N} [a_{In} e^{i(\omega_n t - k_n x)} + a_{Rn} e^{i(\omega_n t + k_n x)}] \quad , for\ n \neq 0 \tag{4}$$

where $a_{In}$ and $a_{Rn}$ are complex parameters representing incident and reflected components, respectively. Their absolute values show the amplitude. $t$ is time, $x$ is wave propagation direction, subscript $n$ shows $n$th harmonic component, $\omega_n$ is angular frequency defined as $\omega_n = \frac{2\pi n}{t_{end}}$ where in the aforementioned relation $t_{end}$ represents the total test duration; $k_n$ is wave number.

Applying Fourier transformation on each probe (assume it as $m$) data, it can be written as a function of a complex parameter $F_{n,m}$.

$$\eta_m = \sum_{n=-N}^{N} F_{n,m}\, e^{i\omega_n} \tag{5}$$

From Eq. (4), the following relation is acquired;

$$F_{n,m} = a_{In} e^{-ik_n x_m} + a_{Rn} e^{ik_n x_m} \tag{6}$$

where $x_m$ shows the location of the probe $m$. This procedure can be repeated for each of the probes. If 3 probes were used, the method of Mansard and Funke

[29] based on least square method could be used to solve the unknowns.

As mentioned before absolute values of $a_{In}$ and $a_{Rn}$ are equal to incident and reflected wave amplitude for the *n*th harmonic, respectively. Hence, reflection function *Cr*(f) for each wave frequency component can be calculated as;

$$C_r(f) = \frac{|a_{Rn}|}{|a_{In}|} \quad (7)$$

and total wave reflection coefficient is given by Eq. (8);

$$C_r = \sqrt{\sum_{n=n_1}^{n_2} |a_{R_n}|^2 \Big/ \sum_{n=n_1}^{n_2} |a_{I_n}|^2} \quad (8)$$

where $n_1$ and $n_2$ are lower and upper bounds of the spectral range within that reflection value is calculated. Figure 14 shows reflection coefficients for each test. As it is obvious, reflection increases with the increase of *kd* for both types of spectra. This can be attributed to the larger ratios of wave length to chamber length for low frequency waves which causes the wave to be transmitted more rather than to be reflected. Therefore, low frequency waves yield lower reflection coefficients than high frequency waves in offshore OWCs.

There is negligible difference in reflection due to wave spectrum type. For example, at *kd* =2.6 reflection by OWC in the case of JONSWAP spectrum is around 0.18 while for P-M spectrum it is approximately 0.19. Generally, reflection coefficient is lower when the incident wave is of JONSWAP spectrum. This issue is more pronounced at high frequency waves; i.e. *kd*=6.45.

For a better understanding of reflection response of an OWC influenced by the type of incident wave spectrum, the spectral reflection coefficient for *kd*=6.45 (caused biggest difference in reflection response) is plotted versus the ratio of chamber length to wave length for each frequency component (See Figure 15). As can be seen, some differences between the two spectra occurred at *B/L*=0.05 to 0.07, 0.36 to 0.5 and 0.8 to 0.96 but the general trend is similar. This figure shows that regardless of the spectrum type all reflection coefficients for *B/L*=0.1 to 0.36 are almost zero. Outside this range for greater *B/L*, spectral reflection values were greater than 1. This behavior can be attributed to energy transfer between wave frequencies. Wave energy conversion in an OWC system highly depends on water and air motion. Since irregular waves are intrinsically variable in time domain, their interaction with OWC influence on air intake and outflow. When incident wave is not in phase with air flow inside the chamber, its pressure instantly adjusts while air frequency may need to a longer time for being adjusted. Consequently, those wave frequencies which are in phase with air flow (they are close to peak frequencies) would be transformed to pneumatic energy and those which are not in phase with air motion can't enter into the chamber. The latter wave frequencies are those frequencies which their reflection amplitude is greater than their incident amplitude; yielding spectral reflection values *Cr(f)* >1 [19].

It is worth mentioning that *Cr* values calculated by Eq. (8) always lead to a value lower than 1, because it considers the ratio between the incident and reflected energy based on conservation of energy [28]. On the other hand as spectral components characterized by *Cr(f)*>1 are small they have little impact on *Cr* calculated by Eq. (8) [28].

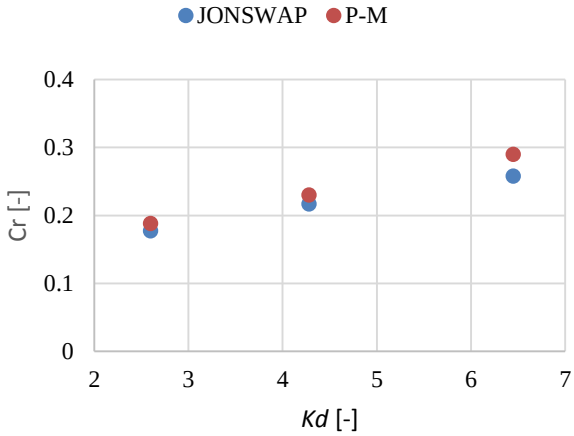


**Figure 14. Reflection coefficient *Cr* versus *kd* for JONSWAP and P-M spectra**

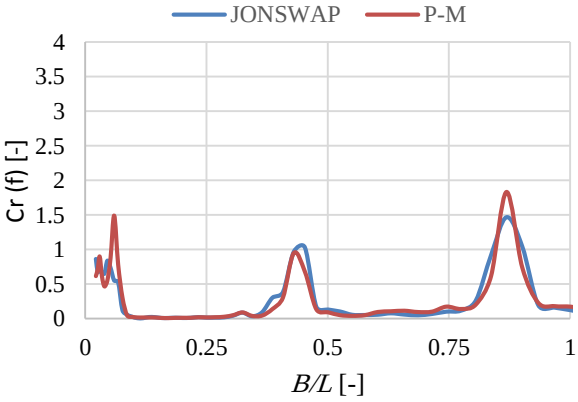


**Figure 15. Spectral reflection versus *B/L* for each frequency component, *kd*=6.45**

## 4. Summary and Conclusions

OWC is one of the wave energy devices which is widely studied by the researchers in the last years. However, experimental studies focusing on offshore OWCs are relatively limited. On the other hand, the previous researchers put their concentration on evaluating wave condition and chamber geometry effects in OWC efficiency. This paper addressed the wave spectrum type impacts on free surface fluctuation inside the chamber, pressure variation and reflection by OWC using a 1:15 physical scale model. The concluding remarks can be summarized as follows;

- Inner chamber free surface spectrum is affected by the type of incident wave spectrum. In another word, energy content at peak frequency was approximately 50% higher when the incident wave spectrum is of JONSWAP type. However, energy content corresponding to sloshing frequency and total energy content in the chamber were almost the same for both types of the spectra.
- JONSWAP spectrum caused higher pressure in peak frequency but this was not the case for *f>fp*. In fact for frequencies other than peak frequency, the pressure spectra of different types (JONSWAP and P-M) were overlapped.
- Reflection coefficient increased by increase of *kd* for both types of spectra.
- There was a little difference in reflection response of an OWC influenced by the type of spectra; however, this discrepancy was more pronounced in high frequency waves.
- For *kd*=6.45 both types of spectra applied as incident waves, showed somehow similar trend in spectral reflection.
- Regardless of the spectrum type all spectral reflection coefficients for *B/L*=0.1 to 0.36 are almost zero.

## 6. References


1- N. Khan, A. Kalair, N. Abas, and A. Haider, "Review of ocean tidal, wave and thermal energy technologies," *Renewable and Sustainable Energy Reviews*, vol. 72. pp. 590–604, 2017.

2- I. López, J. Andreu, S. Ceballos, I. Martínez de Alegría, and I. Kortabarria, "Review of wave energy technologies and the necessary power-equipment," *Renew. Sustain. Energy Rev.*, vol. 27, pp. 413–434, Nov. 2013.

3- F. He, J. Leng, and X. Zhao, "An experimental investigation into the wave power extraction of a floating box-type breakwater with dual pneumatic chambers," *Appl. Ocean Res.*, vol. 67, pp. 21–30, 2017.

4- A. F. O. Falcão and J. C. C. Henriques, "Model-prototype similarity of oscillating-water-column wave energy converters," *Int. J. Mar. Energy*, vol. 6, pp. 18–34, 2014.

5- D. V Evans, "The oscillating water column wave energy device," *J. Inst. Maths Applics*, vol. 22, pp. 423–433, 1978.

6- A. F. de O. Falcão and A. Sarmento, "Wave generation by a periodic surface pressure and its application in wave-energy extraction," in *15th international congress of theoritical and applied mechanics*, 1980.

7- J. Falnes and P. McIver, "Surface wave interactions with systems of oscillating bodies and pressure distributions," *Appl. Ocean Res.*, vol. 7, no. 4, pp. 225–234, 1985.

8- A. J. N. A. Sarmento and A. F. O. De Falcao, "Wave generation by an oscillating surface-pressure and its applications in wave energy extraction," *J. Fluid Mech.*, vol. 150, pp. 467–485, 1985.

9- D. . Evans, "Wave power absorption by systems of oscillating surface pressure distributions," *J. Fluid Mech.*, vol. 114, pp. 481–499, 1982.

10- A. Brito-Melo, A. J. N. a. Sarmento, A. H. Clement, and G. Delhommeau, "A 3D boundary element code for the analysis of OWC wave-power plants," *Proc. 1999 Ninth Int. Offshore Polar Eng. Conf. (Volume 1), Brest, Fr. 30 May - 4 June 1999*, vol. I, pp. 188–195, 1999.

11- Y. Delauré and A. Lewis, "3D hydrodynamic modelling of fixed oscillating water column wave power plant by a boundary element methods," *Ocean Eng.*, vol. 30, pp. 309–330, 2003.

12- A. Iturrioz, R. Guanche, J. L. Lara, C. Vidal, and I. J. Losada, "Validation of OpenFOAM® for Oscillating Water Column three-dimensional modeling," *Ocean Eng.*, vol. 107, pp. 222–236, 2015.

13- T. Vyzikas, S. Deshoulières, O. Giroux, M. Barton, and D. Greaves, "Numerical study of fixed Oscillating Water Column with RANS-type two-phase CFD model," *Renew. Energy*, vol. 102, pp. 294–305, 2017.

14- I. Simonetti, L. Cappietti, H. Elsafti, and H. Oumeraci, "Optimization of the geometry and the turbine induced damping for fixed detached and asymmetric OWC devices: A numerical study," *Energy*, vol. 139, pp. 1197–1209, 2017.

15- I. Simonetti, L. Cappietti, H. Elsafti, and H. Oumeraci, "Evaluation of air compressibility effects on the performance of fixed OWC wave energy converters using CFD modelling," *Renew. Energy*, vol. 119, pp. 741–753, 2018.

16- A. Kamath, H. Bihs, and Ø. A. Arntsen, "Numerical investigations of the hydrodynamics of an oscillating water column device," *Ocean Eng.*, vol. 102, pp. 40–50, Jul. 2015.

17- M. T. Morris-Thomas, R. J. Irvin, and K. P. Thiagarajan, "An Investigation Into the Hydrodynamic Efficiency of an Oscillating Water Column," *J. Offshore Mech. Arct. Eng.*, vol. 129, no. 4, p. 273, 2007.

18- T. Vyzikas, S. Deshoulières, M. Barton, O. Giroux, D. Greaves, and D. Simmonds, "Experimental investigation of different geometries of fixed oscillating water column devices," *Renew. Energy*, vol. 104, pp. 248–258, Apr. 2017.

19- A. Viviano, S. Naty, E. Foti, T. Bruce, W. Allsop, and D. Vicinanza, "Large-scale experiments on the behaviour of a generalised Oscillating Water Column under random waves," *Renew. Energy*, vol. 99, pp. 875–887, Dec. 2016.

20- D.-Z. Ning, R.-Q. Wang, Q.-P. Zou, and B. Teng, "An experimental investigation of hydrodynamics of a

fixed OWC Wave Energy Converter," *Appl. Energy*, vol. 168, pp. 636–648, Apr. 2016.

21- W. Sheng, B. Flannery, A. Lewis, and R. Alcorn, "Experimental Studies of a Floating Cylindrical OWC WEC," in *Ocean Space Utilization; Ocean Renewable Energy*, 2012, vol. 7, p. 169.

22- I. Crema, I. Simonetti, L. Cappietti, and H. Oumeraci, "Laboratory experiments on oscillating water column wave energy converters integrated in a very large floating structure," in *the 11th International Conference of European Wave and Tidal Energy EWTEC*, 2015, pp. 1–7.

23- A. Elhanafi and C. J. Kim, "Experimental and numerical investigation on wave height and power take–off damping effects on the hydrodynamic performance of an offshore–stationary OWC wave energy converter," *Renew. Energy*, vol. 125, pp. 518–528, 2018.

24- A. Elhanafi, A. Fleming, G. Macfarlane, and Z. Leong, "Numerical hydrodynamic analysis of an offshore stationary–floating oscillating water column–wave energy converter using CFD," *Int. J. Nav. Archit. Ocean Eng.*, vol. 9, no. 1, pp. 77–99, 2017.

25- A. Elhanafi, G. Macfarlane, A. Fleming, and Z. Leong, "Investigations on 3D effects and correlation between wave height and lip submergence of an offshore stationary OWC wave energy converter," *Appl. Ocean Res.*, vol. 64, pp. 203–216, 2017.

26- M. Zabihi, S. Mazaheri, and M. Montazeri-Namin, "Experimental hydrodynamic investigation of a fixed offshore Oscillating Water Column device," *Applied Ocean Research Journal*, under revision, 2018.

27- A. B. Rabinovich, "Seiches and Harbour Oscillations," in *Handbook of Coastal and Ocean Engineering*, 2009, pp. 193–236.

28- C. Faraci, P. Scandura, E. Foti, Reflection of sea waves by combined caissons, J.Waterw. Port, Coast. Ocean Eng. 2015.

29- E. P. D. Mansard and E. R. Funke, "The Measurement of Incident and Reflected Spectra Using a Least Squares Method," *Coast. Eng. 1980*, pp. 154–172, 1980.

INTERNATIONAL JOURNAL OF
COASTAL & OFFSHORE ENGINEERING IJCOE Vol.3/No. 3/Autumn 2018 (29-40)

Available online at: http://ijcoe.org/browse.php?a_code=A-10-116-2&sid=1&slc_lang=en

# Safety in Marine Operations

**Sirous F. Yasseri[1*], Hamid Bahai[2]**

[1*]*Corresponding author, Brunel University London; Sirous.Yasseri@Brunel.ac.uk;*
[2]*Brunel University London; Hamid.Bahai@Brune.ac.uk*

**ARTICLE INFO**

*Article History:*
Received: 6 Sep. 2018
Accepted: 12 Dec. 2018

*Keywords:*
Situational Awareness
Marine Operation
Marine Installation Safety
Marine Domain Awareness

**ABSTRACT**

Safety in marine operations primarily depends on forward-planning and people being aware of their surroundings and managing the presence of others in the same arena at the same time. Marine operations must contend with challenging environments and hazards that require greater domain awareness; especially when many operators from different organisations are working in the same area. Being aware of what is going on around you in a marine domain, is termed Marine Domain Awareness (MDA), which involves the perception and understanding of environmental factors, their meaning and effects, and foreseeing their likely status and impact in the near future. This paper applies Situational Awareness (SA) concepts to the safety of marine operations and proposes a model for developing an information exchange system to enhance marine operational safety. The proposed model enhances MDA and can help in developing procedures and training programs to promote domain awareness. A framework for the safe marine operation is outlined in this paper.

## 1. Introduction

Marine operations take place in an arena where members of several different organizations are required to work together within the same space and time. In such situations, several activities will take place in parallel. Participants may have incomplete or inaccurate knowledge of the whole operation, as well as the activity of others, which could affect their safety. Safety in a marine domain primarily depends on people working together and being aware of their surroundings and activities of other people.

This paper refers to the arena where activities are taking place as the "marine domain", and people being aware of what is going on in the domain as Marine Domain Awareness (MDA). MDA is defined as the effective understanding of anything associated with the marine operational arena (with its spatial and temporal boundaries), which could adversely impact personnel safety or the environment. For this, information/data must be collected, analysed, understood and reported to those who need to know. Collected information should be shared with all people and organisations that are legitimately present in the arena. The collected data should identify likely hazards that need be avoided, controlled and mitigated. For the purpose of this paper, the goal of MDA is to establish an adequate level of operational and situational awareness for working in a shared domain, while considering the safety of others and operational requirements. MDA is the application of Situational Awareness (SA) to the marine domain. MDA is a critical, yet not a fully developed component, for all marine operations. The Navy uses the term MDA to mean intelligence gathering and surveillance, which is only one element of MDA as described here.

*Effective understanding* occurs when a decision-maker has all the relevant data, as well as a good comprehension of it, enabling him/her to take appropriate actions. MDA consists of what is observable and known (Situation Awareness), as well as what is anticipated or suspected (Hazard Awareness). It is important that these two components are brought together to provide the decision maker with reliable and actionable information. The term "effective understanding" is meant to acknowledge that information requirements may vary depending upon the task at hand. Therefore, MDA equates to the correct understanding of the content, activity patterns, changes, and potential hazards in the operational arena.

Figure 1 summarises the basic principles of marine domain awareness as described in this paper. The concept of MDA is the cornerstone of the safety of marine operation

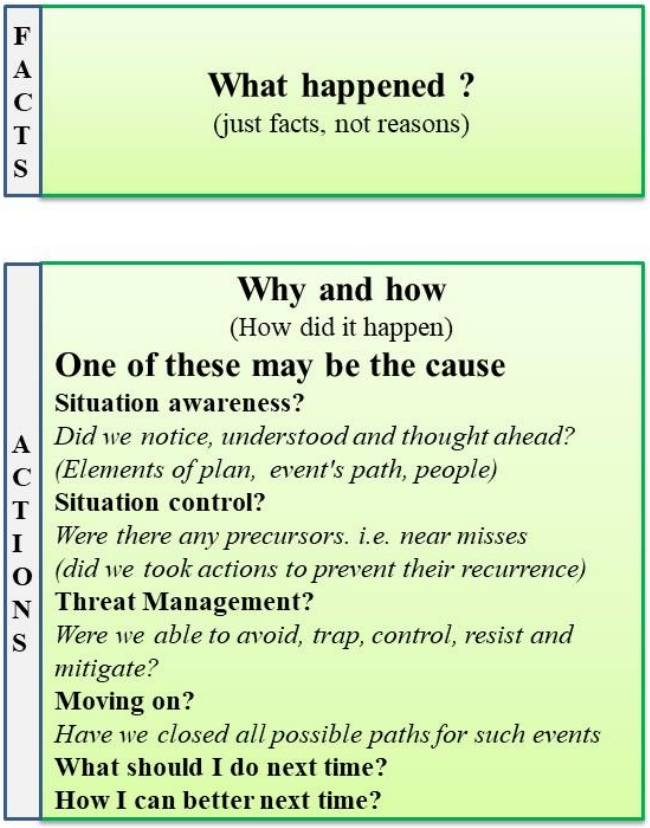


**Figure 1: The basic ideas of using SA in marine operations.**

Every individual has a different level of SA depending upon his/her own perception of reality, experience and knowledge. The situational awareness level of the person in charge determines the situational awareness level of a team. This is contrary to the belief that the team's level of awareness is the sum of the individual members' awareness (Garland and Endsley [12]). *Failures of situation awareness and situational assessment overwhelmingly predominate, being a causal factor in the majority of those accidents attributed to human error*. (Baker and Seah [2])

Codes of practice such as ISO 19901-6:2009 [22], DNV H101 and H102 [4 and 5] provide guidance for the planning and engineering of marine operations, encompassing the design and analysis of the components, systems, equipment and procedures required to perform marine operations, as well as the methods or procedures developed to carry them out safely. These codes, however, do not give much guidance on the influence of human elements. G-OMO [15], mentions SA, but the emphasis is the first element of the SA model, which is 'knowing what is happening around you'.

The claim is that good situation awareness results in good decision making, which in turn leads to a good outcome. Awareness is a variable state, and that state can only be successfully maintained by continued re-assessment the situation.

The aim of this paper is to detail a framework for the safe marine operation.

## 2. Situational Awareness

Awareness of what is happening in a marine arena, whether it is happening below, on, or above the water is a major step towards preventing accidents (Boraz [3]). Understanding the environment, judging the consequence of one's actions and the potential risks, are necessary components for safe operations. The method of understanding a situation is known as Situation Awareness (SA), and the application of the SA principle to marine operations is termed as Marine Domain Awareness (MDA), where the generic SA rules (Endsley [2012]) are adapted to the marine domain. The goal of MDA is to establish a level of situational awareness, for working in the shared marine domain (Harrald and Jefferson [18]), while not adversely affecting the safety of self, others and the operations. Figure 2 shows the steps of assuring safe marine operations. In order to make a decision, the decision maker must start with a situation assessment by first identifying any potential hazards. These include existing hazards, as well as things that could become hazardous if their intensity or location changes. The movement, in time and space, of these potential hazards must be predicted to the location relevant to the decision maker.

This study starts by knowing what is going on by asking questions like "What could go wrong?" "Who is doing what?" "What has happened before?" or "What could happen next?" … and so on, and then trying to eliminate or avoid any identified potential hazards. Any hazard identification is naturally incomplete, errors will inevitably occur and systems must be in place to prevent and control them. If by any chance, a hazard is not detected, and hence no control is in place, then undesirable events could follow. Hence, there is a need for a last line of defence to mitigate their consequences.

Figure 3 shows the abstraction of two major elements for safe operations, namely Understanding (sense-making) and Resolution (decision making). Sensemaking is an attempt to understand what has happened and what is happening. The decision maker then asks "What should we do?"

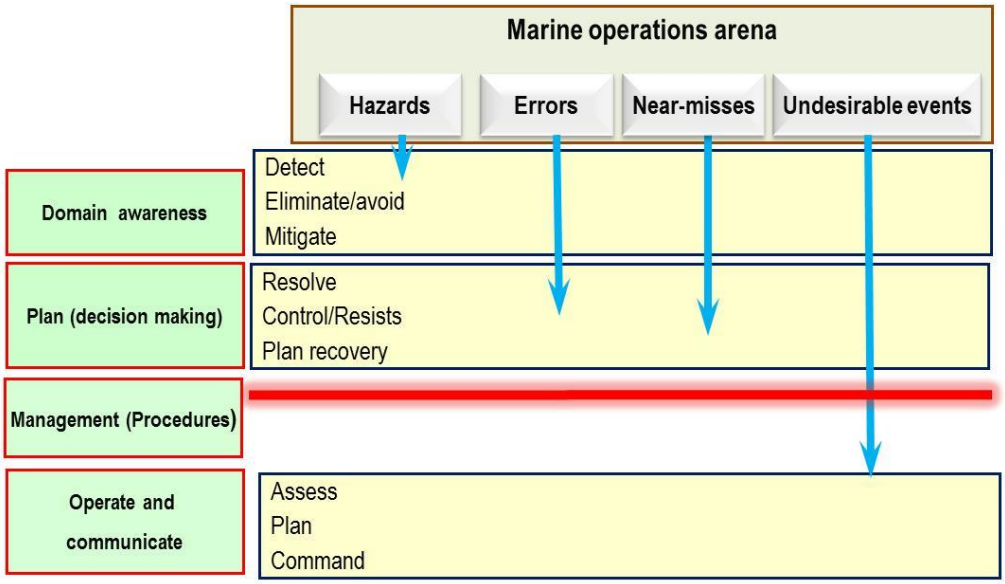


**Figure 2: Steps of assuring safe marine operation**

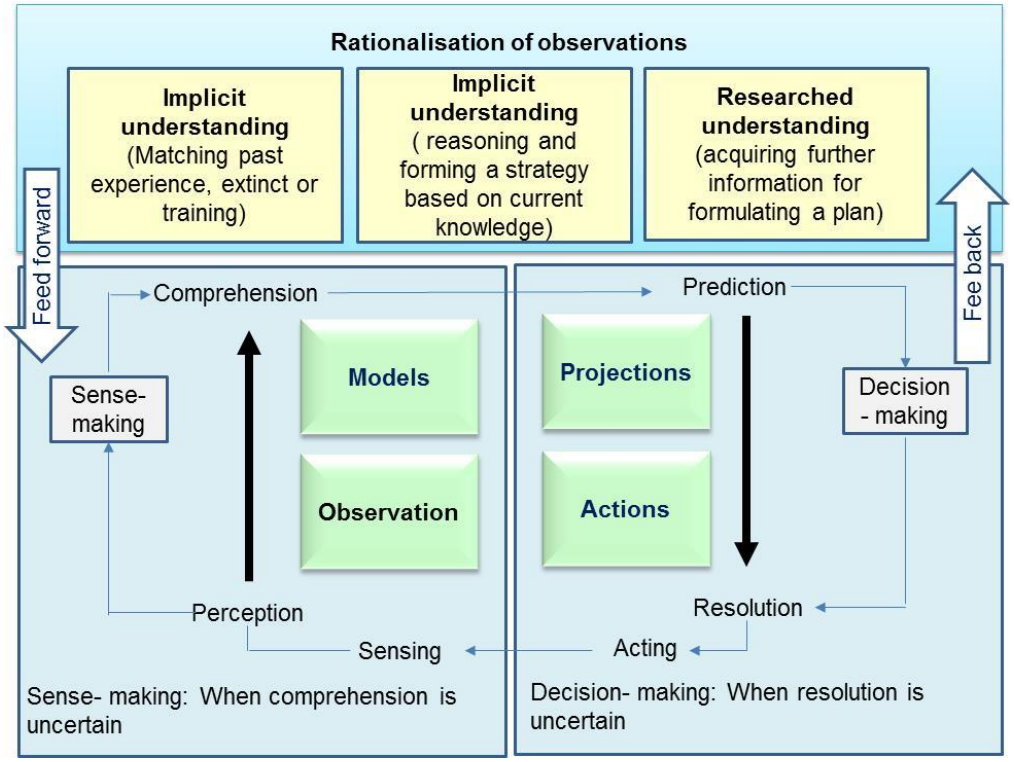


**Figure 3: Sensemaking and decision making**

The left-hand side shows information, which must be gleaned from the real world, and is fuzzy. If the implication of the obtained data is not immediately clear, then a mental model is used for sense-making; (the upper part of Figure 3). Such mental models may be based on past encounters, training or calculations and use of analytical methods (i.e. reasoned), new by research or assistance from experts. A decision is then made based on the forecasted outcome. In light of the likely consequences of the decision, the forecast may be revised.

Pilots developed the SA concept during World War I (Stanton et al, 2001). After World War 2, analysis of air combats showed that cognitive ability played a large role in combat ability; 80% of all planes were shot down by 15% of pilots. A large majority of 'combat aces' survived the war. Flying skill or gunnery were not predictors of combat success (Jones and Endsley [23]). At this time, German and Allied Air Force officers noted that a large proportion of fighter pilots that were hit did not realise that they were under attack before their plane was destroyed (Nardon [24]). The term, "Space Situational Awareness" was coined by the US Air Force around this time.

In the late 1980s, interest spread to other domains such as the military (e.g. Endsley [7]), driving (Kaber and Ma [17]), and medicine (Parush et al [25], and

Wright et al [29]). However, with the exception of one article (Hudson & van der Graaf [21]), the concept has remained relatively unknown in civil marine operations. Lately, Finch [11] proposed a model for Undersea Domain Awareness. Endsley [6] defines situation awareness informally and intuitively as "knowing what's going on" and, more formally, as: *"Situation awareness is the perception of the elements of the environment within a volume of time and space, the comprehension of their meaning, and the projection of their status in the near future."* This definition appears to have stood the test of time, and it is also expressed in similar terms by other authors. SA is also defined as "up-to-the-minute cognizance required operating or maintaining a system" (Adams et al 1995). In other words, SA is the ability to successfully pay attention to, and monitor, the environment and essentially 'think ahead', in order to evaluate the risk of an accident occurring.

Endsley [8 and 9] differentiates between situation awareness, *"a state of knowledge"*, and situation assessment, *"process of achieving, acquiring, or maintaining SA."* This distinction becomes important when trying to apply SA to marine operations. Since situation awareness is "a state of knowledge", it resides primarily in the minds of humans (cognitive), while situation assessment is a process, which requires "sense-making". Endsley also noted that:

*"SA, decision making, and performance are different stages with different factors influencing them and with wholly different approaches for dealing with each of them; thus it is important to treat these constructs separately."*

In the context of Marine operations, Situational Awareness may be defined as (Garland and Endsley, [12]):

*"Knowledge and understanding of the unfolding events which promotes timely, relevant and accurate assessment of actions of self, team-members, and other participants and operations, within the working arena in order to facilitate accurate decision making."* This requires an informational perspective and skill that fosters an ability to determine quickly the context, relevance and consequence of events as they unfold.

The term *situational awareness* describes the awareness of a situation that exists at a particular point in time (Endsley [8]). In some instances, information on the unfolding of events that preceded the current situation may also be relevant, as well as insight into how the situation is likely to unfold. The components of a situation include the mission and constraints on the mission, the capabilities and intentions of other operators, and key attributes of the operation. *Understanding* involves having adequate knowledge to be able to draw inferences about the possible consequences of events, as well as sufficient ability to predict future patterns (Endsley [9]).

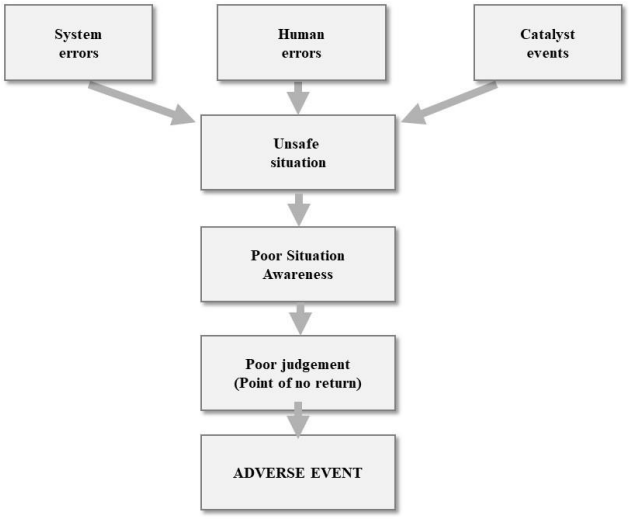


**Figure4: Chain of events leading to a disaster**

In general, a disaster follows a chain of events with some contribution from the human elements (Figure 4). Modern systems are designed to be in a safe state if any part fails to operate properly. The phrase "safe state generally mean s safe shut down without incident. Despite every effort system errs could happen either triggered by human or by a combination of poor design and degradation augmented by human error.

Endsley [7] defined three *levels* of situation awareness (SA) that are: Perception (including "noticing"), Comprehension, and Projection (Figure 5). Clearly, success at higher levels depends on the success at lower levels, and on the decision maker's ability to predict the path of evolving events.

According to this model, SA begins with perception (Figure 5). *Perception* provides information about the status, attributes, and dynamics of relevant elements within the environment. Obviously, without a basic perception of important environmental factors, the likelihood of forming a correct picture of the situation is low. *Comprehension* of the situation encompasses how people combine, interpret, store, and retain information, as well as making sense of it. Thus, comprehension includes more than perceiving or attending to the information; it includes the integration of multiple pieces of information and a determination of their relevance to the underlying goals and the ability to infer or derive conclusions about the goals. Comprehension leads to an organised picture of the current situation with regards to the significance of objects and events. Furthermore, as a dynamic process, comprehension must combine new information with that which already exists to produce a meaningful picture of the evolving situation. The last level is knowledge of the status, the dynamics of the events, and the ability to make predictions based on that knowledge. These predictions represent a *Projection* of the elements of the environment (situation) into the near future (Endsley [6]).

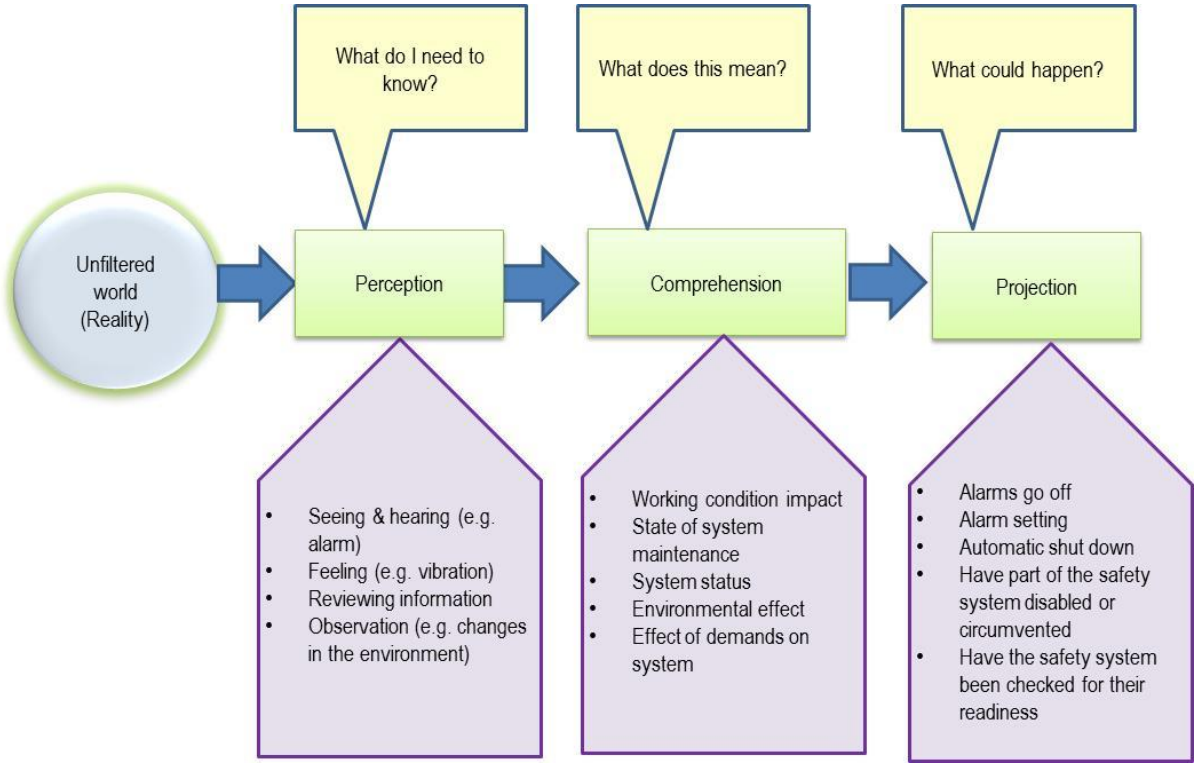


**Figure 5 Three elements in Endsley's model**

In Figure 5, Perception is the attempt to answer the question "What are the current facts?" Comprehension asks, "What is actually going on?" Projection asks, "What is most likely to happen if...?" All elements of Endsley's model run concurrently with continuous feedback and feedforward between them. As time marches on, any analysis will provide a higher level of understanding and transparency to the decision maker. SA is not action or performance. An operator with excellent SA of a failing system may not possess the knowledge of procedures to remedy the failures, or may not have the execution skills to implement the required remedy. In contrast, where automation can support effective performance, it is quite possible to have a good appreciation of the system performance in the absence of good SA. Within a few years of the appearance of the Endsley's article [7], the issue of team situation awareness emerged as an important part in understanding team dynamics: What does each worker know about the understanding and workload of his co-workers? and How is this supported by inter-worker communications and technology? -(Endsley & Robertson [10]). An issue of critical concern is how the concept of the "Team SA" extends beyond the collective average, or the sum of the individual SAs who make up the team (Kaber and Endsley [16])

In Figure 5, Perception is the attempt to answer the question "What are the current facts?" Comprehension asks, "What is actually going on?" Projection asks, "What is most likely to happen if...?" All elements of Endsley's model run concurrently with continuous feedback and feedforward between them. As time marches on, any analysis will provide a higher level of understanding and transparency to the decision maker. SA is not action or performance. An operator with excellent SA of a failing system may not possess the knowledge of procedures to remedy the failures, or may not have the execution skills to implement the required remedy. In contrast, where automation can support effective performance, it is quite possible to have a good appreciation of the system performance in the absence of good SA. Within a few years of the appearance of the Endsley's article [7], the issue of team situation awareness emerged as an important part in understanding team dynamics: What does each worker know about the understanding and workload of his co-workers? and How is this supported by inter-worker communications and technology? -(Endsley & Robertson [10]). An issue of critical concern is how the concept of the "Team SA" extends beyond the collective average, or the sum of the individual SAs who make up the team (Kaber and Endsley [16])

## 3. Endsley's Model

Situation awareness is recognised as a critical enabler for operational effectiveness and is a central element in contemporary system design approaches (Smith and Hancock [27]. Endsley [6] presents a model of situation awareness that highlights a number of issues relevant to the understanding and measurement of situation awareness. The model includes a consideration of the role of limited attention and working memory, mental models, pattern matching and critical cues, ties between situation awareness and automatic action selection, categorization, data-driven and goal-driven processes, expectations and dynamic goal selection (see Figure 6). Endsley's model defines situation awareness in terms of three levels:

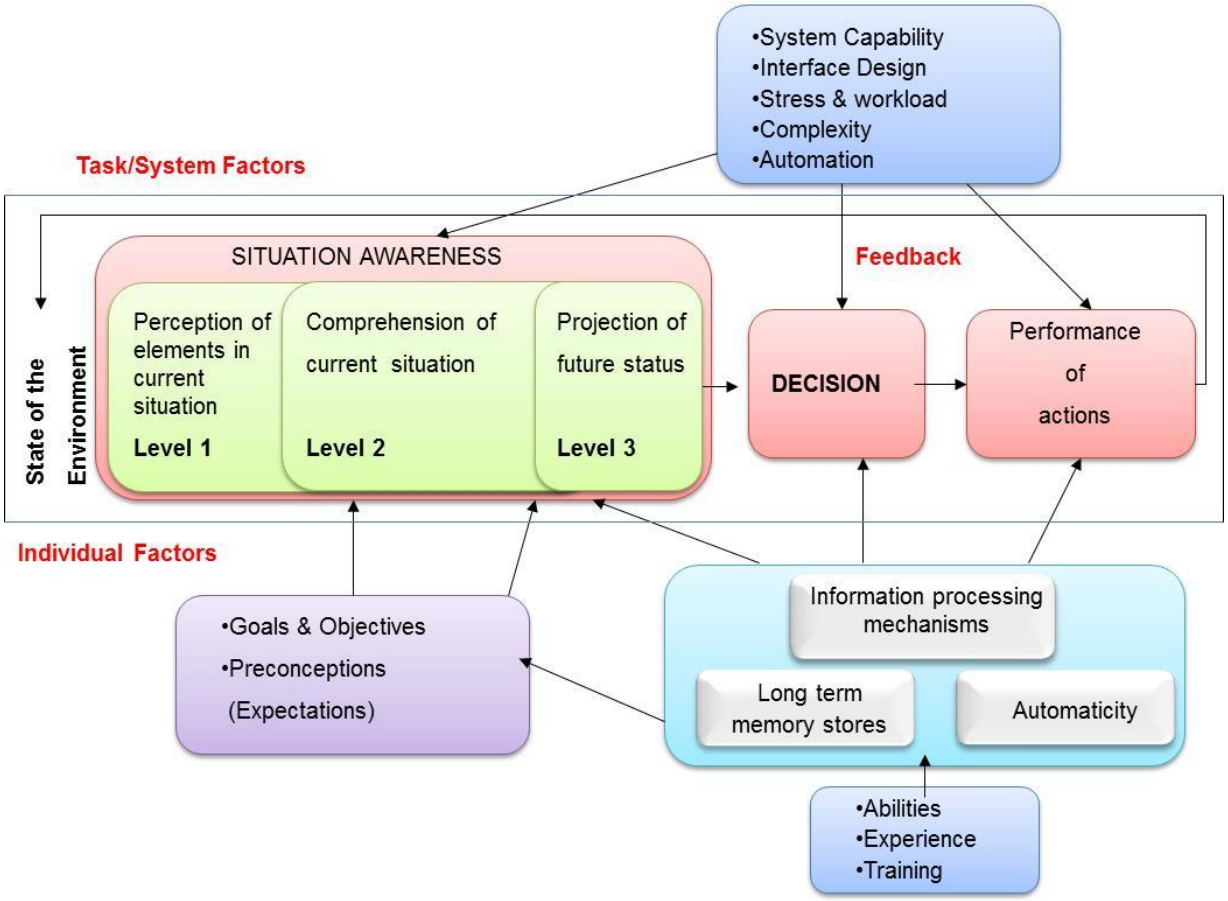


**Figure 6: Endsley's Model of Situation Awareness**

- **Level 1 – Perception:** Perception of environmental cues is fundamental to situation awareness. Without the basic perception of important information, the odds of forming an incorrect picture of the situation increase dramatically.
- **Level 2 – Comprehension:** The notion of situation awareness also encompasses how people combine, interpret, store and retain information. Thus, it includes more than just perceiving or attending to information; it also involves the integration (fusion) of multiple pieces of information and a determination of their relevance to the person's goals and objectives.
- **Level 3 – Projection:** At the highest level of situation awareness, the ability to forecast future events and dynamics is required. This ability to project from current events and dynamics to anticipate future events (and their implications) constitutes the basis for operationally-useful decision making, e.g. knowing that a threat to an aircraft is current and from a certain location, allows fighter pilots or military commanders to project that the aircraft is likely to be attacked in a given manner.

According to Endsley's model, situation awareness involves far more than simply perceiving information within the context of the environment. It also includes the importance of comprehending the *meaning* of the information in an integrated form, especially in terms of being able to understand the implications of the current situation in terms of future projected states. Such an understanding is of critical significance in making operationally and strategically effective decisions in the marine domain.

As marine operations become more knowledge-based, the notion of domain awareness, along with domain assessment, becomes increasingly important for describing and discussing operational procedures; with a lexical definition of "knowing what's going on." Thus, MDA is about "everything" related to acquiring situation knowledge in a complex dynamic environment such as marine operation (Figure 7).

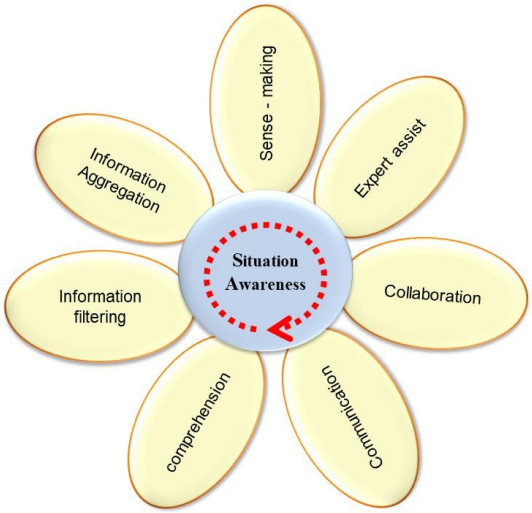


**Figure 7: Capability requirements of SA**

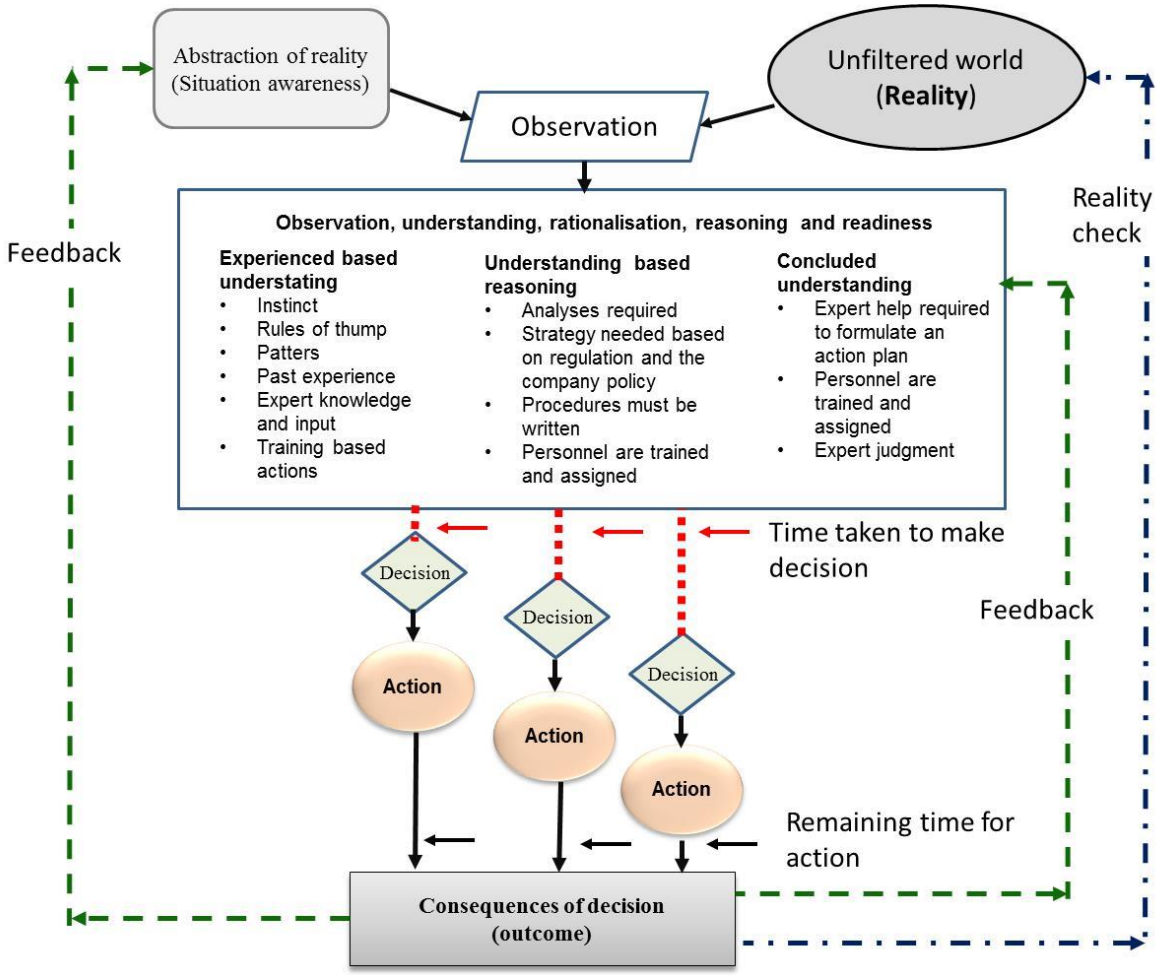


**Figure 8: The decision making process and penalty of taking too long to decide.**

A domain-specific account of SA for marine operations should depict the unique characteristics of activities, challenges and knowledge that are meaningful and relevant to the operators. Such an account should give practitioners insights to SA – what and how SA measurements should be collected in representative environments. Operators must deal with the inherent diversity of various company procedures; all of them valid in their own right, but may cause conflict when combined. MDA ultimately depends on the ability to deal with this heterogeneity - to aggregate, integrate and process task-relevant information in ways that support decision making in an operationally effective manner.

An evolving event takes a certain time to unfold and reach the target via unguarded paths. This governs the available time for observation, comprehension, decision-making and action. Figure 8 shows how resolution for action is achieved. The primary aim of SA is to shorten the time needed to decide. A faster decision by a prepared personal leaves more time to act, with a better chance of arresting the event.

## 4. Elements of MDA

In general, the notions of situation awareness used throughout the literature emphasises the perception and processing of subsets of environmental information. In particular, those informational subsets that are relevant to on-going needs and concerns, and which promote a selection of responses strategically aligned with operational goals and objectives. Inherent to such definitions is the notion of what is important (Figure 9).

Operators are often confronted with a dazzling array of data that must be perceived, comprehended and interpreted. Often such information is highly dynamic and complicated by uncertainty. What is important must be gleaned from masses of data, which is usually masked by irrelevant information (noise). The task confronting the operator is to filter information in a manner that avoids information overload and promotes the selective focus of available cognitive resources to those aspects of the incoming information stream that are of the greatest relevance to their monitoring and decision-making responsibilities

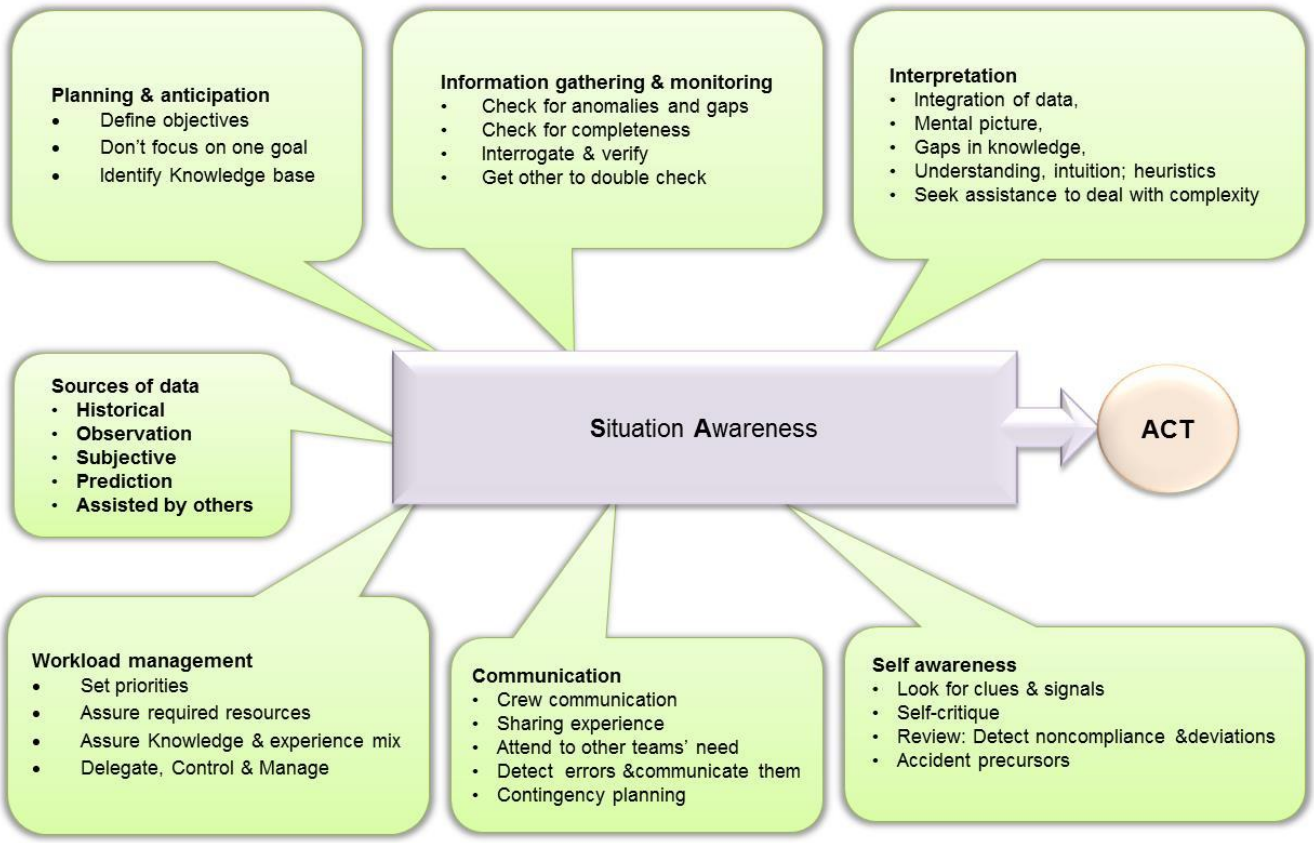


**Figure 9: Perceiving the environment and sense-making**

Information sources may be divided into three general categories based on chronology; information from the past, present and future (Figure 9). There is also a fourth category, which is subjective information, i.e. the observer's state of belief. Historical information is used for background and understanding of the general structure of what has gone wrong in the past. Current observations represent the state of the world. Predictive information attempts to explicitly present the future to the decision maker using a model. Moreover, the decision maker must decide if old information is still relevant and of value. As information ages, its value to a decision maker generally decreases. Finally, the subjective information category is coloured by factors such as training, confidence and the decision-makers bias. The basis for any prediction of a future state is a determination of the current state, combined with a model for how the world can change from that state.

Predictive information sometimes may be available to a decision maker. This is information that some source, external to the decision maker, produces. This is most useful when it can predict the location, time, or intensity of a hazard. However, this is rarely the case. Generally, current information is combined with other information gathered by observations, past cases, and this assembly is used to make sense of the state of the world. Predictive information is generally produced by putting data into a computer or human model. Therefore predictive information is only as reliable as the observations and the model itself. A decision maker must check the reliability of predictive information by comparing old observations with current observations and trends.

Endsley's (2012) definition of situation awareness encompasses the notion of spatial-temporal aspects of the perceived information. A critical part of situation awareness is the understanding of how much time is available until some event occurs or some action must be taken. The 'within a volume of space and time' phrase in Endsley's definition is intended to reflect the fact that operators should concentrate only the parts of the situation that are of interest to them, based not only on space (how far away an element is) but also how soon that element will have an impact on their goals and tasks - i.e., now and here (Sarter, and Woods, 1991). Such abilities depend on understanding the meaning and implications of events as they relate to operational objectives, and in this sense, knowledge becomes an inherent feature of the situation assessment and analysis process. To make informed decisions, the operator must be cognizant of all the relevant elements of the environment, what these elements mean, and how those elements will affect the operational environment over time (Smith and Hancock [27]).

## 5. Measuring MDA for Marine Operation

Measuring awareness of an individual or a team requires metrics and methods. Endsley [6] outlines a

number of issues of relevance to the derivation of SA metrics. She argues that such metrics need to:

- Measure the parameter they actually intend to measure and not be influenced by other processes.
- Provide the required sensitive and diagnostic insight into situation awareness, i.e. measures should indicate why aspects of a system design fail to improve or degrade situation awareness.
- Avoid substantially altering the design by providing biased data and altered behaviour.

Ideally, measurement of SA should not distract the operator from essential tasks, thereby compromising safety and adversely influencing on-going levels of situation awareness and task performance. However, it is possible to identify a number of problems confronting the adequate measurement of situation awareness using some metrics (Hudson and Graaf [21]). Firstly, the fact that decision making and performance are considered as distinct from situation awareness means that operational metrics cannot be based on the quality of decision outcomes or task performance criteria. With high levels of expertise, in well-understood environments, there may be a direct link between the quality of a decision and the situation awareness, whereby a good understanding of the situation leads directly to the selection of appropriate action from memory (Endsley [6]). However, individuals can still make poor decisions with good situational awareness. In some cases, the context may also dictate when the implementation, or non-implementation, of actions adversely, affect outcomes. Secondly, a focus on the processes by which individuals acquire information is largely insignificant from the perspective of measuring situation awareness (Endsley [6]). Different individuals may use different processes to arrive at the same state of knowledge, or they may arrive at different states of knowledge based on the same processes. Thirdly, measurement techniques that affect the allocation of attention resources should be avoided, as these are likely to compromise existing levels of situation awareness, especially in high workload and stressful situations (Endsley [6]). Finally, because measures of situation awareness often depend on the ability to recall situations and associated information states, it is important to consider human memory limitations when aiming to measure situation awareness.

## 6. Competencies

The phrase Marine Domain Awareness (MDA) is used to mean an effective comprehension and response to all information associated with a specific marine operation in a domain that could impact on safety, operations, or the environment. This requires managing information regarding vessels, tools, activities, people, and infrastructure. This is further complicated by the additional activity of sharing information among the stakeholders. MDA relies on the ability to build a comprehensive awareness of activities within the time and space of the marine operation. MDA's purpose is to generate actionable knowledge for the stakeholders. The quantity and depth of information collected from various sources need to be joined to create a common relevant picture that can be shared among the involved parties.

Endsley's theory of SA levels was tested in the marine domain by Grech and Horberry [14]. They conducted a study that focused on the lack of situational awareness among mariners by analysing 177 accident reports between the years 1987 and 2001. Their analyses revealed that 71% of human errors were associated with lack of situational awareness. Of the situational errors, 58% were associated with level 1 (failure to correctly perceive information, detect information or failure to monitor data), 32.7% were associated with level 2 (failure to comprehend information), and 8.8% were associated with level 3 (failure to project future actions or over-projection of current trends).

The analysis of information (i.e. analysing the domain) identifies threats. Courses of action are generated to mitigate deviations from approved procedures. The preferred alternative is selected from an evaluation of various alternatives using established criteria. The preferred alternative is planned in sufficient detail to direct the operation with a coordinated set of tasks. Both domain analysis and threat management functions are needed to achieve safety goals.

Table 1 show a listing of the required skills and their description, which is based upon the principle of Sensing, Assessing, Generating options, Selecting, and directing efforts. The analysis of the domain consists of data gathering, processing & dissemination – (termed analysing the domain) and command and control - (termed threat management) (Hoermann et al [19]). Knowing the nature of an event, a threat management plan can be developed, to intercept, mitigate or cope with the consequences of the residual threats. The success is postulated on the basis of contingency operational procedures, developed from data analysis, to counteract them.

An experienced decision maker is generally sceptical about 'normal' functioning conditions and is constantly making contingency plans for those circumstances when things might go wrong. The slightest change in an observed situation should trigger alarms and bring alternative plans of action to the foreground.

**Table 1: MDA Competencies**

| SA Skill | Description |
|---|---|
| Attention Management | Ability to determine priories and allocate resources accordingly. |
| Attention Span and Allocation | Ability of allocate attention to all tasks and focus adequately on each. Stay focused. |
| Information Gathering | Ability to determine what data is needed and organise its gathering. |
| Analyses, Comprehension and Interpretation | Ability to judge integrity of information, compare and integrate data from different sources, analyse them and make appropriate decision |
| Anticipation and contingency planning | Foresight. Ability to see where the actions would lead, projecting their consequences, and devise contingency plans to remedy the situation if things go wrong. |
| Common Sense balanced judgment | Ability to exercise a balanced judgment and have a sense of proportion |
| Recognition of SA impairment | Ability to recognize loss of SA |
| Recovery from loss of SA | Ability to rectify break down in SA |

Procedures are often used to help make the decision process easier or faster. They have the effect of relieving the decision maker from the responsibility for certain aspects of decision making. The decision maker simply has to assess the situation, find the pattern that best fits the situation, and then follow the prescribed procedure. A whole class of situations may be categorised by one procedure, along with the appropriate characteristics to classify the situation, and the corresponding choice or rule sets that should be followed. Such decision processes are established well in advance of any actual operation. The decision maker then needs only to gather enough data to determine the pattern and significance of variation on the theme, and then to apply the prescribed procedure. This will reduce the number of incorrect decisions that are made by decision makers in high-risk situations. Decision makers in the presence of high risk, tend to be aware of patterns for resolving situations, and are heavily influenced by them. The Army's "rules of engagement" is an example, which is designed to make the appropriate decisions depending on the situation encountered. Companies' procedures, as well as codes of practice, are also designed to help in decision making by identifying appropirte (and corrective) actions for every situation

## 7. Discussion

Elements of SA differ depending on the situation, but its nature and mechanisms could be described generically. Without the perception of the important information, our image of the reality would be incomplete or false. The SA concept exceeds mere perception and takes into account how humans combine, interpret, store and retain information (Endsley [6]). It is necessary to integrate multiple pieces of information and determine their relevance for a person's goals. But these are not all that is needed. At the highest level of SA, the ability to forecast future events and their dynamics is also required.

A large part of SA training is related to learning how to detect available patterns or options. A training programme should aim to teach these elements until they are performed without hesitation. Ability to be aware of what is going on can be taught, similar to driving. The majority of training relates to learning hazard identification, how to avoid them and what the options are if mitigations are needed; i.e., patterns of approved actions for every situation. However, the attention span and innate ability of individuals will differentiate between them.

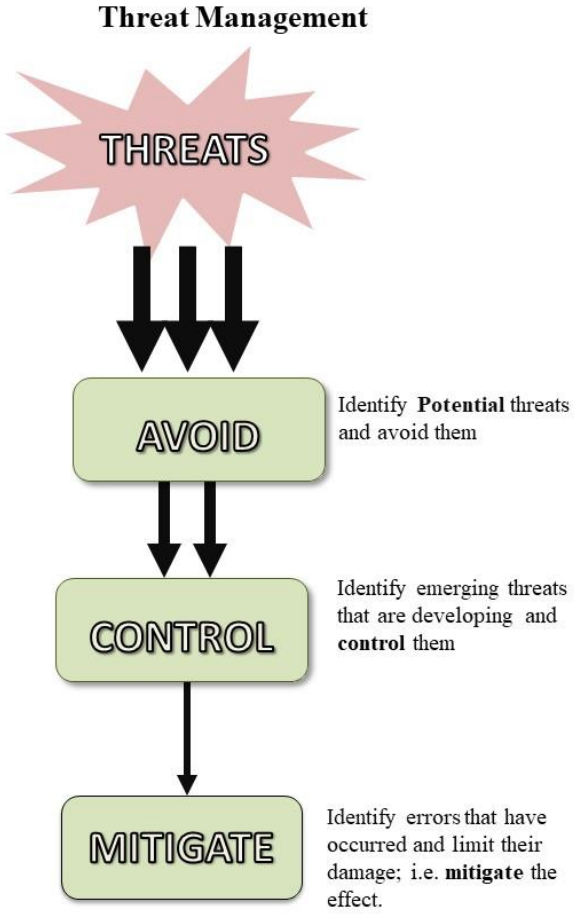


**Figure 10: Steps in threat management**

Domain Analysis is needs driven and includes, proving periodic and non-periodic information and support to each member of the other teams engaged in the arena for achieving the shared goals; hence each operator in the arena is both an information provider and consumer. By posting data to the designated interface member, the complete information becomes available for everyone who needs it. Factors which influence the results are; 1) Uncertainty and error in

what decision makers know; 2) How they act on the information they have; 3) The ability to collect the information needed. Such skills can be greatly enhanced by training.

The threat management (Figure 10) function is a command and control function. The commander on scene generates actions to avoid and mitigate residual threats. A preferred course of action is selected, with an evaluation of alternatives, to assure effectiveness and conformance with established criteria. The preferred alternative is planned in sufficient detail to be communicated to all stakeholders with a coordinated set of tasks.

Hone [20] reduced Endsley's model into three questions:

- Who is where? (Simplified from "…a person's perception of elements in the environment within a volume of time and space …")
- What are they doing? (Simplified from "… the comprehension of their meaning …")
- What they will do? (Simplified from "...the projection of their status in the near future")

As in the original Endsley's model, the three questions relate to a single individual viewpoint. In this simplification, it is assumed (Hone et al, 2005) that the "Who" in "Who is where?" also includes inanimate objects and environment features. Another simplification uses these three questions: What has gone before? What is going on? What is going to happen? Such simplification can help to operationalise SA in an emergency response or in a game of football where the situation changes very fast.

Marine operations typically involve the extensive use of information technologies for information gathering, communication, etc. and because these technologies are the fundamental tools for developing situation awareness, the content of such technologies have dominated the current research (Endsley [6]). However, some situations rely on raw sensory experience as input, with less use of technology and information systems. It is characterised by shorter response times, more immediate feedback, and more rapid fluctuations in relevant conditions (Grech et al [14]).

## 8. Concluding Remark

Understanding and responding correctly to complex situations, and anticipating consequences, are essential skills for the safety of marine operations. These skills require situation awareness (SA): i.e. the ability of the operator to take correct, timely actions. The claim is that superior SA will increase the probability (although not the certainty) of success through improved assessment of, and response to, unfolding events in the domain of marine operation.

Good SA cannot guarantee good decision making, but without it everything depends on chance. Errors can still occur even following well-defined rules - such as approved work methods, permit to work and procedures. Inadequacies, improper tools, operational constraints, poor judgment or bad execution of an appropriate response could lead to an unsafe situation. Furthermore, SA is influenced by the available time and mental ability to process information, and the fact that most situations are dynamic, which aggravates the problem, as it requires continuous adjustment.

Although poor SA does not preclude good outcomes (the chance element), it is reasonable to believe that good SA improves the likelihood of a good outcome. SA revolves around "knowing what is going on around you." Such knowing for untrained personnel originates from past experience, intuition and innate ability to be observant. It is argued that training, which is devised to teach competencies, can instil these abilities in people.

In conclusion, SA may be gained by answering four simple questions:

1. What has happened?
2. Where is everybody?
3. What is happening?
4. What could happen?

The rule-based framework outlined in this paper goes a long way towards safe marine operation, however, in a dynamic environment heuristics (gut feeling, the rule of thumb etc.) are still needed to shorten the decision making process to allow more time for reaction.

## 9. References

1. Adams, MJ, Tenney, YJ, and Pew, RW (1995). "Situation awareness and the cognitive management of complex systems," Human Factors, 37(1), 85-104.
2. Baker, CC and Seah, AK (2004). "Maritime Accidents and Human Performance: the Statistical Trail," MARTECH 2004, Singapore, 225-239,
3. Boraz SC. (2009). "Maritime Domain Awareness -Myths and Realities Naval War College Review," 62(3), 137-146.
4. DNV-OS-H10, (2011). Marine Operations, General, 35pp. https://rules.dnvgl.com/docs/pdf/DNV/codes/docs/2011-10/Os-H101.pdf
5. DNV-OS-H102, (2012). Marine Operations, Design and Fabrication. 35 pp. https://rules.dnvgl.com/docs/pdf/DNV/codes/docs/2012-01/Os-H102.pdf
6. Endsley M, (2012). Designing for Situation Awareness: An Approach to User-Centred Design. CRC Press; 2nd edition, 396pp
7. Endsley M (1998). "Situation Awareness in Aviation Systems," In Garland, DJ, Wise, JA and Hopkin, VD (Eds). Handbook of Aviation Human Errors. CRC Press; 1 edition. ISBN-10: 0805816801
8. Endsley, MR (2000a). "Theoretical underpinnings of situation awareness: A critical review," In M. R. Endsley & D. J. Garland (Eds.),

Situation awareness analysis and measurement, Mahwah, NJ: Lawrence Erlbaum Associates, 3-33.
9. Endsley, MR (2000b). " Situation models: An avenue to the modelling of mental models," Proceedings of the 14th Triennial Congress of the International Ergonomics Association and the 44th Annual Meeting of the Human Factors and Ergonomics Society, Santa Monica, CA: HFES, 1-61-1-64
10. Endsley, MR, and Robertson, MM (2000). "Training for situation awareness in individuals and teams," In M. R. Endsley & D. J. Garland (Eds.), Situation awareness analysis and measurement Mahwah, NJ: Lawrence Erlbaum Associates. 349-367.
11. Finch D (2011). "Comprehensive Undersea Domain Awareness: A Conceptual Model," Canadian Naval Review, 7(3), 21-26.
12. Garland DJ and Endsley MR (2000). Situation Awareness Analysis and Measurement, CRC Press, 371pp
13. Grech, MR., and Horberry, T (2002). "Human Error in Maritime Operations: Analysis of Accident Reports Using the Leximancer Tool," Brisbane: University of Queensland, Brisbane, 1-5.
14. Grech M, Horberry T. and Koester T (2008). Human Factors in the Maritime Domain, CRC Press, 216pp.
15. G-OMO (2013), Guidelines for Offshore Marine Operations Revision: 0611-1401 dated 06/11/2013, 292 pp.
16. Kaber DB, and Endsley M. (1998). "Team Situation Awareness for Process Control Safety and Performance," Process Safety Progress 17(1), 43-48
17. Kaber, DB and MA, R (2005. "Situation awareness and workload in driving while using adaptive cruise control and a cell phone*,"* International Journal of Industrial Ergonomics 35, 939–953
18. Harrald, J, and Jefferson, T (2007). "Shared Situational Awareness in Emergency Management Mitigation and Response," Proceedings of the 40th Hawaii International Conference on System Sciences 50(3): p. 44.
19. Hoermann H-J et al (2003), "Enhanced Safety through Situation Awareness Integration in training", ESSAI NLR-CR-2003-064, Project funded by the European Community under the 'Competitive and Sustainable Growth' Programme (1998-2002), 49 pp. http://www.transport-research.info/sites/default/files/project/documents/20060727_144319_28057_ESSAI_Final_Report.pdf
20. Hone, G, Martin, L, and Ayres, R. (2006). "Awareness – does the acronym "SA" still have any value?" Coalition Command and Control in the Networked Era, 11th ICCRTS conference, 14pp, http://www.dodccrp.org/events/11th_ICCRTS/html/papers/071.pdf
21. Hudson, PTW, & Graaf, GC, (1998). "The Rule of Three: Situation awareness in hazardous situations," paper SPE 46765 presented at the 1998 SPE International Conference on Health, Safety and Environment in Oil and Gas Exploration and Production, Caracas, Venezuela, 4pp.
22. ISO 19901-6:2009 Petroleum and natural gas industries - Specific requirements for offshore structures - Part 6: Marine operations
23. Jones, D G, and Endsley, MR (1996). "Sources of situation awareness errors in aviation," Aviation, Space, and Environmental Medicine, 67(6), 507-512
24. Nardon, L (2007). "Space Situational Awareness and International Policy," Document de travail 14, Paris, ifri Programme Espace**,** 8pp.
25. Parush, A, Hunter A, Campbell C, Calder L, Frank J, Ma Ch., Worthington, J, and Abbott C (2011). "Situational Awareness and Patient Safety," The Royal College of Physicians and Surgeons of Canada, 35pp.
26. Sarter, NB, and Woods, DD (1991). "Situation awareness: A critical but ill-defined phenomenon," The International Journal of Aviation Psychology, 1(1), 45-57.
27. Smith, K, and Hancock, PA (1994). "Situation awareness is adaptive, externally directed consciousness," In R.D. Gilson, D.J. Garland, and J.M. Koonce (Eds.), Situational awareness in complex systems (Daytona Beach, FL: Embry-Riddle Aeronautical University Press, 1994. 59-68.
28. Stanton, N. A.; Chambers, P. R. G. & Piggott, J. (2001) Situational awareness and safety. Safety Science 39 189-204.
29. Wright, SM. and Michael D. Fallacaro, MD (2011). "Predictors of Situation Awareness in Student Registered Nurse Anaesthetists," AANA Journal, 79(6), 484-490.

INTERNATIONAL JOURNAL OF
COASTAL & OFFSHORE ENGINEERING
IJCOE Vol.3/No. 3/Autumn 2018 (41-51)

Available online at: http://ijcoe.org/browse.php?a_code=A-10-184-1&sid=1&slc_lang=en

# Sensitivity of an Axi-Symmetric Tropical Cyclone Model to Two External Parameters

**Nafiseh Pegahfar [1]*, Maryam Gharaylou [2]**

[1]*Assistant Professor, Atmospheric Research Center, Iranian National Institute for Ocean-ography and Atmospheric Science, Tehran, Iran; pegahfar@inio.ac.ir*
[2]*Assistant Professor, Institute of Geophysics, University of Tehran, Tehran, Iran; gharaylo@ut.ac.ir*

**ARTICLE INFO**

*Article History:*
Received: 18 Oct. 2018
Accepted: 17 Dec. 2018

*Keywords:*
Tropical Cyclone Haiyan
Numerical Model
Convective Entropy Flux
External parameters

**ABSTRACT**

More realistic simulation of hazards caused by Tropical Cyclones (TCs) requires knowledge of the mechanisms that formulate tropical cyclone. Here, sensitivity of an idealized framework has been tested to investigate role of two external parameters in vertical entropy flux. The first parameter controls the ratio of width of eyewall and downdraft regions to radius of maximum wind and the second parameter controls radial decay of wind velocity between two regions. This numerical model used conservation principles, assumed axi-symmetry and steadiness to model TC vortex, and let ventilation be occurred via the path-ways of downdrafts outside eyewall and eddy fluxes directly into eyewall. To test this framework, Tropical Cyclone Haiyan (TCH, formed over the Western part of Pacific Ocean on 3 November 2013) has been selected. Two kinds of datasets including Joint Typhoon Warning Centers (JTWC) Best Track data of Japan Meteorology Agency and Global Forecast System Analysis (GFS-ANL) data have been used. The model has been run for 60 different configurations, based on change of the two external parameters and size of two random do-mains. The sensitivity of the modeled convective entropy flux to the applied changes has been examined via two different aspects of investigation. In the first aspect, terms of the reference equation of convective entropy flux have been considered and their responses to the changes have been studies. While in the second aspect, values of the convective entropy flux at TCH peak activity time (PAT), before and after that have been inspected. Results, obtained from the first aspect, obviously indicate that the increase of the first external parameter increases the all terms of the referred equation, while increase of the second external parameter influenced the terms differently. Also enlarging the domains' size does not impress the results similarly. Outcomes of the second aspect reveal that the implemented changes non-uniformly impact the values of the modeled convective entropy flux in the three considered times.

## 1. Introduction

Since Tropical Cyclone (TC) severe weather are most hazardous in coastal regions and caused extensive damage, loss of life and damaging floods hundreds of miles inland, achieving an entire body of knowledge of hurricane behavior is essential to model hurricane hazard (Vickery et al. 2009; Pielke Jr. et al., 2008). Built up more property along the world's vulnerable coastlines would increase the need of guarantee of TC damage in future. Hence, it is important to understand the physics of TCs in order to improve the ability for short- and long-term forecasts. To understand TC characteristic, various parts of that including inner-core (Montgomery and Smith, 2014; Chen et al. 2018), outer-core (Wang, 2012; Lee et al., 2010; Lin et al. 2017; Schenkel et al. 2018) and TC environment (Jones, 1995; Smith et al., 2000) have been considered. In addition, various physical parameters consist of dynamic and thermodynamic ones have been utilized to hypothesize a mechanism by which TC's intensity is affected. Observations indicated that a TC (I) only develops where significant potential heat flux from sea exists, and (II) decays over land even when plentiful amount of moisture and instability exist.

Environmental wind shear is a challenging factor in TC prediction and is observed to be generally detrimental to tropical cyclogenesis (McBride and Zehr, 1981; Zehr, 1992), and is an important component of empirical genesis indices (DeMaria et al., 2001; Emanuel and Nolan, 2004). Numerical modeling studies showed that sufficiently strong vertical wind shear impedes the development of incipient vortices (Tory et al., 2007; Nolan and Rappin, 2008). However, weak wind shear may aid TC genesis by forcing synoptic-scale ascent, especially in baroclinic environments (Davis and Bosart, 2006; Nolan and McGauley, 2012).

One of indirect effects of wind shear is intrusion of low-equivalent potential temperature air into the inner core of a TC that ventilates the incipient disturbance. Advection of environmental dry flow removes the condensation heat from the vortex and prevents TC deepening by decreasing the efficiency of TC heat engine (Nolan, 2007; Marin et al., 2009). Low-entropy entrance at midlevel is hypothesized as a mechanism by which the environmental vertical wind shear can constrain a TC's intensity. Therefore, entropy and also entropy-dependent parameters have been specially considered in developing of some idealized frameworks assessing TC intensity (Emanuel, 1995). These parameters include air-sea thermodynamic disequilibrium (Emanuel, 1986; Emanuel et al., 2004), entropy deficit (Tang and Camargo, 2014; Bruyere et al., 2012), entropy flux (Bryan and Rutonno, 2009). Thermodynamic disequilibrium between the ocean and the atmosphere derives Carnot engine of mature TC and is a principle factor in definition of potential intensity (Emanuel, 1991). Emanuel et al. (2008) showed that entropy deficit between boundary layer and midlevel should be increased with global warming and affect TC formation and intensification. Frank and Ritchie (2001) and Wong and Chan (2004) investigated ventilation (as vertical entropy flux) of the upper level warm core during TC lifetime and Riehl (1951) and Kleinschmidt (1951) studied surface and convective entropy fluxes from ocean during a TC intensification. Results of investigations led to use of entropy as an important parameter in various hypothesis describing both dynamical and thermodynamical mechanisms in TC formation and intensification. Tang and Emanuel (2010) developed a theoretical framework to assess how entropy flux affects TC intensity via two possible pathways (low-level pathway and mid-level pathway). They evaluated that framework for ventilation and potential intensity with fixed values of external parameters.

In this research, the mentioned theoretical concept (with a private source code) has been utilized and the related code has been written by the authors to examine dependency of the convective entropy flux on various values of two external parameters. Following, the theoretical framework (Sec. 2), data and methods (Sec. 3), results and discussion (Sec. 4), summary and conclusions (Sec.5) are presented.

## 2. Theoretical Framework

The source code for this framework is not in the public domain, so we had to develop this algorithm independently. The applied model is based on conservation principles and closely parallels that of Bister and Emanuel (1998). Throughout the derivation, axisymmetry, steadiness and slantwise neutrality (requiring that saturation isentropes be congruent to angular momentum surfaces) are assumed to model TC vortex.

Pseudo-adiabatic entropy has been calculated using the relation defined by Bryan (2008) as:

$$s = \left(c_{pd} + c_l r_v\right)\ln(T/T_R) - R_d \ln(p_d/p_0) + \frac{L_{v0} r_v}{T} - R_v r_v \ln(H) \qquad (1)$$
$$p_d = p - e, \quad e = (r_v * p)/(0.622 + r_v),$$

where the constants of $c_{pd} = 1005$ J/(kgK), $c_l = 4218$ J/(kgK) and $L_{v0} = 2.55 \times 10^{-6}$J/kg are the specific heat at constant pressure for dry air, specific heat for liquid water and latent heat, respectively. The gas constants for water vapor and dry air have been included as $R_v = 461.51$ J/(kgK) and $R_d = 287.05$ J/(kgK), and the constants of $T_R = 273.15$ K and $p_R = 1000$ hPa denote the freezing point of water and reference pressure, in that order. Also the variables of $T$, $p_d$, $H$, $e$, $p$ and $r_v$ demonstrate the temperature, partial pressure for dry air, humidity, water vapor pressure, pressure and water vapor mixing ratio, correspondingly.

The first law of thermodynamics for saturated conditions is combined with the momentum equations and a pseudo-adiabatic assumption, ignoring the contribution of liquid water and ice to the entropy ($s$) is used. It is worthwhile to be noted that unbalanced effects are not absolutely critical to describe the basic behavior of the intensity of ventilation-modified TC. Then the equations are integrated around a closed circuit bounded by two isotherms (Fig. 1a). To achieve the neutrality constrain, the sub-cloud layer is divided up in to two regions, as sketched in Fig. 1b including an "inner" region from $r_1$ to $r_2$ centered around the radius of maximum wind and an "outer" region from $r_2$ to $r_3$. Sources of entropy in both regions include turbulent fluxes ($F_s$), dissipative heating (H), and fluxes by the mean secondary circulation (lateral fluxes). The convective entropy flux, $F_s(z = h) = \overline{\acute{w}\acute{s}}$, through the top of the sub-cloud layer is included in the outer region. Convective downdrafts, in particular, driven by evaporation of rain into the sub-saturated air, are supplied by eddy entropy fluxes in the free troposphere, u′s′, as will be explained later. In a steady state, the entropy flux by

the mean transverse circulation through the boundaries of the sub-cloud layer of the control volume is adequate to the sum of internal sources and sinks of entropy. Then, entropy is assumed constant with height in the sub-cloud layer. The aerodynamic flux formula for the surface flux of entropy is

$$F_s(z=0) = -C_k|u|\,(s^*_{SST} - s_b), \tag{2}$$

where $C_k$ is the enthalpy coefficient, $u$ is wind velocity at surface, $s^*_{SST}$ is the saturation entropy at the sea surface and $s_b$ is the sub-cloud layer entropy. To show the contribution of dissipative heating to the entropy equation, the expression of

$$\int_0^h H dz = \frac{C_D}{T_s}|\mathbf{u}|^3 \tag{3}$$

introduced by Bister and Emanuel (1998), has been used (where the constant of $C_D$ is the drag coefficient and $T_s$ is the surface temperature). To apply the needed approximations, u is expressed as some fraction of the maximum wind velocity,$u_m$, and r (radial distance of u from TC center) is showed as some proportion of the radius of the maximum wind, $r_m$, both in the following fashions of

$$u = \begin{cases} u_m & r_1 < r < r_2 \\ \gamma u_m & r_2 < r < r_3 \end{cases}, \quad r = \begin{cases} r_m & r_1 < r < r_2 \\ \alpha r_m & r_2 < r < r_3 \end{cases} \tag{4}$$

Here, $\gamma$ controls the radial decay of wind and $\alpha$ controls the ratio of the width of both the inner and outer regions to the radius of maximum wind (Fig. 1b). By assuming (I) the turbulent flux of angular momentum at the surface as the aerodynamic flux formula of

$$F_M(z=0) = -C_D|u|r\,v, \tag{5}$$

where v is the azimuthal velocity, and (II) an expression for $< u >$ in the outer-region as

$$< u > \approx -\frac{C_D|u_m|r_m}{h}, \tag{6}$$

the relation of convective entropy flux is obtained as

$$\overline{\acute{w}\acute{s}} = \frac{C_D\gamma|u_m|\alpha}{\alpha - 1}(s_b^o - s_b^i) + C_k\gamma|u_m|(s^*_{SST} - s_a) + \frac{C_D}{T_s}\gamma^3|u_m|^3 \tag{7}$$

where $\overline{\acute{w}\acute{s}}$ is the convective entropy flux, $s_a$ is an ambient value of saturation moist entropy, $s_b^i$ is the sub-cloud layer entropy of the inner region, and $s_b^o$ is the sub-cloud layer entropy of the outer region at $r_3$. The "upwind" like approximation where $s_b^o = s_a$ can be used.

Tang (2010) assumed equal width for both regions ($\alpha = 1$) to simplify the analysis and allocated a value to $\alpha$ that roughly showed the characteristic width of a TC's eyewall. It is worthwhile to note that increase of $\alpha$ increases the radial intrusion of dry air to sub-cloud layer and also allows more surface flux be included. In greater value of $\gamma$ these effects offset another one and $\alpha$ variation leads to ventilation change. Also $\gamma$ value controls the recovery of the downdrafts. Tang and Emanuel (2010) used $0 < \alpha < 3$ and $0.3 < \gamma < 1$ and reported inertially unstable combinations for ventilation and reached a single curve that was invariant across all thermodynamic states. Tang and Emanuel (2010) stated that evaluation of this curve in the nature needs high density time and space at midlevel that is out of the abilities of this research and introduced numerical simulations of ventilated TC as a tool to test this sensible approach.

In the present work, effects of various external parameters have been examined for entropy and its vertical flux during a selected TC.

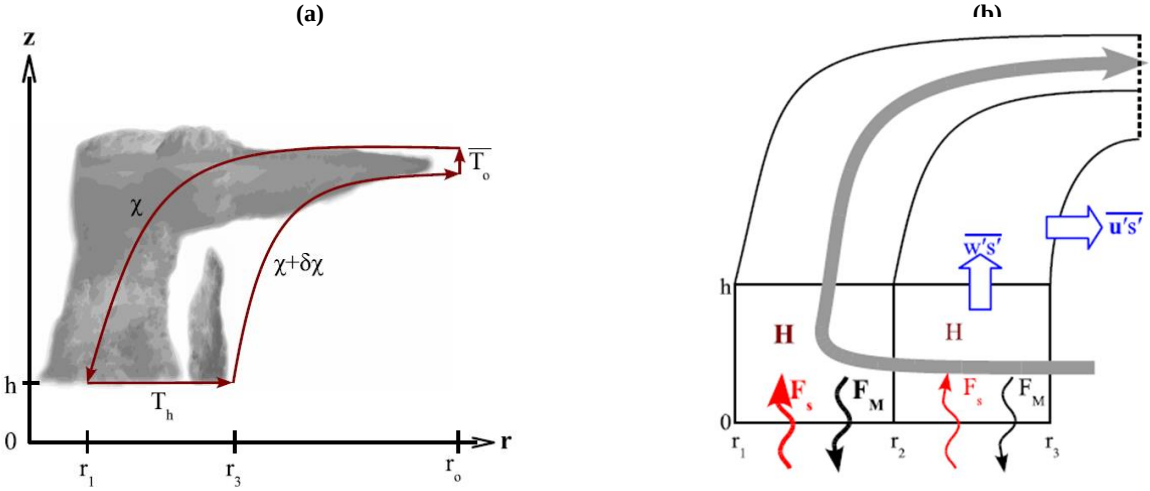


**Figure 1 (a) Closed circuit around which entropy is evaluated. Circuit consists of two isotherms, temperature at cloud base height ($T_h$) and temperature at tropopause height ($T_o$), and two contours of constant $\chi$, where $\chi \in$ {saturated entropy (s∗), momentum (M), mass stream function(ψ)}. (b) Sources and sinks of entropy and angular momentum in the sub-cloud layer and free troposphere for the low-level pathway: surface fluxes of entropy, $F_s(z=0)$, and angular momentum, $F_M(z=0)$ (wavy arrows); dissipative heating, H; advection by the secondary circulation (gray arrow); convective entropy flux, $\overline{\acute{w}\acute{s}}$ (vertical block arrow); and eddy entropy flux, $\acute{u}\acute{s}$, through outer angular momentum surface in the free troposphere (horizontal block arrow) (from Tang, 2010)**

## 3. Data and methods

In the present work, two datasets have been used. The first dataset was from Joint Typhoon Warning Centers (JTWC) Best Track data of Japan Meteorology Agency and included eye location (latitude and longitude), maximum wind speed and its radius. The second dataset was taken from NCEP-GFS analysis data with $0.5^o \times 0.5^o$ horizontal resolution at 26 pressure levels with 6-h intervals. Temperature, humidity, pressure and mixing ratios data at various level heights have been extracted from NCEP-GFS analysis data to calculate entropy and its derivatives at surface, cloud base height and also through boundary layer. All data have been used during 3-11 November 2013. Entropy and its convective flux, have been computed at each grid points of all considered domains that will be described later. To this aim, we computed all values via our NCL (NCAR Command Language) scripts.

To assess dependency of the applied framework on (I) the size of the inner- and outer regions ($\alpha$) and also (II) the radius of decay of wind velocity from inner to outer regions ($\gamma$), 60 experiments have been run. List of $\alpha$ and $\gamma$ values have been shown in Table 1 for 60 experiments. In these experiments, the value of α varies from 1.2 to 3 (including 1.25, 1.3, 1.4, 1.5, 1.67, 1.75, 2, 2.3 and 3) and the γ value ranges from 0.3 to 0.9 (0.3, 0.5, 0.8 and 0.9). For this purpose, the size of the inner region differs from $1^o \times 1^o$ to $5^o \times 5^o$, while the size of the outer region changes from $2^o \times 2^o$ to $7^o \times 7^o$. It should be noted that these regions are different from TC inner- and outer-core, and have been defined randomly.

**Table 1 list of $\alpha$ and $\gamma$ values**

| Num. | size of the inner region ($x^\circ \times x^\circ$) | size of the outer region ($x^\circ \times x^\circ$) | calculated $\alpha$ | $\gamma$ |
|---|---|---|---|---|
| 1 | 1 | 2 | 2 | 0.3, 0.5, 0.8 and 0.9 |
| 2 | 1 | 3 | 3 | 0.3, 0.5, 0.8 and 0.9 |
| 3 | 2 | 3 | 1.5 | 0.3, 0.5, 0.8 and 0.9 |
| 4 | 2 | 4 | 2 | 0.3, 0.5, 0.8 and 0.9 |
| 5 | 2 | 5 | 2.5 | 0.3, 0.5, 0.8 and 0.9 |
| 6 | 2 | 6 | 3 | 0.3, 0.5, 0.8 and 0.9 |
| 7 | 3 | 4 | 1.33 | 0.3, 0.5, 0.8 and 0.9 |
| 8 | 3 | 5 | 1.67 | 0.3, 0.5, 0.8 and 0.9 |
| 9 | 3 | 6 | 2 | 0.3, 0.5, 0.8 and 0.9 |
| 10 | 3 | 7 | 2.33 | 0.3, 0.5, 0.8 and 0.9 |
| 11 | 4 | 5 | 1.25 | 0.3, 0.5, 0.8 and 0.9 |
| 12 | 4 | 6 | 1.5 | 0.3, 0.5, 0.8 and 0.9 |
| 13 | 4 | 7 | 1.75 | 0.3, 0.5, 0.8 and 0.9 |
| 14 | 5 | 6 | 1.2 | 0.3, 0.5, 0.8 and 0.9 |
| 15 | 5 | 7 | 1.4 | 0.3, 0.5, 0.8 and 0.9 |

Tropical cyclone Haiyan (TCH) with the extra-ordinary intensity of 170 kts (at 1800 UTC 7 November) intensified as the highest ever observed TCs globally and reached 35 kts well above the threshold of 135 kts as the existing highest value for category-5 (Lin et al., 2014). TCH devastated the southeast part of Asia, especially the Philippines Islands, and killed 6300 persons. TCH formed at 6°53′N/158°14′E on 2 November 2013, become a tropical storm on 4 November 2013, and reached the intensity of a typhoon on 5 November, based on saffir-simpson hurricane wind scale. TCH reached the maximum intensity at 12:00 UTC 7 November 2013, and after that entered the Philippines Islands. TCH continued northwesterly motion to the northern part of the Vietnam and dissipated on 11 November 2013. Some dynamic, thermodynamic and synoptic features of TCH have been studied by Pegahfar and Ghafarian (2017, 2104). Moreover, some of the upper and lower tropospheric meteorological parameters have been considered during TCH by Pegahfar and Ghafarian (2016). Shimada et al. (2018) examined the structure of TCH inner core. Wang et al. (2018) investigated the role of warm-core ocean eddy on TCH rapid intensification.

## 4. Results and discussion

To assess dependency of the applied framework on the size of the inner- and outer regions and also the radius of the maximum wind speed, 60 experiments have been run. Time series of (I) discrepancy of entropy between the inner- and outer regions, (II) three right terms of Eq. 7 and (III) $\overline{\acute{w}\acute{s}}$ values have been calculated for all experiments and analyzed. As an example, the results of two experiments have been plotted in Fig. 2. The inner regions of $1^o \times 1^o$ and $3^o \times 3^o$, the outer regions of $2^o \times 2^o$ and $6^o \times 6^o$, with $\gamma = 0.9$ have been plotted in Figure 2I and 2II, respectively.

In this figure, the time series of discrepancy of entropy between the inner- and outer regions ("a" panels in Fig. 2I and 2II), three right terms of Eq. 7 ("b", "c" and "d" panels in Fig. 2I and 2II) together with values of $\overline{\acute{w}\acute{s}}$ ("e" panels in Fig. 2I and 2II) have been presented. It can be realized that the first term has negative effect on $\overline{\acute{w}\acute{s}}$, while the second and third terms play positive influence. A remarkable point of Fig. 2 is the existence of two relative maximum values of $\overline{\acute{w}\acute{s}}$, one before 1800 UTC 07 November (TCH peak activity time, hereafter, TCHPAT) and the other after TCHPAT. Figure 2 indicates that the relatively maximum value of $\overline{\acute{w}\acute{s}}$ after TCHPAT did not occur at the same time using various experiments.

To analyze the results of all experiments, Figs. 3-5 have been prepared to demonstrate the minimum values of the first right-hand side term of Eq. 7 and maximum values of the second and third terms according to various $\alpha$ values in logarithmic scale, correspondingly. In Figs. 3-5, the results of selecting $\gamma = 0.9, 0.5$ and $0.3$ have been presented and each marker has been labeled by the size of the inner domain side.

(I)

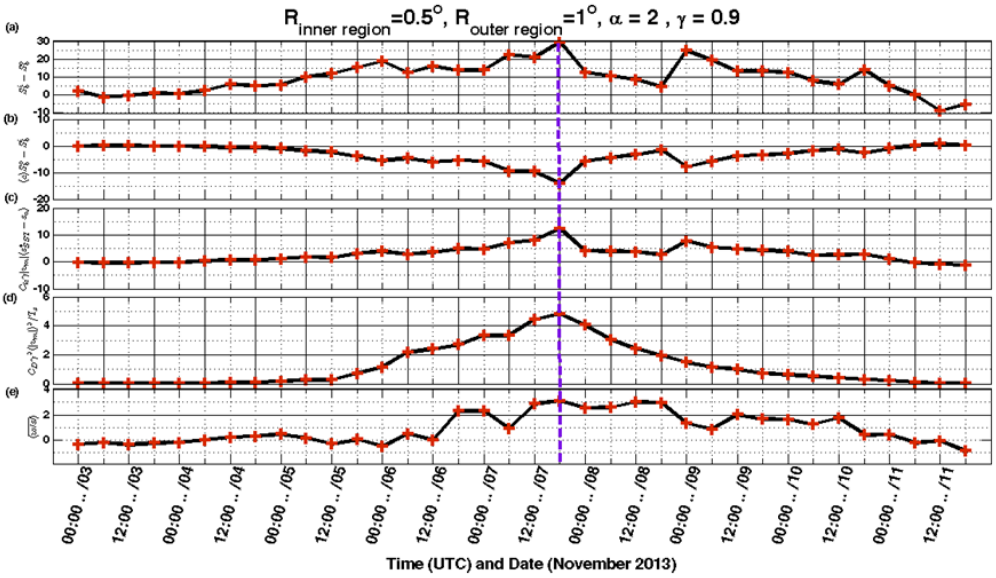


(II)

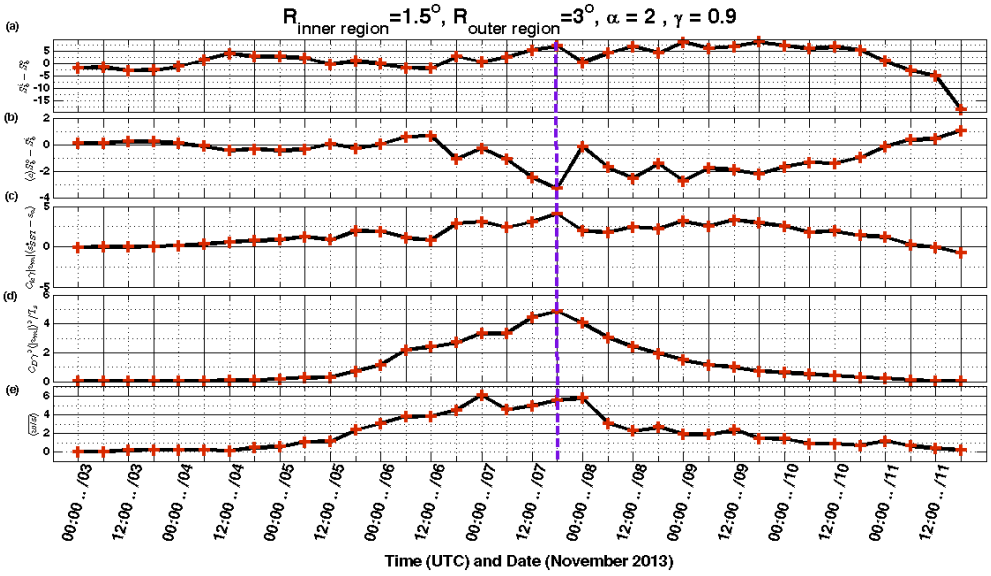


**Figure 2 Time series of discrepancy between entropy in inner and outer regions ($s_b^o - s_b^i$, (J/(kg K))) (a), three right terms of Eq. 7 (b, c, d) and also $\overline{w's'}$ (W/(K m$^2$))(d). The selected case include $1^o \times 1^o$ inner region, $2^o \times 2^o$ outer region (I subplot) and $3^o \times 3^o$ inner region, $6^o \times 6^o$ outer region (II subplot), both for $\gamma = 0.9$. The sign of "R" shows the radius of the regions. Inner- and outer regions have been demonstrated as subscribes of "R" signs.**

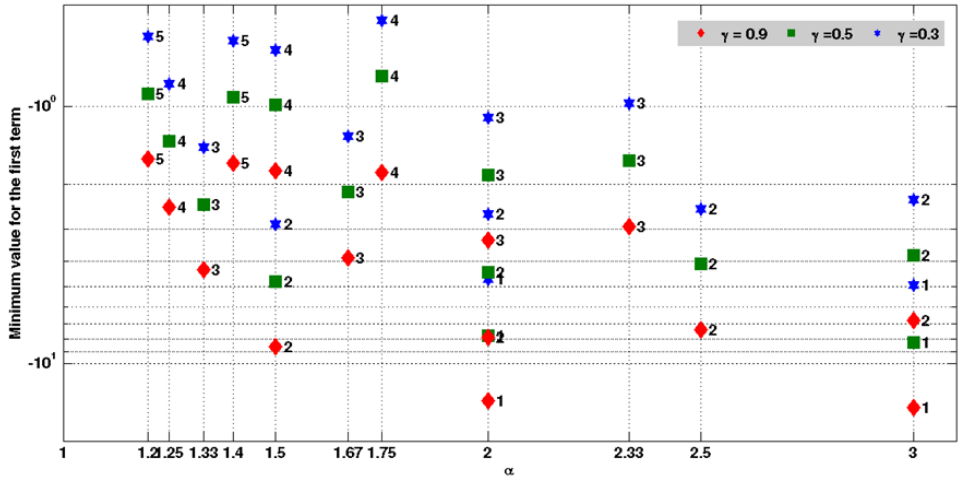


**Figure 3 Distribution of the minimum values of the first right-hand side term (W/(K m$^2$)) of Eq.7, according to the various values of α and γ, and different size for the inner and outer domains. The size of the inner domain side has been added to the right of each marker.**

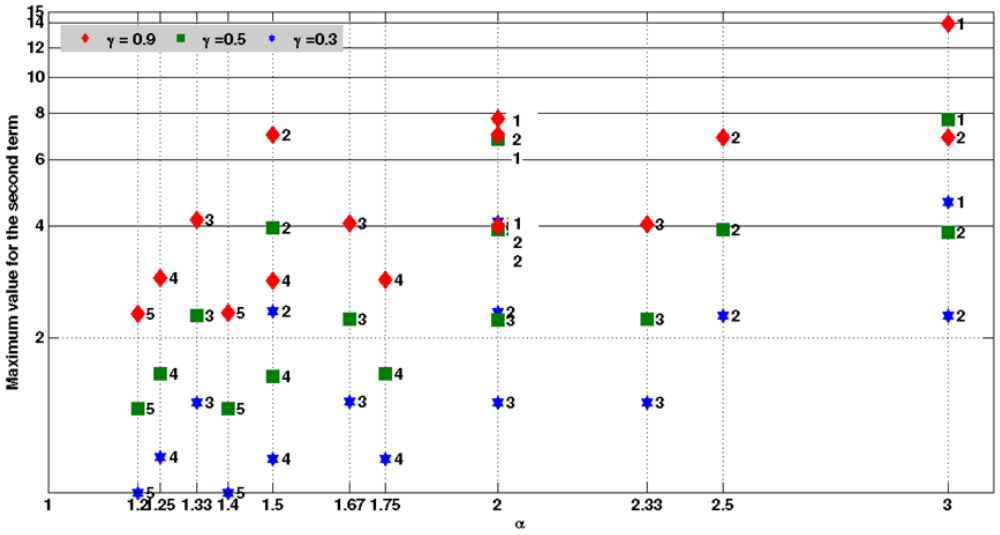


**Figure 4 Same as Fig. 3 but for the maximum values of the second right-hand side term ($W/(K\,m^2)$ ) of Eq.7.**

Figure 3 shows that the smaller inner regions produce the smaller values, and enlarging the inner region size decreases the role of the first term of Eq.7. Also greater γ values lead to larger extreme values of the first term of Eq.7.

Figure 4 demonstrates that increase of γ and α values increase the maximum value of the second term, while increase of the inner region size decreases the corresponding maximum value. It can be realized from Fig. 5 that only increase of γ value increases the maximum value of the third term, while increase of α value and inner region size has no effect. Here after results from the experiments with $\gamma = 0.9$ and $\gamma = 0.8$ will be presented, because of producing the largest absolute values.

As it can be seen from Fig. 2, time series of $\overline{\acute{w}\acute{s}}$ has two relative maximum values, before and after TCHPAT, respectively. For a comprehensive analysis, variation of these two values align with the value at the TCHPAT have been studied using various γ and α values. An overview of $\overline{\acute{w}\acute{s}}$ time series through 60 experiments indicates that the first relative maximum value of $\overline{\acute{w}\acute{s}}$ before TCHPAT occurred between 1800 UTC 6 November and 0000 UTC 7 November, while its second relative maximum value after TCHPAT happened between 0000 and 1200 UTC 8 November. The calculated values of $\overline{\acute{w}\acute{s}}$ for the first relative maximum value before and after TCHPAT together with the values at TCHPAT have been presented in Fig. 6. As this figure demonstrates, choosing $\gamma = 0.9$ and $\gamma = 0.8$ values produces close values of $\overline{\acute{w}\acute{s}}$ especially for the two relative maximum ones, however the first choice of $\gamma$ creates higher values. Changing $\alpha$ and $\gamma$ values leads to significant variation in $\overline{\acute{w}\acute{s}}$ value at TCHPAT and also for two relative maximum values. Also increase of the outer region sizes in experiments with the same inner region sizes rises the values of $\overline{\acute{w}\acute{s}}$.

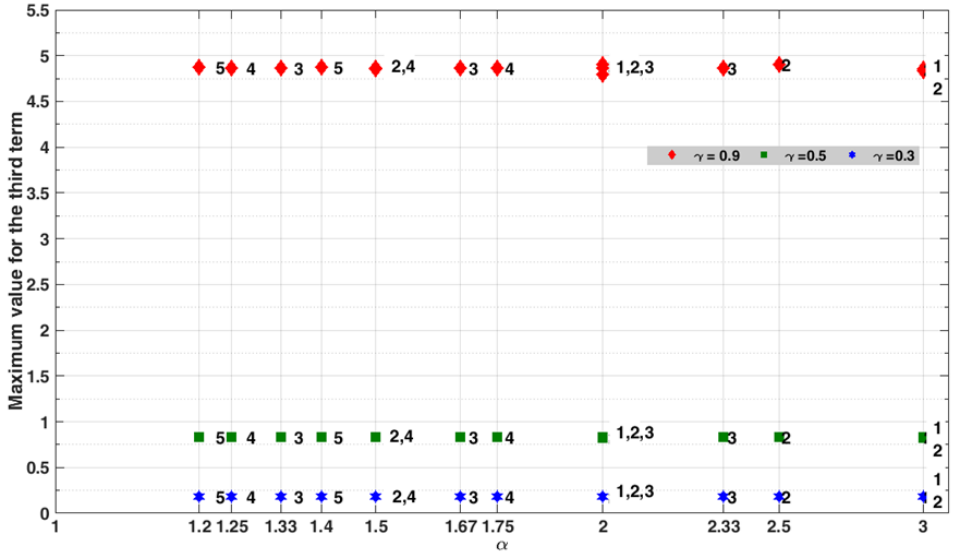


**Figure 5 Same as Fig. 3 but for the maximum values of the third right-hand side term ($W/(K\,m^2)$) of Eq.7.**

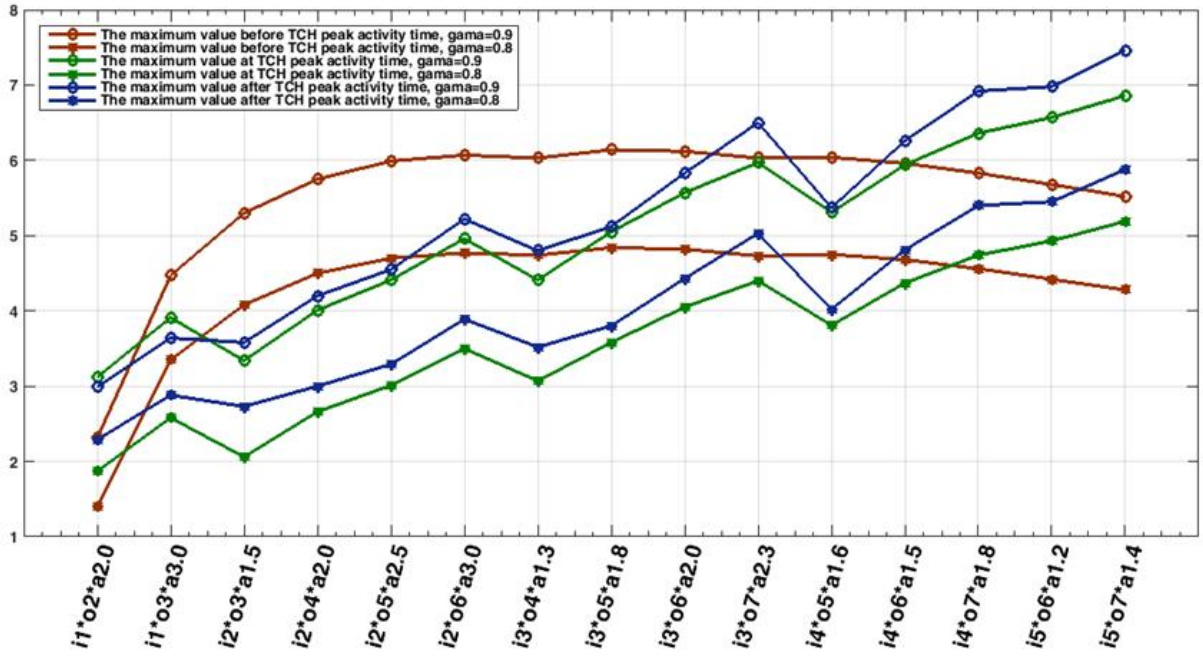


**Figure 6 the value of $\overline{\acute{w}\acute{s}}$ ($\mathrm{W}/(\mathrm{K\,m^2})$) at TCHPAT align with two relative maximum values of $\overline{\acute{w}\acute{s}}$ before and after TCHPAT, respectively. X-abscissa is labeled as "im*on*ap", where "im" denotes the size of inner region side, "on" shows the size of outer region side and "ap" is the α and its value. Values obtained using $\gamma = 0.9$ are denoted by circle and those from $\gamma = 0.8$ are signified by asterisks.**

Moreover, increase of the inner region sizes in the experiments with the same outer region sizes growths the values of $\overline{\acute{w}\acute{s}}$. Increase of $\alpha$ values, without any attention to the inner- and outer region sizes, leads to higher values of $\overline{\acute{w}\acute{s}}$. The first relative maximum value of $\overline{\acute{w}\acute{s}}$ shows relatively constant behavior for the inner domains larger than $2° \times 2°$ and the outer domains greater than $4° \times 4°$, while its value is sensitive to the inner domains smaller than $2° \times 2°$ and the outer domains smaller than $4° \times 4°$.

Variation of the two relative maximum values of $\overline{\acute{w}\acute{s}}$ (before and after TCHPAT) and the value at TCHPAT have been plotted in Fig. 7, based on the various inner – and outer domain sizes. Value of each bar has been added to the top of that. As before, two values of $\gamma = 0.9$ and $\gamma = 0.8$ have been plotted in this figure. As Fig. 7 shows, the inner regions greater than $1° \times 1°$ produce little variation in the first relative maximum value of $\overline{\acute{w}\acute{s}}$, around 5-6 for $\gamma = 0.9$ and 4 for $\gamma = 0.8$, while the experiments with inner region of $1° \times 1°$ lead to the smaller values at both values of $\gamma$.

To analysis dependency of the three special times in $\overline{\acute{w}\acute{s}}$ time series (before, after and at TCHPAT) on the inner and outer domain sizes and also on $\alpha$ and $\gamma$ values separately, Figs. 8-10 have been prepared.

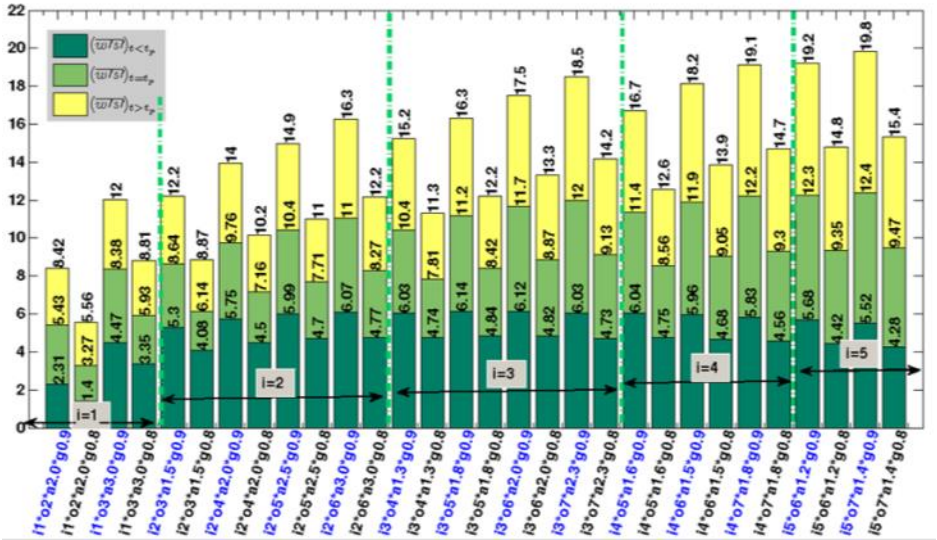


**Figure 7 the value of $\overline{\acute{w}\acute{s}}$ ($\mathrm{W}/(\mathrm{K\,m^2})$) is dark green before TCHPAT ($t < t_p$), light green at TCHPAT ($t_p$) and yellow after TCHPAT ($t > t_p$). The X- abscissa is labeled as "im*on*ap*gt", where "im" denotes the size of inner region side, "on" shows the size of outer region side, "ap" is the α and its value and "gt" refers $\gamma$ and its value.**

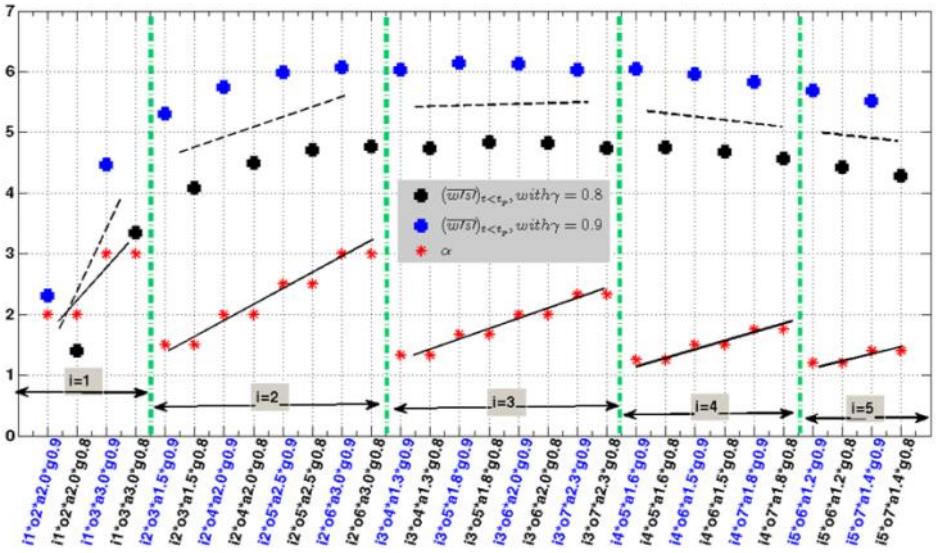


**Figure 8 values of $\overline{\acute{w}\acute{s}}$ ($\mathbf{W/(K\,m^2)}$) before TCHPAT ($t < t_p$, dark green) for two values of $\gamma = 0.9$ (blue plus) and $\gamma = 0.8$ (black plus). The X- abscissa is labeled as "im*on*ap*gt", where "im" denotes the size of inner region side, "on" shows the size of the outer region side, "ap" is the α and its value and "gt" shows the $\gamma$ and its value.**

Figure 8 shows relative maximum value of $\overline{\acute{w}\acute{s}}$ before TCHPAT for the experiments with $\gamma = 0.9$ and 0.8 and various inner- and outer domain sizes. Independency of the value of the first relative maximum value of $\overline{\acute{w}\acute{s}}$ on the inner- and outer domain sizes for the experiments with the inner domain greater than $2° \times 2°$ is evident. Changing inner domain size from $1° \times 1°$ to $2° \times 2°$ increases the first maximum value of $\overline{\acute{w}\acute{s}}$ significantly.

Figure 9 demonstrates that at TCHPAT, in the experiments with the same inner domain size and different outer domain size (various $\alpha$), increase of $\alpha$ value leads to greater value of $\overline{\acute{w}\acute{s}}$. In the experiments with the same value of $\alpha$, the larger inner domain produce larger $\overline{\acute{w}\acute{s}}$ values. The value of $\overline{\acute{w}\acute{s}}$ at TCHPAT is dependent on inner- and outer domain size and also $\alpha$ and $\gamma$ values. At TCHPAT, the smallest value of $\overline{\acute{w}\acute{s}}$ belongs to the experiments with smaller inner domain size ($i = 1$). Results from Figs 9 and 10 are similar.

## 5. Summary and conclusions

Forecasting the activity of severe TCs as significant natural hazards along with improving understand of their plausible impacts are an important task (Camargo et al. 2007). In the present work, a theoretical framework developed by Tang (2010) has been utilized. The source code of this axi-symmetric framework was not freely available and the authors developed that independently. There were two external parameters in this model that controlled the results. One of them was $\alpha$ parameter that shows the ratio of the outer domain size to the inner one. The other one was $\gamma$ parameter that expressed the wind

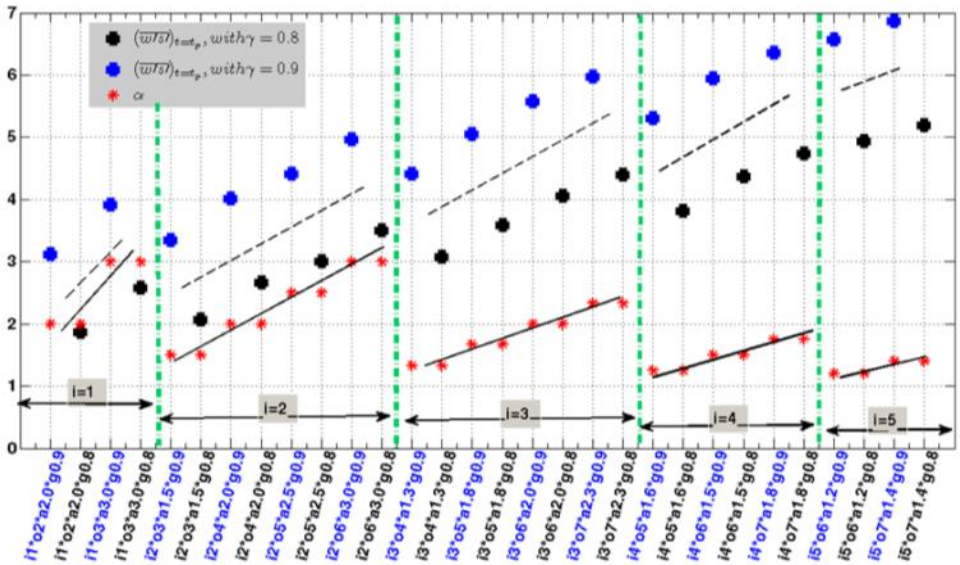


**Figure 9 values of $\overline{\acute{w}\acute{s}}$ ($\mathbf{W/(K\,m^2)}$) at TCHPAT ($t = t_p$, dark green) for two values of $\gamma = 0.9$ (blue plus) and $\gamma = 0.8$ (black plus). The X-abscissa is labeled as "im*on*ap*gt", where "im" denotes the size of inner region side, "on" shows the size of the outer region side, "ap" is the α and its value and "gt" shows the $\gamma$ and its value.**

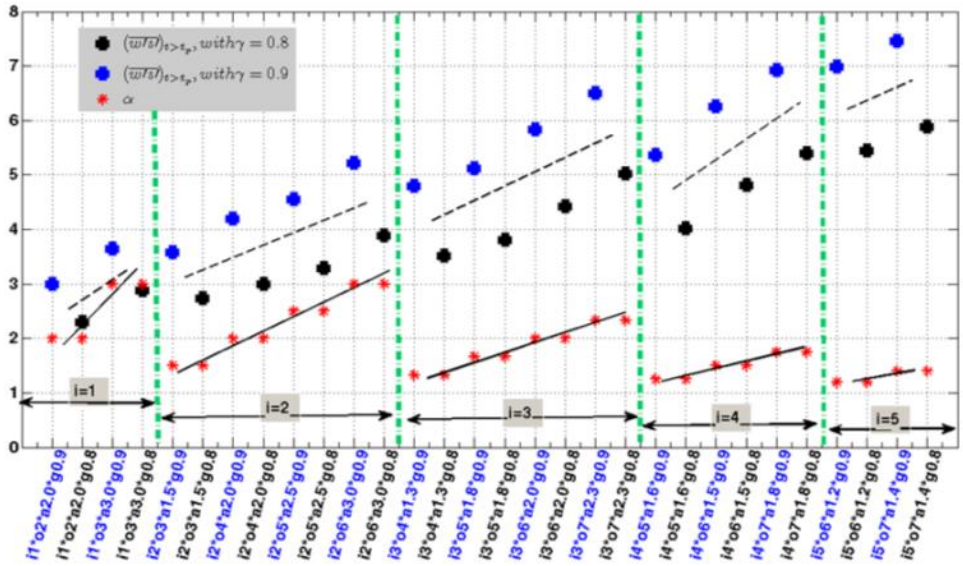


**Figure 10 values of $\overline{\dot{w}\dot{s}}$ ($\mathbf{W/(K\ m^2)}$) after the TCHPAT ($t > t_p$, dark green) for two values of $\gamma = 0.9$ (blue plus) and $\gamma = 0.8$ (black plus). The X- abscissa is labeled as "im*on*ap*gt", where "im" denotes the size of inner region side, "on" shows the size of outer region side, "ap" is the α and its value and "gt" shows the $\gamma$ and its value.**

speed as a fraction of maximum wind speed. To investigate the sensitivity of this model to these parameters, it was run for 60 different configurations. Various configurations were set using different $\alpha$ and $\gamma$ values and also inner- and outer domain sizes. The α value varied from 1.2 to 3 and γ value ranged from 0.3 to 0.9. Also the inner region size differed from $1^o \times 1^o$ to $5^o \times 5^o$, while the outer region changed from $2^o \times 2^o$ to $7^o \times 7^o$. Values of $\overline{\dot{w}\dot{s}}$ were calculated using Eq. 7 including three main terms.

The outputs were analyzed from the two different aspects categories as (I) three right-hand side terms of the applied main equation (Eq. 7) and (II) importance of two relative maximum values of $\overline{\dot{w}\dot{s}}$ before and after TCHPAT and also $\overline{\dot{w}\dot{s}}$ value at TCHPAT.

Investigation of the first aspect showed that the increasing of $\gamma$ value increased the importance of all terms. In addition, increase of the specific volume (α) led to the increase of the contributions of entropy discrepancy between the inner and outer regions at both cloud base height and surface (the first and second right-hand-side terms), while it had no effect on the maximum wind speed (the third right-hand-side term).

Analysis of two maximum values of the convective entropy flux before and after TCHPAT and that at the TCHPAT revealed that the effects of variation of $\alpha$ and $\gamma$ values and also change of the inner- and outer domain sizes at these three considered times were not the same. The inner domain size smaller than $2° \times 2°$ and the outer domain size smaller than $4° \times 4°$ produced noticeable variations for the corresponding values before TCHPAT, while the larger inner- and outer domain sizes didn't affect the results importantly. Values of vertical entropy flux at TCHPAT and also its maximum value after TCHPAT are sensitive to $\alpha$ and $\gamma$ values and also the inner- and outer domain sizes. A thorough evaluation showed that both enlarge of the inner domain size along with the constant outer domain size, and extend of the outer domain size with constant inner domain size led to the increase of the convective entropy flux.

Overall, findings of this research showed that configuration of the model (including the two external parameters and domains' size) affected the convective entropy flux outputs during the TCH from two different aspects. Since a TC experiences various extensions and intensities during its lifetime, reaching a comprehensive conclusion to define an optimized configuration needs data with higher horizontal grid resolution and also more TCs for test. The authors are implementing this subject based on downscaling approach.

## Acknowledgement

This work was funded by the Iranian National Institute for Oceanography and Atmospheric Science (project No. 393-033-02). The authors would like to thank NCEP-GFS teams for providing analysis data and also JTWC for TCH track data.

## 6. References

1- Bister, M., & Emanuel, K., (1998), *Dissipative heating and hurricane intensity*, Meteorology Atmospheric Physics, 65, 233–240.

2- Bruyère, C. L., Holland, G. J., & Towler, E., (2012), *investigating the use of a genesis potential index for tropical cyclones in the North Atlantic basin*, Journal of Climate, 2524, 8611-8626.

3- Bryan, G. H., (2008), *On the computation of pseudoadiabatic entropy and equivalent potential temperature*, Mon. Wea. Rev., 13612:5239-5245.

4- Bryan, G., & Rotunno, R., (2009), *The maximum intensity of tropical cyclones in axisymmetric numerical model simulations*, Mon. Wea. Rev., 137, 1770–1789.

5- Camargo, S. J., A. H. Sobel, A. G. Barnston, and K. A. Emanuel, (2007b), *Tropical cyclone genesis potential index in climate models*. Tellus, 59A, 428–443.

6- Davis, C., & Bosart, L., (2006), *The formation of Hurricane Humberto 2001: The importance of extratropical precursors*, Quart. J. Roy. Meteor. Soc., 132, 2055–2085.

7- DeMaria, M., Knaff, J., & Connell, B., (2001*), A tropical cyclone genesis parameter for the tropical Atlantic*, Wea. Forecasting, 16, 219–233.

8- Chen, X., Wang, Y., Fang, J., & Xue, M., (2018), *A Numerical Study on Rapid Intensification of Typhoon Vicente (2012) in the South China Sea. Part II: Roles of Inner-Core Processes*, Journal of the Atmospheric Sciences, 75(1), 235-255.

9- Emanuel, K. A., (1986), *An air–sea interaction theory for tropical cyclones. Part I: Steadystate maintenance*, J. Atmos. Sci., 43, 585–604.

10- Emanuel, K. A., (1991), *The theory of hurricanes*, Annual Review of Fluid Mechanics, 231, 179-196.

11- Emanuel, K. A., (1995), *Sensitivity of tropical cyclones to surface exchange coefficients and a revised steady-state model incorporating eye dynamics*, J. Atmos. Sci., 52, 3969– 3976.

12- Emanuel, K., & Nolan, V., (2004), *Tropical cyclone activity and the global climate system. Preprints*, 26th Conf. on Hurricanes and Tropical Meteorology, Miami, FL, Amer. Meteor. Soc., 240–241.

13- Emanuel, K., DesAutels, C., Holloway, C., & Korty, R., (2004), *Environmental control of tropical cyclone intensity*, J. Atmos. Sci., 617, 843-858.

14- Emanuel, K., Sundararajan R., & Williams J., (2008), *Hurricanes and global warming - results from downscaling IPCC AR4 simulations*, Bull. Amer. Meteor. Soc., 89, 347–367.

15- Frank, W. M., & Ritchie, E. A., (2001), *Effects of vertical wind shear on the intensity and structure of numerically simulated hurricanes*, Mon. Wea. Rev., 129, 2249–2269.

16- Jones, S., (1995), *The evolution of vortices in vertical shear. I: Initially barotropic vortices*, Quart. J. Roy. Meteor. Soc., 121, 821–851.

17- Kleinschmidt E., (1951), *Grundlagen einer theorie der tropischen zyklonen*, Arch. Meteor. Geophys. Bioklimatol., 4A, 53–72.

18- Lee, C. S., Cheung, K. K., W., Fang, W. T., Elsberry, R. L., (2010), *Initial maintainance of tropical cyclone size in the western North Pacific*, Mon. Wea. Rev., 138(8), 3207-3223.

19- Lin, I. I., Pun, I. F., & Lien, C. C., (2014), *"Category-6" supertyphoon Haiyan in global warming hiatus: Contribution from subsurface ocean warming*, Geophysical Research Letters, 41(23), 8547-8553.

20- Lin, N., Jing, R., Wang, Y., Yonekura, E., Fan, J., & Xue, L. (2017), *A statistical investigation of the dependence of tropical cyclone intensity change on the surrounding environment*, Mon. Wea. Rev., 145, 2813–2831

21- Marin, J., Raymond, D., & Raga, G., (2009), *Intensification of tropical cyclones in the GFS model*, Atmos. Chem. Phys., 9, 1407–1417.

22- McBride, J., & Zehr, R., (1981), *Observational analysis of tropical cyclone formation. Part II: Comparison of non-developing versus developing systems*, J. Atmos. Sci., 38, 1132–1151.

23- Montgomery, M. T., & Smith, RK., (2014), *Paradigms for tropical cyclone intensification*, naval postgraduate school Monterey ca dept. of meteorology.

24- Nolan, D., & Rappin, E., (2008), *Increased sensitivity of tropical cyclogenesis to wind shear in higher SST environments*, Geophys. Res. Lett., 35, L14805, doi: 10.1029/2008GL034147.

25- Nolan, D., & McGauley, M., (2012), *Tropical cyclogenesis in wind shear: Climatological relationships and physical processes*, Cyclones: Formation, Triggers, and Control, 1-36.

26- Nolan, D., (2007), *What is the trigger for tropical cyclogenesis?*, Aust. Meteor. Mag., 56, 241–266.

27- Pegahfar, N., & Ghafarian, P., (2014), *Analysis of two dynamic parameters of CAPE and Helicity for Haiyan Tropical Cyclone*, International ICOPMAS Conference, Tehran, Iran.

28- Pegahfar, N., & Ghafarian, P., (2016), *Investigation of meteorological parameters in the lower and upper troposphere during tropical cyclone Haiyan*, Journal of Oceanography 726:55-67.

29- Pegahfar, N., & Ghafarian, P., (2017), *Dynamic and Thermodynamic Analysis of Tropical Cyclone Haiyan*, Journal of Space and Earth Physics, 424, 13-26.

30- Pielke, Jr. R., Gratz, J., Landsea, C., Collins, D., Saunders, M., & Musulin, R., (2008), *Normalized hurricane damages in the United States: 1900-2005*. Natural Hazards Rev., 9, 29–42.

31- Riehl, H., (1951), *A model for hurricane formation*, J. Appl. Phys., Vol. 21, 917–925.

32- Schenkel, B. A., Lin, N., Chavas, D., Vecchi, G. A., Oppenheimer, M., & Brammer, A., (2018), *Lifetime Evolution of Outer Tropical Cyclone Size and Structure as Diagnosed from Reanalysis and Climate Model Data*, Journal of Climate, 31(19), 7985-8004.

33- Shimada, U., Kubota, H., Yamada, H., Cayanan, E. O., & Hilario, F. D., (2018), *Intensity and Inner-Core Structure of Typhoon Haiyan (2013) near Landfall: Doppler Radar Analysis*, Monthly Weather Review, 146(2), 583-597.

34- Smith, R., Ulrich, W., & Sneddon, G., (2000), *On the dynamics of hurricane-like vortices in vertical-shear flows: Quart*, J. Roy. Meteor. Soc., 126, 2653–2670.

35- Tang, B., & Camargo, S. J., (2014), *Environmental control of tropical cyclones in CMIP5: A ventilation perspective*, Journal of Advances in Modeling Earth Systems, 61, 115-128.

36- Tang, B., & Emanuel, K., (2010), *Midlevel ventilation's constraint on tropical cyclone intensity*, J. Atmos. Sci., 67, 1817–1830.

37- Tang, B. H. A., (2010), *Midlevel ventilation's constraint on tropical cyclone intensity*, Doctoral Thesis, Massachusetts Institute of Technology.

38- Tory, K., Davidson, N., & Montgomery, M., (2007), *Prediction and diagnosis of tropical cyclone formation in an NWP system. Part III: Diagnosis of developing and nondeveloping storms*, J. Atmos. Sci., 64, 3195–3213.

39- Vickery, P.J., F.J. Masters, M.D. Powell and D. Wadhera, (2009), *Hurricane hazard modelling: the past, present and future*, Journal of Wind Engineering and Industrial Aerodynamics, 97, 392-405.

40- Wang, Y., (2012), *Recent research progress on tropical cyclone structure and intensity*, Trop. Cyclone Res. Rev, 1, 254-275.

41- Wang, G., Zhao, B., Qiao, F., & Zhao, C., (2018), *Rapid intensification of Super Typhoon Haiyan: the important role of a warm-core ocean eddy*, Ocean Dynamics, 68(12), 1649-1661.

42- Wong, M. & Chan, J., (2004), *Tropical cyclone intensity in vertical wind shear*, J. Atmos. Sci., 61, 1859–1876.

43- Zehr, R., (1992), *Tropical cyclogenesis in the western north Pacif ic*, NOAA Tech. Rep. NESDIS 61, 181 pp.

INTERNATIONAL JOURNAL OF
COASTAL & OFFSHORE ENGINEERING IJCOE Vol.3/No. 3/Autumn 2018 (53-62)

Available online at: http://ijcoe.org/browse.php?a_code=A-10-224-1&sid=1&slc_lang=en

# Wave Climate Variability and Longshore Sediment Transport Evaluation along Ramin Harbor, Southeast Coast of Iran

**Ehsan Isaie Moghaddam[1*], Habib Hakimzadeh[2]**

[1*] *MSc, Faculty of Civil Engineering, Sahand University of Technology; e_isaie@sut.ac.ir*
[2] *Professor, Faculty of Civil Engineering, Sahand University of Technology; hakimzadeh@sut.ac.ir*

## ARTICLE INFO

*Article History:*
Received: 26 Apr. 2018
Accepted: 26 Nov. 2018

*Keywords:*
Longshore Sediment Transport
Wave Climate
Seasonal Variations
Ramin Harbor
Monsoon Season
Kamphuis Formula

## ABSTRACT

This paper examines the variation of wave characteristics and net Longshore Sediment Transport (LST) rates along the Ramin Harbor, southeast coast of Iran. Potential LST rates were determined based on three empirical relationships, namely, CERC, Kamphuis and Komar and using transformed hindcast offshore waves from 1985 to 2006. Detailed analysis of 22-year deep water wave information for the region indicates considerable seasonal variations for the wave conditions, with high energy monsoon waves being generated in Indian Ocean and Arabian Sea from southern direction during monsoon season. Moreover, the long period swell waves originated from Indian Ocean usually approach the coast from southeast to south. Further, the variable sea waves characterized by shorter-period, normally spreading from west to southwest, are superimposed on the basis swell during non-monsoon season. In order to assess the reliability and accuracy of the predicted magnitudes for LST rates, the achieved results were compared with the field data, with the Kamphuis equation being found to give acceptable estimation for the potential LST rate. Finally, through morphological analyze of the adjacent shorelines and coastal region, a reasonable agreement was established for the LST direction.

## 1. Introduction

A proper knowledge of sediment transport processes along beaches is of significant importance for engineers in coastal planning facilities. Assessment of the sediment transport rate and its predominant direction are known as important data in designing of shore protection measures. Also, it has been known that among different coastal processes and parameters, Longshore Sediment Transport (LST) is the most important parameter that controls the sediment dynamics and diverse morphological changes (Güner, Yüksel, and Çevik, 2013). It also provides an integral part of the input required for determination of dredging requirements at a port entrance (Schoonees, 2000). Furthermore, it is generally accepted that wave action is the primary source of energy available at a coastline compared to the other oceanographic parameters such as winds, tides and ocean currents for moving sediments (Prasad and Reddy, 1988). Breaking of waves as they approach to the nearshore zone is primarily associated with large amount of wave energy losses and producing the longshore currents which transport significant amount of sediments along the coast (Kunte and Wagle, 1993).

The contribution of different terms to the magnitude of the LST rate has been investigated by a number of researchers over the last decades (e.g., Camenen and Larroudé, 2003; Chempalayil et al., 2014; King, 2005; Larangeiro and Oliveira, 2003; Shanas and Sanil Kumar, 2014; Smith, Wang, Ebersole, and Zhang, 2009). It is also possible to calculate the transport rate utilizing various formulas and methods (Mafi, Yeganeh-Bakhtiary, and Kazeminezhad, 2013). Because of the complexity of the nearshore processes, numerical schemes are known to be the best tool available to describe the mechanisms governing coastal processes. But due to the extreme difficulty of acquiring extensive data over a complicated coastal topography and relatively high cost in conjunction with measurement processes, a commonly used approach is to estimate LST rate through empirical bulk formulations. Most of the LST empirical relationships suggested by researchers were extended based on laboratory data and can only be reliable for a specific circumstance. Thus, it was known that for a proper evaluation of the LST in a coastline which is subjected to various wave conditions, examination of the underlying processes and elements responsible for the

changes would be necessary (Sheela Nair, Sundar, and Kurian, 2015).

The present paper aims to investigate the long-term wave climatology of the Ramin Harbor using 22 years hindcasted wave data provided by the Iranian Ports and Maritime Organization (PMO). Seasonal to decadal variability of the LST is estimated based on empirical formulas over the period of 1985-2006. Morphological landforms and dredging statistics are used to evaluate the reliability of potential sediment transport rate along the study area. In addition, LST direction is determined through the calculations and littoral environmental observations.

## 2. Study area

### 2.1. Geomorphology

The study area in this research is Ramin fishery harbor, located in southeast of Iran, along the north coast of Oman Sea at 60.745° E longitude and 25.268°N latitude (Figure 1). The harbor layout is such that its basin's mouth is located in front of a broken coastline and the navigations through the harbor entrance are subjected to a considerable sedimentation problem due to uncontrollable sediment drift towards the harbor entrance. Consequently, the water depth at the entrance and inside the basin decreases continuously. The harbor lies in a relatively straight coastline between Beris Headland and Chabahar Bay. This section faces the Arabian Sea and the Indian Ocean and the coastline has an extension of 60 km with more or less a WNW-ESE general orientation. The bottom contours align approximately parallel to the general trend of the shoreline. The area is mainly occupied by a series of cliffs and rocky landforms both on the eastern and western side, and short stretches of sandy beaches are located to the east of the harbor and the seasonal Lipar River at a distance of 8 km east of the harbor which is blocked by sand bar. Measurements of particle size distribution at a number of locations around the basin revealed that the bottom sediment size varies along the study area from fine sand to medium sand (with a median grain size of about 0.15 mm to 0.35 mm). Also, a bathymetric survey of the near-shore zone of the Ramin Harbor indicated that the beach and near-shore profiles are characterized by a relatively steep beach slope (The overall slope in the surf-zone was found to be in the order of about 0.05).

### 2.2. Winds

The Arabian Sea and the Gulf of Oman are subject to two distinct seasons separated by two short (30 to 45 days) transition periods. During December through March the winds blow predominantly from the northeast and during June through September they blow from the southwest. April and May; October and November are typically the spring and fall transition, respectively. From the standpoint of wave generation,

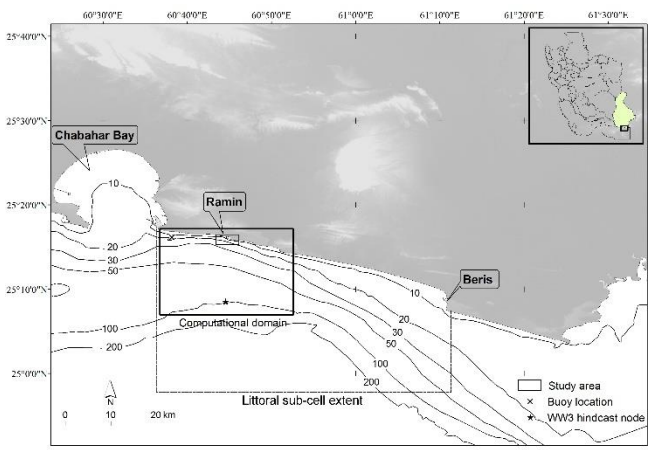


**Figure 1. Location map with the position of observed and modeled waves and the extent of the regional and the nested type of unstructured grids used for nearshore wave transformation**

northeast monsoon winds have no effect on the Oman Sea coast of Iran and particularly the Ramin Harbor, while southwesterly flow directly influences the study region coast (Walters and Sjoberg, 1988).

### 2.3. Hydrodynamics

This seasonal cycle of winds leads to a cycle in wave climate of the southeast coast of Iran, both over the open sea and over coastal areas. Hence, the study area is strongly influenced by high energy monsoon-induced waves being generated in the Indian Ocean and Arabian Sea from the southern direction during monsoon season (i.e., June to September). Furthermore, the coast is exposed to long period swell waves originating from the Indian Ocean and approaching from the sector between southeast to southern directions as well as generally the less-energetic sea waves which are propagating from west to southwest and being generated close to the shore by local Oman Sea winds, superimposed on the basis swell during non-monsoon season (i.e., October to May) (Figure 2) (Dibajnia, Kebriaee, and Allahyar, 2008).

Tides in the study area are mixed semi-diurnal dominant with a mean tidal range of 2.5 m and hence, the beach is categorized as a meso-tidal beach (Short, 1991). In meso-tidal condition, waves as well as tidal currents are important. However, in coastal regions where high energy waves are most dominant upon the shore planform, tidal influences usually become negligible (Short and Hesp, 1982). despite the low energy wave climates that exist in the study region during non-monsoon period, the high energy waves become predominant in the monsoon season.

## 3. Data and Methodology

Recent advancements in wave hindcast modeling provided the computation of extended, high-quality, continuous-wave time series, improving the information of the long-term wave climatology along the Iranian coasts.

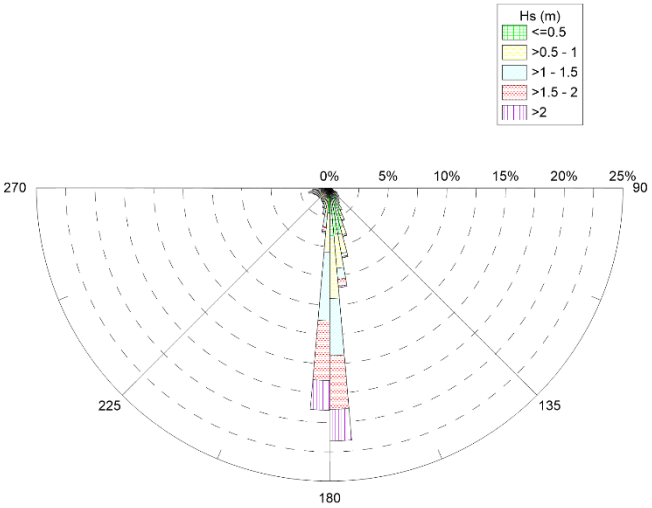


**Figure 2. Long-term wave statistics of Ramin deep water location during the years between 1985 and 2006 (WW3 hindcast node)**

Monitoring and Modeling Studies of Iranian Coasts is a multi-year study to determine wave climate on the Oman Sea and the Persian Gulf coastline of Iran and is based on numerical hindcast data provided by Iranian PMO. PMO hindcast wave estimates were compiled in intermediate to deep water depths with third-generation spectral wave model WAVEWATCH III (Tolman, 2009), and the achieved model results were found in excellent agreements with the measurements made at various buoy locations and satellite altimeter data (Dibajnia et al., 2008).

### 3.1. Wave Propagation Model Description

The wave conditions applied in the present study obtained from the aforementioned project at node 60.75° E and 25.125° N that extend from January 1985 to December 2006 with a 3-h interval. In order to assess the wave conditions in the near-shore and coastal zones which most often involves transformation of the known offshore wave statistics, MIKE 21 Spectral Wave model (MIKE 21 SW) was used. The model is based on flexible mesh and therefore particularly applicable for simultaneous wave analysis both in regional and local scales. In MIKE 21 SW model, the governing equation is based on the wave action conservation formulation given as:

$$\frac{\partial N}{\partial t} + \frac{\partial C_x N}{\partial x} + \frac{\partial C_y N}{\partial y} + \frac{\partial C_\sigma N}{\partial \sigma} + \frac{\partial C_\theta N}{\partial \theta} = \frac{S}{\sigma} \qquad (1)$$

The left-hand side of this equation describes the wave spectral energy propagation in space and time and the right-hand side term contains the superposition of source functions describing various physical phenomena. The parameters in this equation are: N = the action density spectrum, which is equal to energy density spectrum divided by the relative angular frequency, σ = wave relative angular frequency, θ = wave direction, $C_x$, $C_y$, $C_\sigma$ and $C_\theta$ is the propagation velocity of a wave group in the four-dimensional phase space $\vec{x}$ (x,y), σ and θ respectively, and S = the source term for the energy balance equation. The model is used for both offshore and nearshore wave modeling as it includes two different formulations: (a) directional decoupled parametric formulation and (b) fully spectral formulation (DHI Manual, 2014). In this study, the spectral formulation and time formulation of wave model have been selected as directionally decoupled parametric formulation and quasi-stationary, respectively. The regional modeled domain extends from Ramin coast to the WW3 simulation point in the N/S direction and from east of Chabahar Bay to a midway between the Chabahar and Beris fishery port in the W/E direction. Also, the local modeled domain extends 4.2 km along the shoreline and about 2 km across the shoreline and toward the open sea where water depth is about 25 m (Figure 1). The model has been run over unstructured grids in which a coarse mesh is used for the regional scale section of the computational domain with a high-resolution mesh describing the shallow water environment at the coastline. The grids' data were achieved through interpolation of bathymetric data resulting from a compilation of the near-shore survey data with a digitized nautical hydrographic chart. Grid generation and bathymetry interpolation were accomplished by Mesh Generator, a pre-processing module of the MIKE model. The relevant size of triangle mesh varies from 1000 m to 80 m for the regional model, and varies from 100 m to 20 m for the local high-resolution model. Wave estimates derived from the WW3 hindcast of Iranian PMO at the node (60.75° E, 25.125° N; Figure 1) act as the boundary conditions along the offshore model boundary for the local wave simulation. The formulation of wave breaking derived by Battjes and Janssen (1978) is used, where α = 1 and γ = 0.85. The Nikuradse roughness coefficient is used for the dissipation due to wave-bottom friction with a physical roughness of $K_N$ = 0.065 m.

**Table 1. Statistical results of model/measure comparison at buoy location**

| Wave parameters | Bias | RMSE | Scatter index (%) | Correlation | Number of observation |
|---|---|---|---|---|---|
| Significant wave height (m) | 0.07 | 0.27 | 33 | 0.87 | 142 |
| Wave period (sec) | -0.11 | 0.57 | 18 | 0.78 | |
| Mean wave direction (deg) | -0.59 | 13.06 | 11 | N.A. | |

For this particular study, since the model was only deployed for transformation of offshore wave statistics,

all wind-wave generation components (white-capping and quadruplet-wave interactions) were excluded.

In order to validate the model output parameters, a comparison is made between numerical model results against measured data at the Chabahar buoy location. The recorded data were collected at 3 h intervals using a Datawell Directional Waverider buoy near the Chabahar Bay (60.65° E and 25.267° N) from May 1998 to September 2000 discontinuously, which is deployed at 17 m water depth (Figure 1). The results, depicted in Figure 3 and Table 1, exhibit a relatively good agreement between the numerical model results and measured data. Moreover, in order to reduce running time, simulations were carried out using the annual representative wave bands for each year from 1992 to 2006 as the offshore forcing. Wave outputs were extracted along a cross-shore profile that extends from shoreline to approximately 20 m below LAT on the updrift side of the harbor (east side). Breaking wave characteristics were obtained at the point where the breaking criteria ($H_s/d_b$=0.78; CERC, 1984) was satisfied. These parameters were then used as the inputs for the following selected transport formulas. The instantaneous potential LST rate calculated for each wave band was converted into the annual transport considering the annual percent occurrence of each band.

### 3.2. Longshore Sediment Transport Formulas

Estimation of LST rates were computed using three different bulk formulations proposed by CERC (1984), Kamphuis (1991) and Komar (1998). Empirical formulas which have been used to predict potential LST rate, derived from extensive field measurements and laboratory investments and considering different parameters in formulations result in different predicts of LST value.

#### 3.2.1. CERC formula (1984)

One of the most widely used relationships for computing LST rate is the CERC (1984) formula, which assumes proportionality between the volume of transported sediments and the longshore energy flux. The CERC formula is defined by:

$$Q = \frac{K}{(\rho_s-\rho_w)(1-n)g}\frac{\rho_w g}{16}H_{sb}{}^2 C_{gb}\sin(2\alpha_b) \qquad (2)$$

Where $Q$ represents the LST rate in volume per unit time, $K$ is a dimensionless empirical proportionality coefficient and was taken as 0.39, $\rho_w$ is the density of saltwater, $\rho_s$ is the sediment density, $g$ is the gravity acceleration, $n$ is the porosity of sediments, $H_{sb}$ is the significant breaking wave height, $C_{gb}$ is the wave group celerity at the breaker line and $\alpha_b$ is the wave breaking angle.

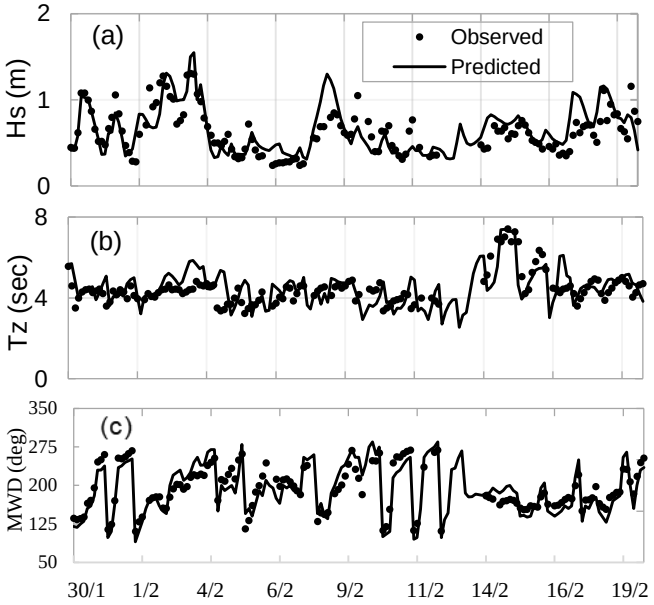


**Figure 3. Time series plots of modeled and measured wave parameters at Chabahar buoy from Jan. 30, 2000 to Feb. 20, 2000: (a) significant wave height, (b) mean wave period, (c) mean wave direction**

#### 3.2.2. Kamphuis (1991)

Kamphuis (1991) also presented an equation based on dimensional analysis which is a function of combination of all the important terms influence on wave breaking and sediment movements:

$$Q = \frac{2.27 H_{sb}{}^2 T_p{}^{1.5} m_b{}^{0.75} D_{50}{}^{-0.25}\sin^{0.6}(2\alpha_b)}{(\rho_s-\rho_w)(1-n)} \qquad (3)$$

In which $T_p$= peak wave period, $m_b$= the beach slope in the surf zone and $D_{50}$= sediment median grain size.

#### 3.2.3. Komar (1998)

Using breaker height and breaker angle, Komar (1998) proposed the following relationship:

$$Q = 0.46\rho_w g^{\frac{3}{2}} H_b{}^{\frac{5}{2}}\sin(\alpha_b)\cos(\alpha_b) \qquad (4)$$

For the present study, the aforementioned equations are compared with each other and validated against the net LST rate estimated based on the observed shoreline evolution pattern, dredging records and geomorphological features to determine the reliability of the figures of LST formulae for the study area.

## 4. Results

### 4.1. Wave Climate

The long-term variations in offshore wave climate were studied based on computing of mean annual wave data. Table 2 shows that mean annual significant wave height ($H_s$) varies from 0.27 m to 1.65 m with an average value of 0.82 m. The mean annual wave period ($T_z$) also varies between 3.6 sec and 12.3 sec, with an average magnitude of 6.85 sec. The coasts of Ramin are exposed to waves propagating annually from the sector

119° to 244°, with the average value of nearly 178° (Table 2).

**Table 2. Long-term mean annual wave characteristics between 1985 and 2006**

| Wave parameters | Min. | Max. | Average | Standard deviation |
|---|---|---|---|---|
| Significant wave height (m) | 0.27 | 1.65 | 0.82 | 0.09 |
| Wave period (sec) | 3.6 | 12.3 | 6.85 | 0.32 |
| Mean wave direction (deg) | 119 | 224 | 178.4 | 2.48 |

To assess the seasonal variations of the deep water wave climate for the region, monthly-based analysis of wave parameters was carried out. During the non-monsoon season, monthly average $H_s$ ranges from 0.2 m to 1.13 m with the average of 0.48 m (nearly 95% of waves are with height less than 1 m) (Figure 4).

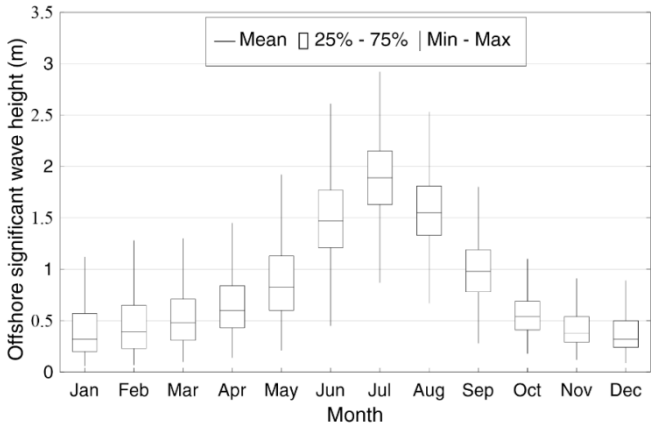


**Figure 4. Monthly average of the offshore significant wave height for the 22 years of wave hindcast at WW3 hindcast node**

End of pre-monsoon period is characterized by transition of low energy wind waves to high energy swell waves. Compare to other seasons, wave heights exhibit higher values during monsoon conditions and are observed within the range of 0.78 m to 2.15 m, with an average value of 1.5 m (88% of waves are greater than 1 m). Maximum $H_s$ is experienced in July. The monthly average $T_z$ during January to May varies from 4.2 sec to 8 sec. However, maximum $T_z$ is observed in October and November (Figure 5).

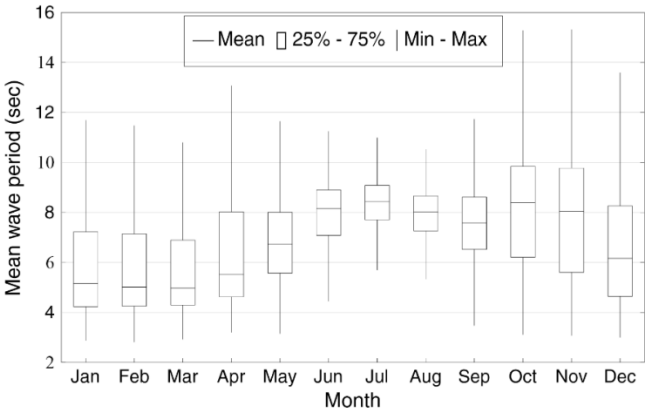


**Figure 5. Monthly average of the mean wave period for the 22 years of wave hindcast at WW3 hincast node**

The monsoon season is considerably less variable than the other seasons for the wave period and it mostly persisted between 6.5 sec and 9.1 sec with an average value of 8.05 sec. In addition, waves propagate over a very narrow directional band from the south section (Figure 6).

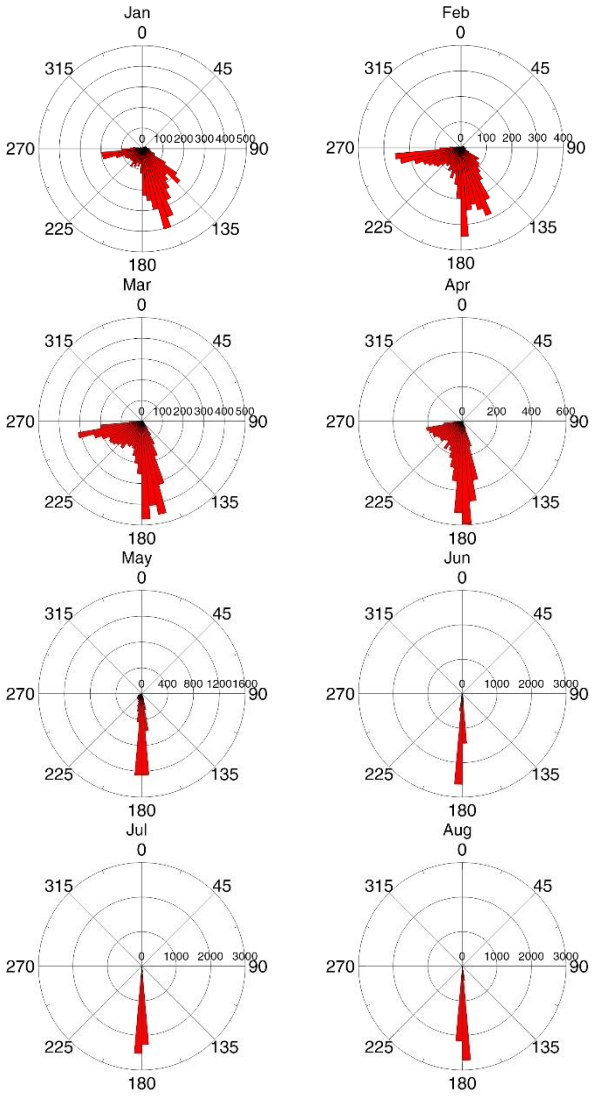

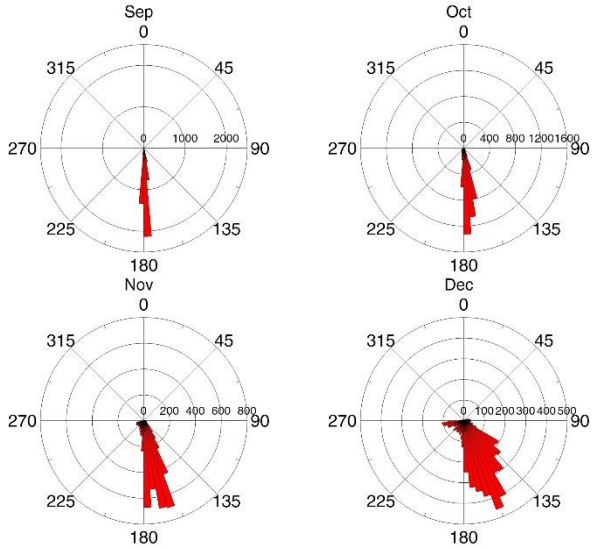


**Figure 6. Rose diagram of monthly average of mean offshore wave direction for the 22 years of wave hindcast at WW3 hindcast node**

About 10% of waves reach the coast from ESE to SSE, 70% of waves are between SSE and SSW and less than 20% of them approach from the sector between SSW and WSW. Further, with the onset of monsoon, long period swell waves propagating from south become predominant. Overall, the wave climate is dominated by high energy swell waves from south. However, significant seasonal variations in the wave conditions are experienced. The inter-annual variability of the deep-water wave parameters for the study site over a long period of 22 years, indicates that yearly wave characteristics are almost the same during the years (Figure 7). Furthermore, it presents an integration of clear annual cyclic pattern of monsoon waves and non-cyclic trend of non-monsoon waves.

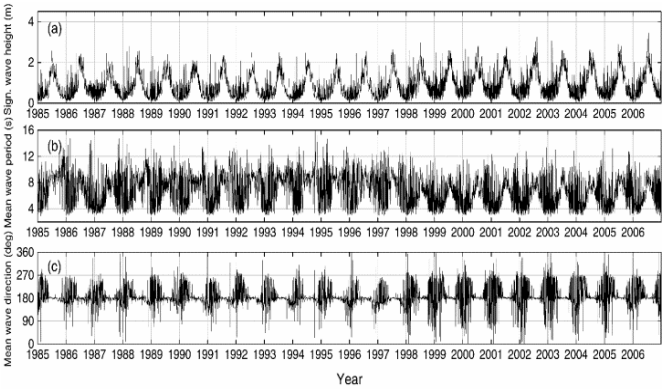


**Figure 7. Inter-annual variability in wave parameters between 1985 and 2006: (a) significant wave height, (b) mean wave period, (c) mean wave direction**

## 4.2. Longshore Sediment Transport Rate

Table 3 presents long-term mean annual net potential LST rates predicted by the selected methods for the study region. Comparative analysis of the long-term LST estimates obtained by different formulae indicates that the CERC equation overestimates the rate by about 136 and 39 percent than that of Kamphuis and Komar equation and the rate computed by the Komar formula is approximately 69 percent higher than Kamphuis equation. Mean annual net potential LST rates estimated with the CERC, Kamphuis and Komar expressions gave a value of 3.66, 1.55 and $2.63\times10^5$ $m^3year^{-1}$ to the west, respectively.

Although the estimated magnitudes vary widely, all three formulae agree on the monthly and annual net LST direction. The variations of the net LST rate over a period of 22 consecutive years suggest that the annual net transport rates are quite variable from year to year (Figure 8). A roughly irregular pattern with a maximum value in 1996 and a minimum one in 2000 are observed during the examined period. The net LST direction was predominantly found towards the west. Reversals in the net transport directions occurred twice during the study period. The main reason for this phenomenon may be related to the very strong eastward transport as observed in 2000.

**Table 3. Estimated long-term mean net potential LST rates**

| | CERC | Kamphuis | Komar |
|---|---|---|---|
| Potential LST ($10^5 m^3 year^{-1}$) | 3.66 | 1.55 | 2.63 |

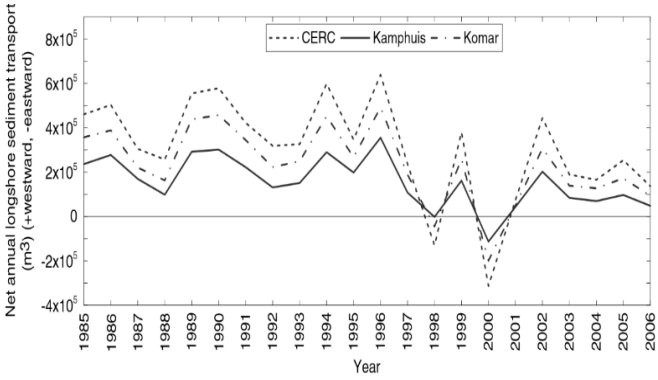


**Figure 8. Annual estimations and inter-annual variability of the LST computed for the 22 years of wave hindcast based on the CERC (1984), the Kamphuis (1991) and the Komar (1998)**

In order to provide the demonstration for the seasonal variability of LST, the net longshore transport was also examined based on monthly averages of 22-year (Figure 9). Seasonal variations in the LST rate are attributed to seasonal variations of the wave climate. Detailed analysis of the long-term monthly averages shows that the direction of net LST is from east to west throughout the year except during the monsoon months of June-July. As illustrated in Figure 6, the dominant direction of the wave is from SSE to S during the year, causing a large amount of sediment transport in westerly direction. It was also found that the wave height describes low energy conditions during the non-monsoon season, while during the monsoon season the wave energy increases and the waves are consistently high, which has a direct effect on the transport rate.

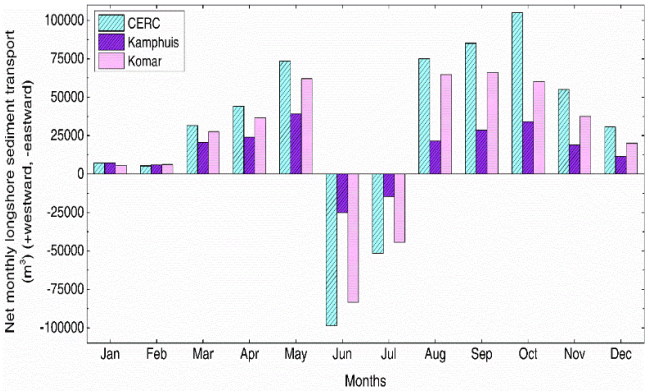


**Figure 9. Monthly average net LST rate estimated at the breaker zone for the 22 years of wave hindcast from the CERC (1984), the Kamphuis (1991) and the Komar (1998)**

$H_s$ within the monsoon period was 3 times the value during non-monsoon period. The computed LST rate based on the CERC, Komar and Kamphuis during monsoon period (4 months) was 54, 50 and 36 %, respectively, of the total LST rate. The non-monsoon season (8 months) contributes to about 46, 50 and 64 % based on the same formulae.

The performance of the LST rates calculated from the CERC formula noticeably depend on the values considered for the *K* empirical coefficient.Various values of the *K* coefficient have been presented by the researchers over the last decades (e.g., Bailard, 1981, 1984; Kamphuis and Readshaw, 1978; del Valle, Medina, and Losada, 1993). However, the default value for this parameter recommended by Komar and Inman (1970) employed in this study yielded unsatisfactory results. Then, the Komar formula produced the estimation close to that calculated by the CERC formula since both the formulae have the same input parameters that need to be calibrated and adjusted with the field data. The Kamphuis expression gives values significantly smaller than the values obtained by the CERC and Komar.

## 5. Discussion

The magnitudes of potential LST calculated using the hindcast wave data and empirical formulae may overestimate or underestimate the transport rates under different conditions and at different sites. In addition, the above LST relationships suffer from uncertainties arising from local conditions in which they were developed and are also based on the assumption of infinite supply of sand along the shoreline. In order to achieve logical long-term net longshore transport rates, a number of verifications are usually required for the geomorphology of the study area. Coastal landforms respond to all the variables of shore drift during their course of formation and hence these landforms can be considered the most reliable of long-term sediment transport indicators (Kunte and Wagle, 1993). The coastline between the Chabahar Bay and Ramin Harbor is dominated by rocky coral beaches to the west, near the Chabahar Bay. Further east, until Ramin Harbor, it consists of sandy beaches, which are limited landward by cliffs. The coast between Ramin Harbor and Beris Headland is partially rocky, along with straight sandy beaches backed by coastal dune systems. Sand bar formed at the mouth of Lipar seasonal river on the updrift (east) side of the Ramin Harbor blocks sediment load discharge to the sea (Figure 10). Hence, the Ramin Harbor is situated in a supply limited coast.


**Figure 10. Geomorphic landforms along the coastline extent between Chabahar Bay and Beris Headland**

The sediment transport regime can also be inferred from the established shoreline movement trend across the study area. A relative stability in shoreline position can be found both on up-drift and down-drift sides of the harbor, while an accretion trend may be detected at the beach leaned to the secondary breakwater (Figure 11). Dredging operations performed in 2004 are responsible for the considerable shoreline retreat within the outer basin of the harbor.

Numerical simulations conducted by Isaie Moghaddam et al. (2018), indicate that coastal currents over the study area flow toward the outer port basin and form

cyclonic gyres that contribute in transporting and depositing coastal sediments within the port basins and around the secondary breakwater. These corroborates that the net LST direction is westbound (into the harbor basins). In other words, the outer harbor basin acts as the substantial sediment sink which entrapped the majority of littoral sand coming from east coast of Ramin. Therefore, the real (or actual) net LST rate can be equated to the amount of sediments accumulated in harbor basins.

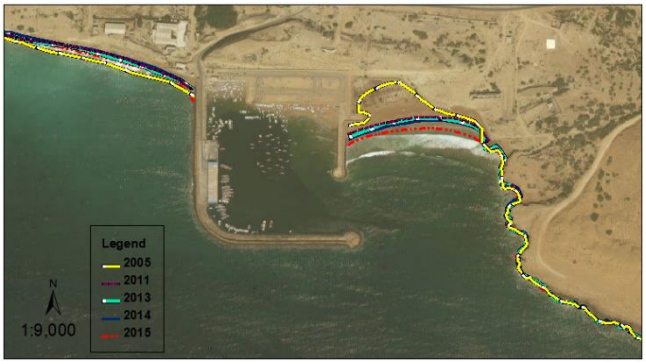


**Figure 11. Historical shoreline position at the study area over a 10-year period (instantaneous wet/dry line proxy)**

Also, in order to determine actual net LST rate across the study area, volumetric differences based on hydrographic surveys and dredging records may be used. Two bathymetric surveys carried out in 2000 and 2009 at the nearshore zone of the Ramin Harbor. However, the survey interval is not short enough to identify different seasonal changes. Concern to dredging activities, the regions adjacent to the harbor mouth and the secondary breakwater, where the majority of sediments are deposited were frequently dredged. The amounts of materials removed in 2002 and 2004 were about $0.625\times10^5$ $m^3$ and $0.658\times10^5 m^3$, respectively. These dredging figures yield the associated actual net LST rate about $0.3\times10^5$ $m^3 year^{-1}$ at Ramin Harbor.

Evaluation of coastal landforms, geomorphological indicators and dredging records of the coastal stretch under consideration suggest that the availability of sand at the littoral section has been restricted. Then, it may be concluded that actual longshore transport rate will be significantly less than that of the calculated potential rate. Moreover, the magnitudes of potential LST calculated based on CERC and Komar formulae overestimated the transport rates and can lead to large coastline variations which were not observed along the study area. However, the rates estimated based on the Kamphuis expression are considered more suitable for the evaluation area. This confirms the results of Afshar-Kaveh and Soltanpour (2010), who suggested the Kamphuis (1991) equation as offering reliable formula along the Iranian southern coasts. Moreover, Schoonees and Theron (1996) and Schoonees (2001), evaluated the efficiency of 52 different LST formulae against an extensive database collected at a wide variety of sites around the globe and found that the Kamphuis (1991) formula is the most accurate overall (Schoonees, Theron, and Bevis, 2006).

## 6. Conclusions

Estimates of the annual and inter annual LST variations along the Ramin Harbor, southeast coastline of Iran, have been determined using 22 years hindcasted wave data. Annual cycle of wave climate over the study area was dominated by two distinct seasonal changes: high energy waves from southern sector with an average period of 8.05 sec and height range from 0.78 to 2.15 m during monsoon season, and long period swells spreading from southeast to south direction superimposed with variable wind waves from west to southwest with the average period of 6.25 sec and wave height of 0.48 m during non-monsoon period. Computed long-term mean net potential LST rate for the region is 3.66, 1.55 and $2.63\times10^5 m^3 year^{-1}$ based on the CERC, Kamphuis and Komar formulae, respectively. The seasonal variation in LST rate was also observed in response to the seasonality of wave regime. Multiple lines of evidences have been deployed to evaluate the predicted LST magnitudes and directions. For this case study, the investigation was made at sandy beaches bounded with short stretches of rocky outcrops, where geologic features normally control sediment transport. Consequently, the actual longshore transport rate was less than the potential transport rate. It has then been found that the Kamphuis formula yielded more acceptable values in comparison with the other two formulae. In addition, a net sediment transport to the west was inferred from calculations and environmental observations.

## Acknowledgments

Authors acknowledge Iranian Ports and Maritime Organization (PMO) and Iranian National Institute for Oceanography and Atmospheric Science (INIOAS) for making the wind and wave data available. The first author also wishes to express his sincere thanks to Kh. Bahiraie for his keen interest and encouragement, and also to Dr. A. Nasrollahi for his valuable explanations of MIKE software applications and suggestions which greatly improved quality of this research study. This work would not have been possible without availability of the MIKE 21 product provided by Danish Hydraulic Institute (DHI) and their contribution is greatly appreciated.

## References

1- Afshar-Kaveh, N. and Soltanpour, M., (2010), *Verification of longshore sediment transport formulas at some of the southern coastlines of Iran*, Journal of

Civil and surveying Engineering, Vol.44(3), p.317-326.

2- Bailard, J. A., (1981), *An energetics total load sediment transport model for a plane sloping beach*, Journal of Geophysical Research, Vol. 86.

3- Bailard, J. A., (1984), *A simplified model for longshore sediment transport*, Proceedings of the 19th International Conference on Coastal Engineering, p.1454-1470, Houston, Texas.

4- Battjes, J. A. and Janssen, J. P. F. M., (1978), *Energy loss and set-up due to breaking of random waves*, Proceedings of the 16th International Conference on Coastal Engineering, p. 569-587, Hamburg, Germany.

5- Camenen, B. and Larroudé, P., (2003), *Comparison of sediment transport formulae for the coastal environment*, Coastal Engineering, Vol.48(2), p.111-132.

6- CERC, (1984), *Shore protection manual*. Washington: Coastal Engineering Research Center, U.S. Army Corps of Engineers Press.

7- Chempalayil, S. P., Kumar, V. S. and Dora, G. U. and Johnson, G., (2014), *Near shore waves, long-shore currents and sediment transport along micro-tidal beaches, central west coast of India*, International Journal of Sediment Research, Vol.29(3), p.402-413.

8- del Valle, R., Medina, R. and Losada, M. A., (1993*), Dependence of coefficient K on grain size*, Journal of Waterway, Port, Coastal and Ocean Engineering, Vol.119(5), p.568-574.

9- *DHI MIKE 21 Wave modeling user guide*, (2014), Denmark: DHI Water and Environment.

10- Dibajnia, M., Kebriaee, A., and Allahyar, M., (2008), *Wave climate hindcast for the Oman Sea*, Proceedings of the 8th International Conference on Coasts, Ports and Marine Structures p.29-31, Tehran, Iran.

11- Güner, H. A. A., Yüksel, Y. and Çevik, E. Ö., (2013), *Longshore sediment transport-field data and estimations using neural networks, numerical model, and empirical models*, Journal of Coastal Research, Vol.29(2), p.311-324.

12- Isaie Moghaddam, E., Hakimzadeh, H., Allahdadi, M.N., Hamedi, A., Nasrollahi, A., (2018), *Wave-induced currents in the northern Gulf of Oman: a numerical study for Ramin Port along the Iranian coast*, American Journal of Fluid Dynamics, Vol.8(1), p.30–39.

13- Kamphuis, J. W., (1991), *Alongshore sediment transport rate*, Journal of Waterway, Port,

14- Coastal and Ocean Engineering, Vol.117(6), p.624-640.

15- Kamphuis, J. W. and Readshaw, J. S., (1978), *A model study of alongshore sediment transport rate*, Proceedings of the 16th International Conference on Coastal Engineering, p.1656-1674, Hamburg, Germany.

16- King, D. B. Jr., (2005), *Influence of grain size on sediment transport rates with emphasis on the total longshore rate (Technical report of ERDC/CHL CHETN-II-48)*, Washington: U.S. of Army Corps of Engineers.

17- Komar, P. D., (1998), *Beach processes and sedimentation*, p.544-545, New Jersey: Prentice Hall Inc. Press.

18- Komar, P. D. and Inman, D. L., (1970), *Longshore sand transport on beaches*, Journal of Geophysical Research, Vol.75(30), p.5914-5927.

19- Kunte, P. D. and Wagle, B. G., (1993), *Remote sensing approach to determine net shore drift direction-a case study along the central east coast of India*, Journal of Coastal Research, Vol. 9(3), p.663-672.

20- Larangeiro, S. H. C. D. and Oliveira, F. S. B. F., (2003*), Assessment of the longshore sediment transport at Buarcos beach (west coast of Portugal) through different formulations*, In Proceedings of CoastGIS'03, Genova, Italy.

21- Mafi, S., Yeganeh-Bakhtiary, A. and Kazeminezhad, M. H., (2013), *Prediction formula for longshore sediment transport rate with M5' algorithm*, Journal of Coastal Research, Vol.2(SI 65), p.2149-2154.

22- Prasad, K. and Reddy, B., (1988), *Near-shore sediment dynamics around Madras Port, India*, Journal of Waterway, Port, Coastal and Ocean Engineering, Vol.114(2), p.206-219.

23- Schoonees, J. S., (2000), *Annual variation in the net longshore sediment transport rate*, Coastal Engineering, Vol.40(2), p.141-160.

24- Schoonees, J. S., (2001), *Longshore sediment transport: applied wave power approach, field data analysis and evaluation of the formulae*, PhD thesis, University of Stellenbosch, Stellenbosch.

25- Schoonees, J. S. and Theron, A. K., (1996), *Improvement of the most accurate longshore transport formula*, Proceedings of the 25th International Conference on Coastal Engineering, Vol.3, p.3652-3665, Orlando, Florida.

26- Schoonees, J. S., Theron, A. K. and Bevis, D., (2006), *Shoreline accretion and sand transport at groynes inside the Port of Richards Bay*, Coastal Engineering, Vol.53(12), p.1045-1058.

27- Shanas, P. R. and Sanil Kumar, V., (2014), *Coastal processes and longshore sediment transport along Kundapura coast, central west coast of India*, Geomorphology, Vol.214, p.436-451.

28- Sheela Nair, L., Sundar, V. and Kurian, N. P., (2015), *Longshore sediment transport along the coast of Kerala in southwest India*, Proceedings of the 8th International Conference on Asian and Pacific Coasts, Vol.116, p.40-46, Chennai, India.

29- Short, A. D., (1991), *Macro-meso tidal beach morphodynamics-an overview*, Journal of Coastal Research, Vol.7(2), p.417-436.

30- Short, A. D. and Hesp, P. A., (1982), *Wave, beach and dune interactions in southeastern Australia*, Marine Geology, Vol.48(3-4), p.259-284.

31- Smith, E. R., Wang, P., Ebersole, B. A. and Zhang, J., (2009), *Dependence of total longshore sediment transport rates on incident wave parameters and breaker type*, Journal of Coastal Research, Vol.25(3), p.675-683.

32- Tolman, H. L., (2009), *User manual and system documentation of WAVEWATCH III version 3.14 (Technical Note 276)*, National Oceanic and Atmospheric Administration (NOAA), Camp Springs, MD 20746.

33- Walters, K. R. and Sjoberg, W. F., (1988), *The Persian Gulf region, a climatological study*, Washington: U.S. Marine Corps, Department of the Navy Press.